EVALUATION OF ATLAS-BASED BRAIN SHIFT MODEL FOR IMPROVED ADAPTATION TO INTRAOPERATIVE NEUROSURGICAL CONDITIONS

By

Ishita Chen

Dissertation

Submitted to the Faculty of the

Graduate School of Vanderbilt University

in partial fulfillment for the requirements for

the degree of

DOCTOR OF PHILOSOPHY

in

Biomedical Engineering

May 2012

Nashville, Tennessee

Approved:

Michael I. Miga

Benoit M. Dawant

Robert L. Galloway

Reid C. Thompson

Robert J. Webster III

ACKNOWLEDGEMENTS

Little did I know that chance encounters with three people eight years ago would impact my life so profoundly. I met Dr. Michael Miga in 2005 when I was presenting my undergraduate research work at the SPIE Medical Imaging conference. Though at the time I had no knowledge of the field of image guided surgery, I was struck by two things— "brain shift" was an odd sounding phrase and Dr. Miga spoke very enthusiastically about it. The intrigue of the problem and encouragement by Dr. Miga led me to pursue this work. I owe an enormous debt of gratitude to him for providing me with the opportunity to work in his lab and on this project, for his guidance and support as my advisor throughout the years, and for his unwavering patience as I learned through making, perhaps much more than, my fair share of mistakes.

At this same conference I also met Dr. Robert Galloway, who over the next years, advised me in my master's thesis project, served on my PhD committee and was very generous with his help for this project. He kept his door open to hear out my problems — technical as well as non-technical — and for that I am very grateful. I would also like to thank Dr. Benoit Dawant, Dr. Robert Webster, and Dr. Reid Thompson, who served on my PhD committee. Dr. Dawant provided amazing ideas and expertise with the image processing aspects of this work. Dr. Webster provided insightful comments and critiques to help develop this work. Dr. Thompson helped us collect intraoperative data, without which this project would not have been possible. His feedback was invaluable for the consideration of clinical feasibility for the development of the methodology. In addition to his help with this project, Dr. Thompson provided me with tremendous amount of help

and encouragement as I looked to the next phase of my career. He nurtured my interest in clinical medicine and welcomed me into his clinic to learn the stories of patients to whom this work is truly dedicated. These were some of the bravest people I have met and I hope to serve their needs through wherever life takes me next.

The members of BML, SNARL, and MIP labs were not only instrumental to the completion of this project but also kept me sane through all the years in graduate school. I will run out of room and synonyms for gratitude before I am able to list the tremendous contributions they each made towards my education and the many ways in which they touched my life. I would like to acknowledge two individuals in particular because of the sheer number of hours they logged helping me with this project and in my personal growth. Prashanth Dumpuri showed me the ropes when I was starting out and helped me fill the many gaps in my knowledge. I owe a special thanks to Rowena Ong for her enormous help with this project and for her love and friendship. I would also like to thank the operating room staff, residents, and nurses in the Department of Neurosurgery and the CT technicians in the Department of Radiology for their help with data collection. I am also grateful to the National Institutes of Health (NIH)—National Institute of Neurological Disorders and Stroke that supported this work under Grant R01 NS049251-01A4.

The closing brings me to the last of those three life changing chance encounters. Eight years ago when interviewing at Vanderbilt University for graduate school, I met a student in the MD/PhD program in SNARL lab excitedly talking about the confluence of medicine, engineering and science. I had no idea that eight years later I would be married to this man. I am incredibly grateful to my husband Richard Chen for loving me despite

all my faults and flaws. Lastly, and most importantly, I would like to thank my parents and sister for their lifelong love and support. None of this would have been possible without them.

TABLE OF CONTENTS

Page

LIST OF TABLES

LIST OF FIGURES

Figure Page

CHAPTER I

PURPOSE AND SPECIFIC AIMS

There are an estimated 13,000 deaths and 18,000 new cases every year for all primary malignant brain and central nervous system (CNS) tumors. This translates to an age-adjusted incidence rate of about 9 per 100,000 people. Gliomas, primary tumors of the supporting tissue of the nervous system, account for 77% of all primary malignant brain tumors [1]. The general prescribed treatment for a primary brain malignancy is some combination of neurosurgery, chemotherapy and radiation therapy. Image guidance, that utilizes a rigid registration between the preoperative magnetic resonance (MR) images and physical space of the operating room, is now the standard of care in neurosurgical procedures. The fidelity of the image guidance system is known to be compromised by the extensively studied phenomenon of brain shift. A considerable body of work in literature has focused on solving this problem either through intraoperative imaging or by updating preoperative images with mathematical models. The factors that affect the magnitude and the direction of tissue deformation cannot be predicted to exact precision before the procedure and are often difficult to measure during the procedure. To account for this uncertainty, a statistical atlas-based method was described in [2] and was used to capture the range of possible solutions. This was work was validated using postoperative MR data in [3]. The postoperative MR data encapsulates the general trends of deformation of brain tissue under conditions of surgical load. Postoperative MR images are typically acquired after a lapse of 24 hours of surgery, during which period a

shift recovery is known to occur. As a result, the postoperative measurements are typically smaller than what would be observed intraoperatively. Moreover the surgical environment is quite dynamic due to active tissue resection and retraction, which affect the observed displacements in the region of the craniotomy. The goal of this work was to systematically study the differences between the pre-post MR deformation and preoperative MR and intraoperative laser range scan (LRS) deformation and devise strategies to better adapt the atlas-based model for intraoperative conditions. These goals were accomplished through the following specific aims.

Specific Aim #1: *Improve the subsurface accuracy by incorporating dural septa into the atlas-based model.*

a. Develop a strategy to segment the falx cerebri and tentorium cerebelli from MR images and incorporate these membrane structures into the brain shift model.
b. Study the effect on surface and subsurface displacements of incorporating these membranes into the atlas-based model.
c. Systematically study the difference between the pre-post MR deformation and pre MR- intraoperative LRS deformation.

Specific Aim #2: *Study strategies to enhance the feasibility of intraoperative implementation of the atlas-based method.*

a. Decrease the computational time through automated segmentation of brain tissue and the dural septa and compare the shift correction results to manually segmented results.
b. Perform a sensitivity analysis to determine an optimal atlas size and resolution while maintaining the fidelity of shift correction results.

Specific Aim #3: *Simulate the effects of using a retractor during surgery and devise a technique for including that information in the model based image update.*

a. Develop an algorithm to update the atlas-based model with local displacements occurring due to the use of a retractor device during surgery.
b. Perform a validation of the above method using simulation and phantom experiments.

Specific Aim #4: *Develop a computational tumor growth model to serve as preliminary basis for estimation of decompressive stresses associated with tumor resection*

a. Modify the reaction-diffusion equation of tumor growth to account for the inhibitory effect of mechanical stress due to the mass effect.
b. Perform simulation experiments to compute tumor cell concentration and resultant stresses and strains for a simplistic one dimensional implementation.

CHAPTER II

BACKGROUND

Image guidance found its earliest applications in neurosurgery and today it is the standard of care for the surgical treatments of central nervous system neoplasia, epilepsy and cerebrovascular disorders. The fidelity of image to physical space registration, that drives the neurosurgical image guidance system, is known to be compromised by the phenomenon of brain shift, a non-rigid deformation of brain tissue caused by gravity, edema, hyperosmotic drugs administered prior to surgery and tissue resection. This problem was identified by Kelly et. al. when they observed displacement in metal beads implanted in the brain cortex during image guided laser resection of tumors [4, 5]. Hill et. al. studied brain tissue deformation between the preoperative MR images and intraoperative images after dura opening but before tumor resection and found displacements greater than 1 mm [6]. Other systematic studies to characterize this deformation were performed with the aid of intraoperative imaging modalities and different studies found that the range of deformation for brain tissue could vary from 1cm to 2.5 cm from their pre-operative state during surgery [5, 7, 8]. A trained neurosurgeon is aware of the misalignment between the surgical field and the preoperative image and compensates for it to some extent [9] but it is not always possible to accurately predict the amount of shift.

Correction of brain shift using intraoperative volumetric imaging

Extensive work has been reported in literature to compensate for brain shift using various intraoperative imaging techniques— CT, MRI and ultrasound. Lunsford et. al. discussed the construction and usage of an operating suite outfitted with an intraoperative CT scanner [10]. Images were acquired before, during and after tumor resection to guide and evaluate the extent of the resection. Okudera et. al. redesigned the intraoperative CT equipment such that the gantry was mobile and the scanner contained a head fixation device [11]. This removed the limitation of having to perform the surgery with the head placed in the gantry. Each of the two works reported above required a special operating room (OR) suite that housed a dedicated CT unit. Installation of multiple units in a big hospital could be quite expensive. Butler et. al. overcame that limitation by designing a mobile CT unit that could be wheeled to the OR as needed [12]. Despite these advancements, the widespread use of intraoperative CT has been hampered by concerns for radiation exposure.

MRI offers superior soft tissue contrast without the risk of ionizing radiation inherent in CT imaging. Acquiring real-time updated MR images during tumor resection and other neurosurgical procedures, and using those for guidance has been explored by several groups [13-21]. Black et. al. described the construction of a vertical magnet with a double doughnut configuration [13]. This provided a vertical spacing for access to the site being actively imaged during stereotactically guided biopsy or craniotomy. This method had the limitation of confined access to the surgical site. Surgery during active imaging in the magnet bore also required use of special non-ferrous instruments. A different system described in [17] resolved some of these issues by designing a weak

magnet (0.2-tesla) placed in an RF shielded area, which is separate from the operating area. The operating table had a head fixation system and could be moved between the two areas to operate and image as needed. In this case, only some of the instruments like retractors and biopsy cannulas needed to be MR compatible, rest of the instruments could be used as usual. This system had its own limitations including the weak field strength and additional time spent in patient transit. By contrast, Sutherland et. al. presented a system where instead of the patient being moved from surgical area to imaging area, the magnet is moved from a storage area to the operating area [18]. Hadani et. al. described a compact magnet mounted on transportable gantry that could be stowed away under the surgical table when not in use [22]. This system, though more compact than the design of Sutherland et. al., as a tradeoff had weaker signal strength and a more limited field of view. Installation of a dedicated intraoperative MR unit can be prohibitively expensive, especially when adding in the costs of adapting an OR suite to storing and operating the imaging equipment and use of non-ferrous surgical instruments.

Like MR, ultrasound does not have the risk of ionizing radiation but unlike MR, it is a lot more cost efficient and less bulky for placement in the OR. Trobaugh et. al. described a method to construct and register 3D ultrasound images to tomographic images with a stress towards neurosurgery applications [23]. Comeau et. al. used an overlay of 2D ultrasound images on preoperative MR images to give context to the structures within the ultrasound images and display the deformation that had taken place intraoperatively [24]. Downey et. al. explored the use of 3D ultrasound for guiding needles in biopsy [25]. Gobbi et. al. optically tracked the ultrasound probe, created visualization of the brain shift and used homologous landmarks to generate a thin plate

spline transform to correct the shift in phantom data [26, 27]. Letteboer et. al. used the tracked ultrasound system to measure brain shift intraoperatively before and after dura removal in 12 patients [28]. Despite the low cost, the use of ultrasound for delineating tumor margins is limited by the low signal to noise ratio.

Due to the various limitations associated with each modality, there have been difficulties adapting them as means to provide updated information in the OR after shift has occurred. Recently, more developments have been made with using the intraoperative images as a means to warp the preoperative MR images as opposed to using them directly for guidance.

Use of intraoperative volumetric imaging to update preoperative images

Advances in MRI field have permitted the acquisition of rich information preoperatively such as functional imaging, diffusion weighted imaging or angiography. Surgical constraints do not permit reacquisition of that data intraoperatively [29]. The brain shift literature has shown a general move towards pursuing research to update the preoperative images rather than using the intraoperative images directly for guidance. Hata et. al. used non-rigid registration between preoperative and intraoperative MR images using a mutual information metric [30]. 3D volumetric non-rigid registration does not have a closed form solution and can be quite computationally intensive, making it unsuitable for use within the surgical timeframe. Biomechanical models using discretized methods such as finite element techniques have been explored by many groups for this problem. Hagemann et. al. performed a 2D analysis using a linear elastic model driven by surface displacements computed using active contours method [31]. They performed

analysis on real clinical as well as synthetic data. For clinical data, images were acquired preoperatively and postoperatively. Tumor and resection area outlines were manually selected by an expert and then a snake algorithm was applied to determine the correspondence of the outlines. This correspondence was then used as a boundary condition to drive the linear elastic model, which was solved using the Galerkin approximation of the finite element method. Ferrant et. al. followed a similar approach in 3D preoperative and intraoperative (0.5 T magnet) images [32]. They extracted the surface of the cortex and the lateral ventricles from the preoperative and intraoperative MR images. The boundary surfaces were used with an iterative shape matching algorithm to compute the surface displacements. These surface displacements were used as boundary conditions in a linear elastic model to obtain the volumetric displacements over the entire mesh, which were then interpolated back to the image grid to deform the original preoperative image. Wittek et. al. used the non-linear model for large displacements to solve the problem [33]. As in the work of Ferrant et. al. the brain parenchymal surface, tumor and ventricles were segmented and used to generate a patient specific mesh. The displacements on the surface were computed from the use of intraoperative imaging and used for computing the displacements over the entire domain. Clatz et. al. used a block matching algorithm instead of surface information to drive a linear elastic model [34]. Blocks were selected based on their intensity variance and they provided subsurface displacement information as well. A hybrid interpolation and approximation technique was used to compute the dense displacement field. All of the above listed methods require an intraoperative MR scan and as previously discussed,

those devices are not widely available in the operating rooms due to high cost of operation.

Use of sparse intraoperative data to update preoperative images

A more cost effective alternative to volumetric intraoperative images is to use sparse data, which wouldn't necessitate the installation of expensive tomographic devices in the OR. Stereoscopic cameras and laser range scanners are two devices in this category. They have been used by different groups to capture cortical surface data to measure intraoperative brain shift. The former involves a pair of charge-couple device (CCD) cameras attached to the binocular optics of stereoscopic microscope. A set of corresponding points are located between the left and right images and triangulation is used from that correspondence to estimate a 3D surface. Skrinjar et. al. and Sun et. al. used this technique to compute intraoperative brain shift [35, 36]. The laser range scanner (LRS) works on the optical principle of triangulation as well. The surface of interest is illuminated with a laser light source and the reflected light is detected by the CCD camera, which is located in the scanner. The depth is computed based on the detected light pattern and the known geometrical relation between the camera and the laser source. Audette et. al. used a laser range scanning device with a non-rigid 2D spline based iterative closest point (ICP) algorithm to register the LRS data to the MR cortical data [37]. Sinha et. al. used a surface mutual information technique to register the LRS data to the MR textured surface [38]. Cao et. al. performed a systematic comparative study of different registration techniques to register physical space and preoperative MR image space [39]. The authors compared feature point based registration, vessel contour ICP

based registration, and the Surface MI method developed in Sinha et. al. [38]. They also extended the latter method with an additional constraint of high correspondence confidence, and found that overall it provided the most robust registration results. Registration between serial LRS images (before and after tumor resection) was studied by Sinha et. al. using a non-rigid surface registration technique [40]. This work was extended by Ding et. al., who obtained an improvement in mean target registration error using a semi-automatic vessel contour registration method [41]. Some of these works address subsurface shift by using the sparse surface measurements to drive finite element models while some provide updated information through overlays on the surface of the MR [36]. Although the largest amount of shift error occurs on the surface, having accurate updated subsurface information would be important in surgical decisions to delineate the remainder of tumor margin after resection.

Prediction of brain shift using biomechanical models

The same reasons that make biomechanical models the methodology of choice with intraoperative MR, make it a viable avenue to pursue with sparse intraoperative data to obtain subsurface shift information. Skrinjar et. al. compared a damped spring mass model and a linear elastic model for use in conjunction with their stereoscopic camera data, and found that the continuum model was preferable because the spring damping model was mesh dependent on model parameters and lacked a good model guidance strategy [35]. Warfield et. al. treated the brain tissue as a homogenous linear elastic material and drove the model with deformations computed at the surface of the cerebrum and lateral ventricles [42]. Bucki et. al. similarly demonstrate the use a displacement

driven linear elastic model to correct for shift error [43]. Hu et. al. used a linear viscoelastic model to describe the gravity induced brain shift [44]. Joldes et. al. used an incompressible non-linear neo-Hookean model [45]. Miller et. al. and Wittek et. al. applied the hyperelastic models to address the problem of brain shift [33, 46-48]. Although the non-linear models may better reflect the brain tissue mechanics with loads similar to that experienced during surgery [49, 50], due to their complexity and computational cost, their feasibility of use for model guided surgical system update has not been adequately demonstrated. Paulsen et. al. used a biphasic model to describe the brain shift in the OR [51, 52]. This model was originally developed by Biot to explain soil mechanics by treating it as a porous medium [53]. In a manner similar to the soil consolidation, it treats the brain tissue as consisting of two distinct phases. The elastic deformations of the solid phase and the pressure gradients of the fluid phase are coupled together. Miga et. al. demonstrated the applicability of this work to gravity induced brain shift in the OR [54]. This model was purely predictive and the sparse data was used for validating the model results. The actual model was driven by simulated forces in the OR such as gravity, pressure gradients caused by hyperosmolar medication, edema etc. These forces are very challenging to measure intraoperatively and cannot be predicted with precision before the surgery.

Use of inverse modeling technique to predict intraoperative brain shift

In order to account for the uncertainty in intraoperative conditions, atlas-based methods have recently been developed [2]. In their work, Dumpuri et. al. built an atlas of solutions that accounted for shift caused by gravity, edema, and mannitol with different

head orientations, fluid levels, and capillary permeabilities. The inverse solution was then reconstructed by minimizing the least squared error between the solutions and the measurements made with sparse data. This method was validated with postoperative MR data and the predictions were found to work well with the surface and subsurface measurements. It was noted that the deformations measured intraoperatively are often larger than the postoperative displacements because an estimated 25% shift recovery happens in the period between the surgery and time the postoperative scans are performed. There is also more variation in the displacements because intraoperatively the brain tissue is subjected to forces like resection and retraction. In [2] and [3] the atlas-based inverse model was developed and the surface and sub-surface accuracy was evaluated. In the following sections, strategies to improve the feasibility of intraoperative implementation for the atlas-based model will be presented.

CHAPTER III

METHODOLOGY

Subsequent to this chapter, a series of studies are performed to test the new innovative work that has resulted from this thesis. Each of these studies share aspects of a common framework which has been enhanced through this dissertation. To provide the reader with a complete context of the methodology to include the innovations presented in this work, this chapter of the thesis introduces the overall framework and these new developments. The overarching framework steps involved are: image processing, geometric model development, biomechanical model realization, parameterization of boundary conditions, construction of an inverse approach, and compensation within the image-guided surgery platform. This thesis contributes novel material in the areas of geometric model development, analysis of method sensitivity, and biomechanical model realization. In these next sections, we will step-by-step move through the framework indicating where the new contributions will be made.

Image segmentation

With respect to the brain shift compensation framework, the approach begins by segmentation of the object of interest, i.e. the brain. The pre-operatively acquired images for intraoperative guidance are high resolution T1 weighted MR images. In order to construct a geometric model (the next step in the framework), the structures of interest in the images must be segmented. The need for anatomic accuracy must be balanced with computational efficiency, and for this reason, the structures selected for segmentation are

the brain, tumor, and the dural septa. The segmentation can either be done manually, semi-automatically, or automatically. Briefly, the semi-automatic and automatic segmentation method for dural septa is described below.

Semi-automatic segmentation: Falx cerebri and the tentorium cerebelli are the two important sub-structures of the dural septa. In this realization, different segmentation techniques were used for each. The falx was segmented manually by drawing on the mid-sagittal slice of the brain. This is shown in Figure 1 below.

(a) 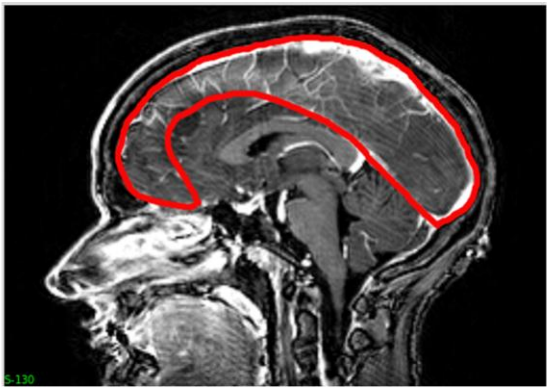 (b) 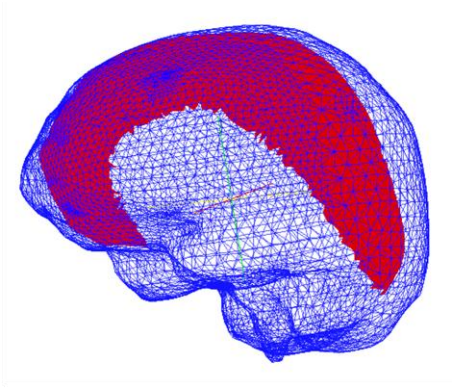

Figure 1. Falx segmentation procedure. (a) Manual periphery drawn around falx on gadolinium enhanced MRI (b) segmented falx overlaid with the mesh.

Figure 1 shows the contour of the falx drawn on the brain image slice and the segmented falx overlaid with the finite element mesh. The left and the right tentorium were segmented separately and this segmentation procedure is shown in Figure 2 below.

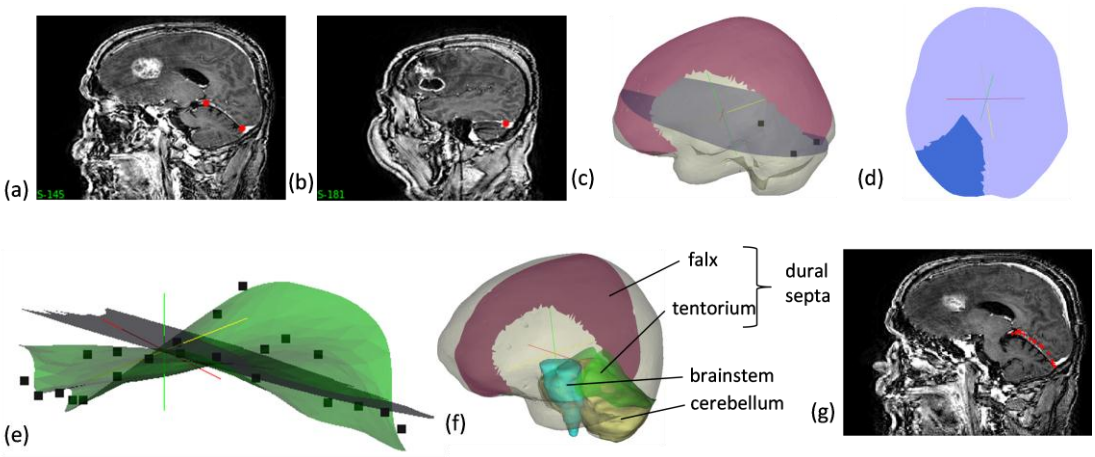

Figure 2. Procedure for tentorium segmentation. (a) and (b) show the selection of three points used for clipping a plane in the mesh, (c) shows the clipped plane (with those three points) overlaid with the mesh and the falx, (d) shows the clipped plane segmented into an approximate tentorium shaped structure and (e) shows the segmented plane with the final tentorium surface created by morphing the plane in (d) using a thin plate spline algorithm. The points on the surface are the target points used to drive the thin plate spline algorithm. (f) shows the mesh overlaid with the segmented falx and the tentorium surfaces. The segmented brainstem (in blue) and cerebellum (in yellow) are shown for reference, were not modeled separately. (g) is the sagittal MRI slices overlaid with the red points of the tentorium surface. A good overlap of the points and the hyperintense region indicate the quality of segmentation.

For each side, a plane that roughly passes through the tentorium region is created, which is then manually clipped into a tentorium shaped structure. This clipped plane is then morphed into the tentorium shape using the thin plate spline algorithm [55]. The resulting surfaces are shown in Figure 2 (e)–(g).

Automatic segmentation: The automated segmentation algorithm is based on the atlas-based segmentation approach described in [56]. The segmentation was performed using a series of three steps, during which the patient images acquired above are registered to a template T1 image of size 256 × 256 × 256 and 1 mm × 1 mm × 1 mm voxel size, for which an expertly segmented binary mask and dural septa with method described above was available. The steps of the segmentation are described in the schematic below.

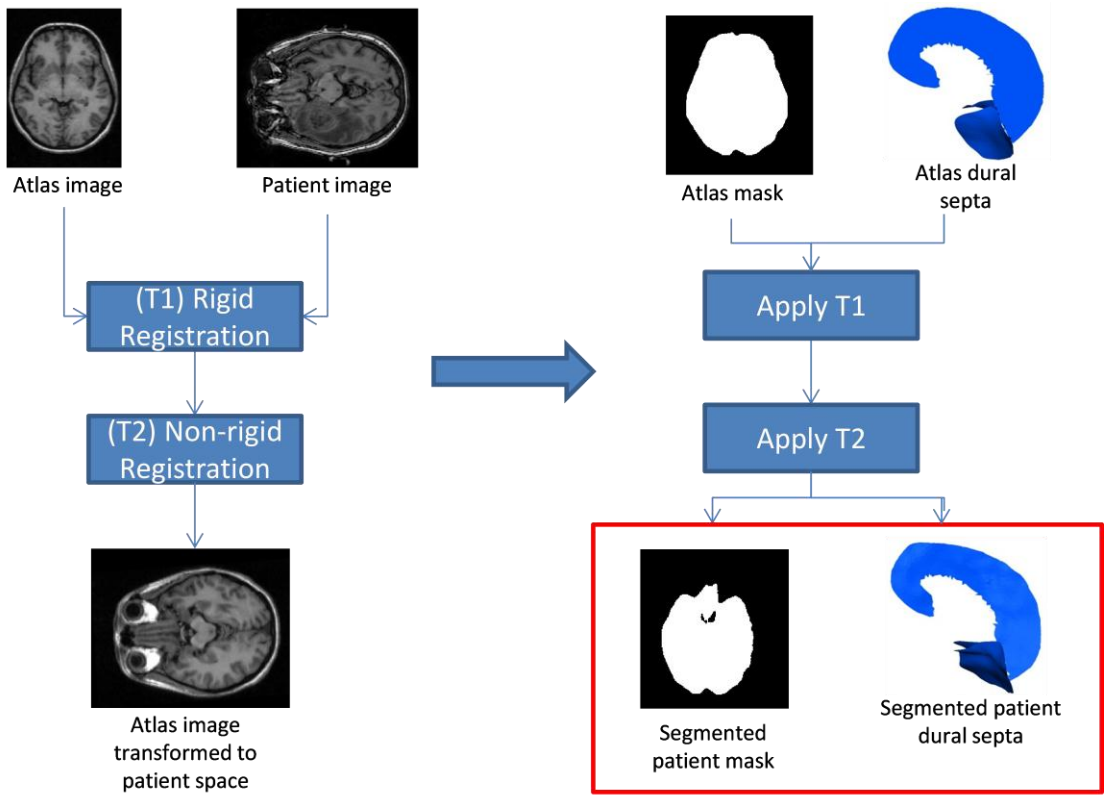

Figure 3: The schematic for segmentation of cerebral tissue and dural septa. A rigid transformation between an atlas image and patient image (T1) is computed. The transformation, T1 is applied to the atlas image and a non-rigid transformation (T2) is computed between the rigidly transformed atlas image and the patient image. The computed transformations (T1 and T2) are applied to structures derived from the atlas image (binary mask and dural septa templates) to obtain the segmentation of patient cerebral tissue and dural septa.

The patient image is registered to the template image using a series of two steps: a rigid registration and non-rigid registration, resulting in transforms T1 and T2 respectively. These transformations are then applied to the pre-segmented image binary mask and dural septa template surfaces to provide patient specific structures.

In Chapter IV, the manual segmentation of the brain and the semi-automatic segmentation of the dural septa will be described and are investigated within the context of intraoperative brain shift compensation. To our knowledge, this is the first comprehensive investigation focused at understanding the influence of the dural septa for biomechanical model-based techniques in compensation. In Chapter V, the automatic

segmentation algorithm will be described in greater detail. A comparison of these two different segmentation methods will also be presented in Chapter V. To our knowledge, this is the first study to evaluate the robustness and sensitivity of an automatic method to deploy dural septa.

Mesh generation

Once the organ has been segmented form the image volume, the task of generating a geometric description for use in numerical integration techniques for partial differential equations (e.g. finite element techniques) begins. Here, brain and tumor surfaces were created from the segmented binary masks using the marching cube algorithm [57] and smoothed using the Laplacian smoothing function [58]. A mesh generating program was used to create a mesh with tetrahedral elements from these surfaces [59]. This process is shown in Figure 4 below.

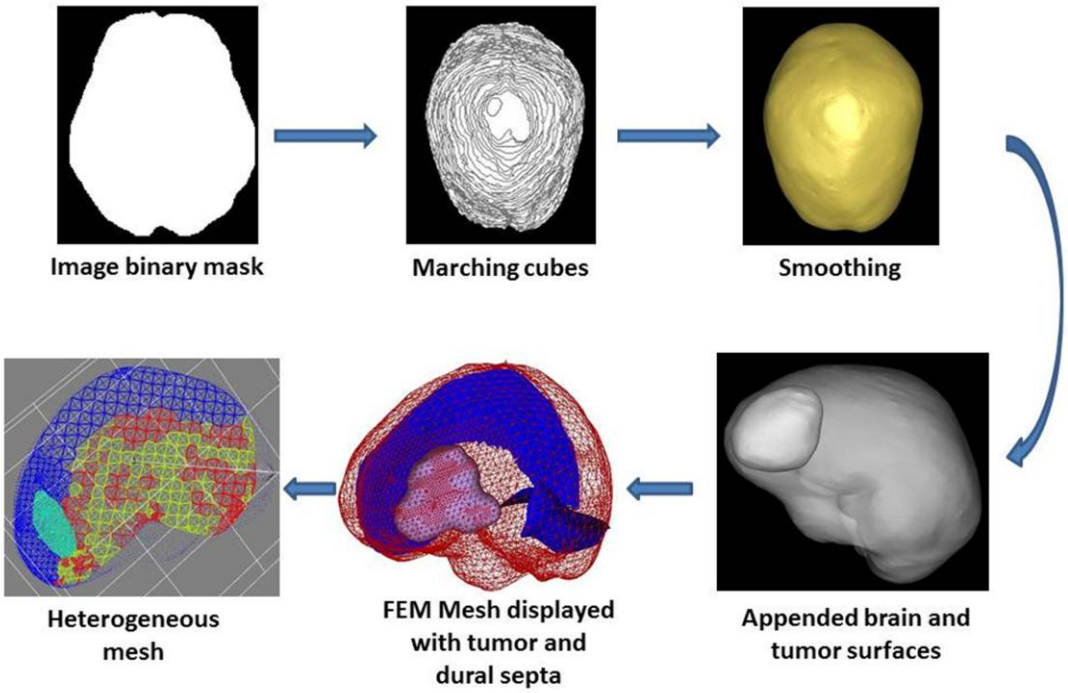

Figure 4: The binary image mask is used to generate the marching cubes surfaces, which are then smoothed using a Laplacian function. These surfaces are created for the brain and tumor, though the above figure only shows brain surfaces. The brain and the tumor surfaces are then appended and used to generate a finite element mesh with the previously segmented dural septa. An image intensity threshold is used to classify the elements into grey and white matter. The image in second row on far left is a slice of the heterogeneous mesh, with blue-falx, cyan-tumor, red-gray matter, green-white matter.

The edge length of the element was ~5 mm and refinement was performed around the tumor surface. Usually this resulted in ~20,000 nodes and ~100,000 elements. An intensity threshold was then used to classify the brain parenchyma elements as being gray matter or white matter.

Overview of the continuum model

With the geometric model developed specifically for numerical integration techniques, the next step in our framework is to select a model that accurately predicts how the tissue will deform under various loading conditions specific to neurosurgical

tumor resection. In this work, the poroelastic biphasic model was chosen to simulate the brain tissue biomechanics because of its relative simplicity and because it takes into account the pressure dynamics of the fluid component. The biphasic model proposed by Miga et. al. was used to model the shift deformations [54]. The model was set up in a way very similar to that described in Dumpuri et. al. [2]. The equations of biphasic consolidation are listed below:

$$\nabla \cdot G\nabla\vec{u} + \nabla\frac{G}{1-2\nu}\left(\nabla\cdot\vec{u}\right) - \alpha\nabla p = -\left(\rho_t - \rho_f\right)g \tag{3.1}$$

$$\alpha\frac{\partial}{\partial t}\left(\nabla\cdot\vec{u}\right) + \frac{1}{S}\frac{\partial p}{\partial t} + k_c\left(p - p_c\right) = \nabla\cdot k\nabla p \tag{3.2}$$

The term $\vec{u}$ is the displacement vector, p is the interstitial pressure, G is the shear modulus, ν is the Poisson's ratio, α is the ratio of fluid volume extracted to volume change of the tissue under compression, ρ_t is the tissue density, ρ_f is the fluid density, g is the gravitational unit vector, $1/S$ is the amount of fluid that can be forced into a tissue under a constant volume, t is the time, k_c is the capillary permeability, p_c is the non-homeostatic intracapillary pressure in the event an administered hyperosmotic agent or edema event, and k is the hydraulic conductivity. The equation (3.1) describes the solid phase of the model, which is described by isotropic linear elastic behavior. The equation (3.2) describes the fluid phase of the model, where the pressure gradients are governed by Darcy's law [60]. The material properties were used as stated in Dumpuri et. al. [2] and are listed in the table below.

TABLE 1
MATERIAL PROPERTIES

Symbol	Value	Units
E_{white}, E_{gray}	2100	N/m^2
E_{tumor}	100,000	N/m^2
ν	0.45	no units
ρ_t	1000	kg/m^3
ρ_t	1000	kg/m^3
g	9.81	m/s^2
α	1.0	no units
$1/S$	0.0	no units
k_{white}	1×10^{-10}	m^3s/kg
k_{gray}	5×10^{-12}	m^3s/kg
$k_{c1,\ white}$*	2.3×10^{-9}	Pa/s
$k_{c2,\ white}$*	4.6×10^{-9}	Pa/s
$k_{c3,\ white}$*	6.9×10^{-9}	Pa/s
$k_{c1,\ gray}$*	11.5×10^{-9}	Pa/s
$k_{c2,\ gray}$*	23.0×10^{-9}	Pa/s
$k_{c3,\ gray}$*	34.5×10^{-9}	Pa/s
p_c	-3633	Pa

* These values were used to simulate three different capillary permeability values resulting from the administration of mannitol and are designed to capture a physiological range.

Boundary conditions

While the model of the continuum is critical, the deployment of boundary conditions is equally critical. Following the work by Dumpuri et al. [2], [3], we have elected an approach which pre-computes a range of possible brain deformations which is subsequently fitted to the intraoperative data. Central to that strategy is to generate a systematic method of varying boundary conditions, i.e. an atlas of deformations. The atlas for this work was constructed for two kinds of deformation: deformation caused by gravity, and deformation caused by mannitol - a hyperosmolar drug administered prior to surgery to reduce intracranial pressure. The boundary conditions used for building the atlases are demonstrated in Figure 5 below.

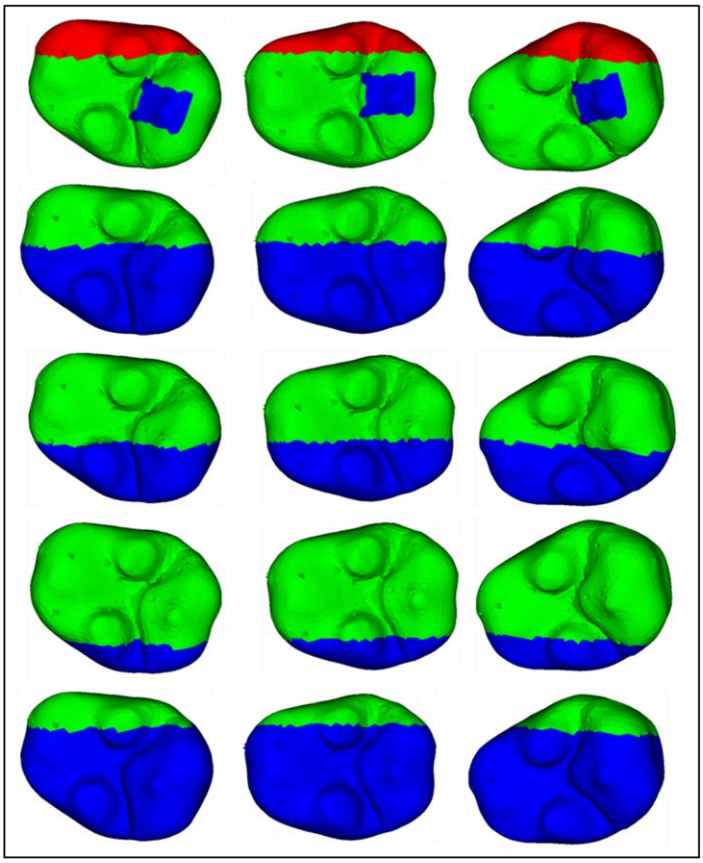

Figure 5: Boundary conditions for running the model. The columns show three different head orientations. The first row shows the displacement boundary conditions, which are same for gravity and mannitol atlases. The red region represents the stress free nodes, green region represents the slip nodes and blue region is comprised of the fixed brainstem nodes. The next three rows represent the pressure boundary conditions for the gravity atlas. The green region represents the nodes at atmospheric pressure (Dirichlet conditions) and the blue region represents Neumann conditions. The demarcation in this case is determined by the presumed level of fluid drainage, and the three different levels were manually designated. The last row shows the pressure boundary conditions for the mannitol atlas. The green region represents the nodes at atmospheric pressure (Dirichlet conditions) and the blue region represents Neumann conditions. The demarcation between the two regions is same as that between the stress free and slip nodes for displacement boundary conditions.

The top row shows the displacement boundary conditions that were solely a function of head orientation and would be the same regardless of mannitol or gravity-induced deformations. It reflects the brainstem (blue region) being fixed, i.e. no deformation. The region associated with the highest elevation on the brain with respect to the head orientation, is designated to be stress free (shown in red). All other nodes on the

boundary, including the internal boundaries (the falx cerebri and the tentorium cerebelli), are assigned slip boundary conditions, that is, they cannot move in the normal direction, but movement in the tangential direction is permitted (shown in green). The demarcation between the stress free and slippage region is a function of the head orientation, the demarcating plane is perpendicular to the direction of gravity and level is set empirically. The next three rows (2,3,4) in Figure 5 show the pressure boundary conditions for gravity deformation condition. The highest nodes in this case are designated to be at atmospheric pressure (green region) and all other nodes (including the internal boundaries of falx and tentorium) are assigned a no-flux pressure condition, that is, there is no pressure gradient across these boundaries (blue region). The demarcation between the atmospheric pressure and no flux boundary condition is done by the presumed level to which cerebrospinal fluid has drained to during the procedure. The mode of deformation is the weight of the exposed tissue pulling down on itself. The pressure boundary conditions for mannitol are shown in last row. The stress free nodes are assigned to be at atmospheric pressure (green region) and all other nodes have a no-flux pressure boundary conditions imposed upon them (blue region). The mode of deformation in this case is the interstitial pressure drawing the fluid into the leaky capillaries. In order to build the atlas, for each patient, different head orientations were used (three of which are represented in the columns of Figure 5). Tissue resection was simulated by decoupling nodes belonging to tumor material type. For the gravity deformations, different fluid drainage levels were used and for mannitol induced deformations, capillary permeability values were varied. The number of deformation solutions in the atlas depended on the number of head orientations, fluid levels and capillary permeability values. The selection of these

numbers was done empirically in the work in Chapter IV, and Chapter V presents an extensive sensitivity analysis to determine the atlas size based on these parameters.

Inverse Model

Intraoperatively, the atlas that was built above would be used to solve the inverse model, driven by sparse data, i.e. LRS data collected during surgery. By pre-computing the solution in this manner, it allows for the rapid solution to intraoperative shift. To guide the selection of the correction, two LRS scans are acquired — one after opening of the dura, and another one after tumor resection. The scanner is tracked during the acquisition of the textured point clouds and hence the two scans can be easily registered to each other by simply putting them in physical space. These two surfaces are registered to the MR images using constrained surface mutual information algorithm discussed in Cao et. al. [39] or using a simple ICP approach [61]. Homologous points are then selected on both the LRS surfaces and these sparse displacements are used to drive the inverse model as described next.

The atlas of displacement solutions computed above are compiled into a matrix E that consists of $3N$ rows and m columns, where N is the number of nodes in the mesh (with each node having a displacement solution in the Cartesian x, y, and z directions) and m is the number of solutions in an atlas. The sum of squared error between the inverse solution and the true solution is defined as following.

$$\varepsilon = \left(E\boldsymbol{\alpha} - \boldsymbol{U}\right)^T \left(E\boldsymbol{\alpha} - \boldsymbol{U}\right) \tag{3.3}$$

In equation (3.3), ε is a sum of squared error between the inverse solution ($E\boldsymbol{\alpha}$ term) and the true measured displacements, $\boldsymbol{U}$. E is the matrix of atlas solutions and $\boldsymbol{\alpha}$ is an $m \times 1$

vector of weighting coefficients. The weighting coefficients can be obtained by the least squared error approach.

$$\boldsymbol{\alpha} = \left(E^T E\right)^{-1} E^T \boldsymbol{U} \tag{3.4}$$

Since the displacement data over the entire domain is unknown and only sparse measurements are available, the above equation is rewritten as follows:

$$\boldsymbol{\alpha} = \left(M^T M\right)^{-1} M^T \boldsymbol{u}_{sparse} \tag{3.5}$$

In equation (3.5), M is the matrix of sparse atlas solutions which is $3n_s$ rows and m columns, n_s being the number of sparse points or previously computed homologous points on the LRS surfaces, where the deformation is known from the tracking of the pre- and post- resection LRS. $\boldsymbol{u}_{sparse}$ is a $3n_s$ vector of those measured displacements. Unfortunately, equation (3.5) is an ill-posed problem. The first term in equation (3.5) is usually near singular because the number of atlas solutions exceeds that of the number of sparse homologous points. This can be resolved by either using a regularization parameter or constraining the problem. In a method employed by Clements et. al. [62] the Tikhonov regularization method was used to solve a similar problem. The sum of squared error residual can be redefined as follows:

$$\varepsilon = \left\| M\boldsymbol{\alpha} - \boldsymbol{u}_{sparse} \right\|^2 + \left\| \beta\boldsymbol{\alpha} \right\|^2 \tag{3.6}$$

In the above equation, β is the Tikhonov factor. The least squared error can be computed as follows:

$$\boldsymbol{\alpha} = \left(M^T M + \beta^2 I\right)^{-1} M^T \boldsymbol{u}_{sparse} \tag{3.7}$$

I is an $m \times m$ identity matrix and β^2 is the Tikhonov factor, which in Joachimowicz et. al. [63] is estimated as

$$\beta^2 = \lambda\, tr\left(M^T M\right) \tag{3.8}$$

λ is a weighting factor and the second term is the trace of the matrix $M^T M$. The Tikhonov factor makes the first term in equation (3.7) in the parenthesis invertible, making it possible to solve that equation.

A second approach involves constraining the problem and using an optimization technique to solve equation (3.5). This technique was used in Dumpuri et. al. [64] and the following constrains were implemented to solve the problem.

$$\min \left\| M\boldsymbol{\alpha} - \boldsymbol{u}_{\boldsymbol{sparse}} \right\|^2 \text{ s.t. } 0 \le \alpha_i \le 1 \text{ and } \sum_{i=1}^{m} \alpha_i \le 1 \tag{3.9}$$

The first constraint ensures that all the weighting coefficients are positive. Hence if a solution in an atlas deforms in the incorrect direction, the objective function would weigh that solution lower instead of assigning a higher negative regression coefficient. The second constraint ensures that the solution is always interpolated, and not extrapolated. The implementation of the active set method for quadratic programming in the Optimization Toolbox of MATLAB® (Mathworks Inc) [65] was used to solve this linear constrained least squared error problem. When comparing the performance of approaches associated with (3.8), and (3.9), it was found that while the data fit with the former was quite nice, often in regions distant from the craniotomy, the results were less satisfying while the latter approach was more consistent and robust.

Overall pipeline

With the framework components designated above, the schematic of the entire process, beginning from image acquisition to the model update in the OR, is shown in Figure 6.

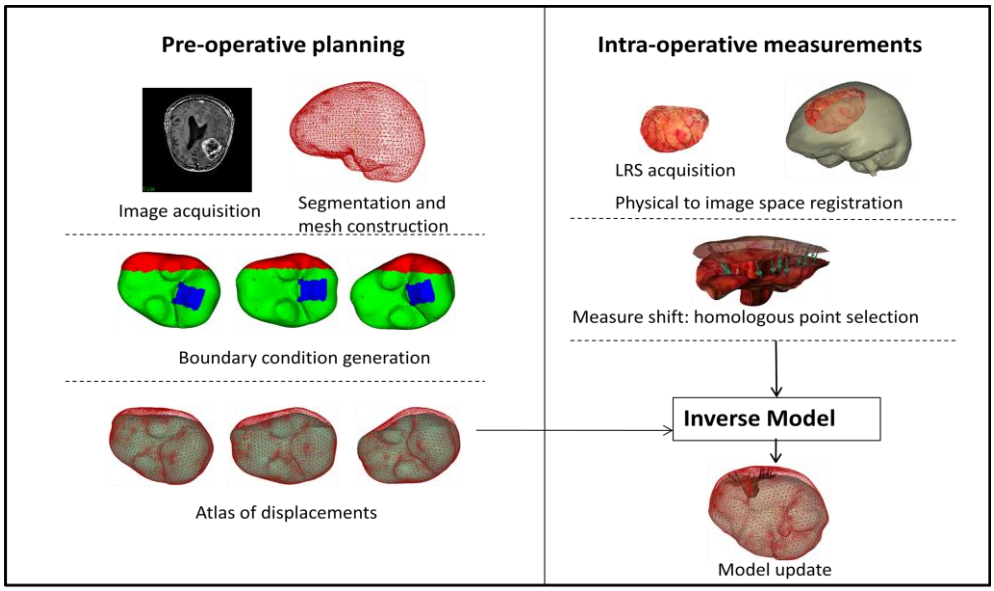

Figure 6: Schematic showing the overall procedure for model updated image guided neurosurgery. The workflow is broadly divided into pre-operative and intra-operative phases. Most time intensive steps are done in the pre-operative phase, i.e. image segmentation and mesh construction. Boundary conditions for each deformation type and generation of model solutions to form the atlas are also done pre-operatively. Some representative displacement boundary conditions are shown- with blue region being the fixed brainstem, red is the stress free region and green represents the slippage boundary conditions. The dural septa (not shown in the figure) are included in the model by assigning them the slippage boundary condition. The intraoperative phase consists of sparse data collection (laser range scans), registration of those scans to image space and obtaining measured shift through homologous points on the pre- and post-resection scans. In the last step, those measurements are used to fit the displacement atlas using an inverse model to obtain the final model updated results.

The atlas-based method for brain shift correction shifts a bulk of the computational burden pre-operatively. After the MR image acquisition, the image is segmented into the brain, tumor and the dural septa and the mesh is constructed. The atlas of deformations is then built by perturbing the boundary conditions and the driving conditions. Intraoperatively, sparse data is acquired for the craniotomy region using a tracked laser

range scanner before and after tumor resection. Homologous points are selected on these serial scans and used to drive the inverse model to obtain deformation information for the entire domain.

One important novel advance in this thesis is towards taking into account surgical retraction forces. Briefly, the integration of retraction into the atlas-based inverse model pipeline is described below.

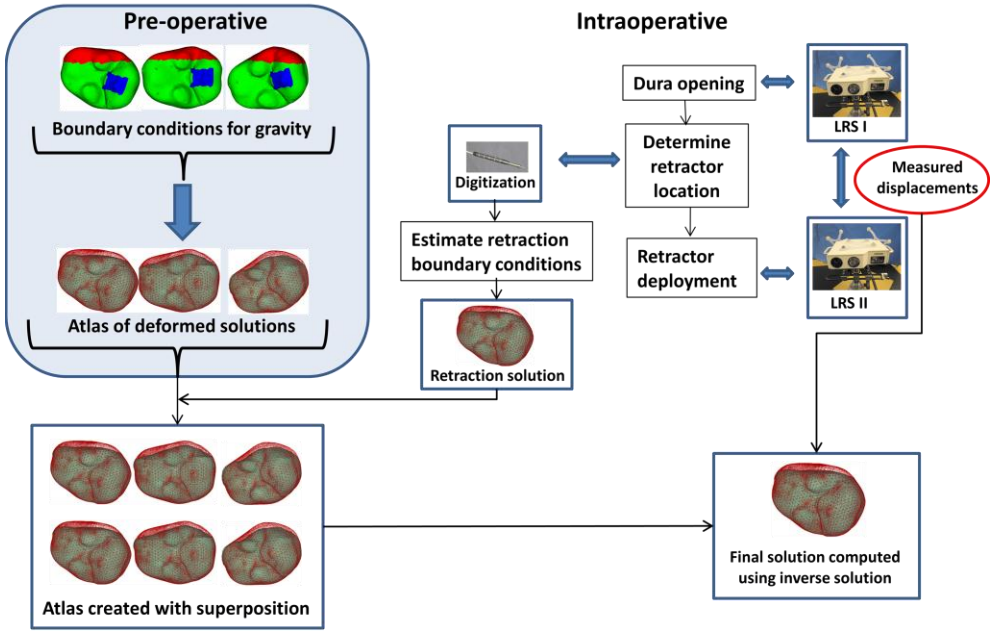

Figure 7. Schematic showing the overall workflow. Preoperatively, the deformation atlas is computed for gravity. Intraoperatively, first sparse data set is acquired after dura removal using a device such as a tracked LRS (measurement marked as LRS I in figure). After the location where the retractor will be placed is determined by the surgeon, the location can be digitized and used to estimate the retractor boundary conditions and construct a retraction model prediction. This can be linearly superposed with the gravity atlas computed pre-operatively to create an atlas that contains solutions both with and without retraction. After retractor deployment, another sparse data set can be acquired. Displacements can be computed from the two surfaces through homologous points and used to inversely solve the model.

In this case, the pre-operative deformation atlas is built as before. Intraoperatively, before the deployment of the retractor, the retractor location is marked with a tracked tool tip, and used for estimating the retractor boundary conditions (in the future, this could be

replaced by having a tracked reference on the retractor like any other guidance tool). The mesh nodes are split along the retractor plane. The side in contact with the retractor is prescribed slip boundary conditions, where the movement in the direction normal to the plane is restricted, whereas it is free to move in tangential directions. The other side of the retractor is prescribed type II stress free boundary conditions. The retractor solution is then appended to the pre-computed deformation atlas. The advantage of the active solution of retraction in the OR is that the location of retraction is not known prior to surgery and the forward model solution restricts the atlas size. Homologous points on the serial laser range scans before and after retraction are then used to drive the inverse model.

Chapter VI will present this new methodology of retraction integration within the atlas-based modeling paradigm in greater detail along with validation experiments of the technique in simulation and phantom data. As with retraction, the deformations associated with resection and tumor debulking are also very challenging. Chapter VII presents a novel yet preliminary work on accounting for resection forces.

CHAPTER IV

MANUSCRIPT 1 — Intraoperative Brain Shift Compensation: Accounting for Dural Septa

Original manuscript: I. Chen, A. M. Coffey, S. Ding, P. Dumpuri, B. M. Dawant, R. C. Thompson, and M. I. Miga, *IEEE Trans Biomed Eng*, vol. 58 (3), pp. 499-508, Mar, 2011

Introduction and Significance of Study

Human brain has a complex anatomy, with structures that affect the biomechanics under surgical loads. In mathematical modeling, the need for accuracy must be balanced with computational efficiency. In this work, a need for modeling the dural septa — the falx cerebri and the tentorium is explored and a technique for segmenting and modeling these structures is studied. Factors such as head orientation, amount of fluid drainage or mannitol administered influence the magnitude and direction of brain shift, but are difficult to measure or quantify to exact precision in the operating room. The atlas-based modeling method was developed to account for the uncertainties in the intraoperative environment and the accuracy of the method was demonstrated with pre- and post-operative data analysis [2, 3]. In this work, the analysis of the atlas-based method was performed with sparse intraoperative data acquired using a tracked laser range scanning device. This work presents some critical observations about the difference of behavior between pre- and post-operative and pre- and intraoperative brain shift analysis.

Abstract

Biomechanical models that describe soft-tissue deformation provide a relatively inexpensive way to correct registration errors in image guided neurosurgical systems caused by non-rigid brain shift. Quantifying the factors that cause this deformation to sufficient precision is a challenging task. To circumvent this difficulty, atlas-based methods have been developed recently which allow for uncertainty yet still capture the first order effects associated with deformation. The inverse solution is driven by sparse intraoperative surface measurements, which could bias the reconstruction and affect the subsurface accuracy of the model prediction. Studies using intraoperative MR have shown that the deformation in the midline, tentorium, and contralateral hemisphere is relatively small. The dural septa act as rigid membranes supporting the brain parenchyma and compartmentalizing the brain. Accounting for these structures in models may be an important key to improving subsurface shift accuracy. A novel method to segment the tentorium cerebelli will be described, along with the procedure for modeling the dural septa. Results in seven clinical cases show a qualitative improvement in subsurface shift accuracy making the predicted deformation more congruous with previous observations in literature. The results also suggest a considerably more important role for hyperosmotic drug modeling for the intraoperative shift correction environment.

Introduction

Image guidance found its earliest applications in neurosurgery and it is the standard of care today for the surgical treatments of central nervous system neoplasia,

epilepsy and cerebrovascular disorders. The fidelity of image to physical space registration is central to image guided neuronavigation and is known to be compromised by the phenomenon of brain shift, deformation of brain tissue caused by gravity, edema, hyperosmotic drugs administered prior to surgery, and tissue resection. Systematic studies to characterize this deformation have been performed with the aid of intraoperative digitization and have found that the range of deformation for brain tissue could vary from 1cm to 2.5 cm from their pre-operative state during surgery [5, 7]. A trained neurosurgeon is aware of the misalignment between the surgical field and the preoperative image and compensates for it to some extent [9] but guidance systems capable of compensation would be very desirable.

Extensive work has been reported in the literature to compensate for brain shift. One strategy is to use intraoperative imaging techniques such as CT [12], MRI [5], and ultrasound [28]. Although intraoperative imaging captures a great deal of anatomical shift, the wealth of preoperative data cannot be updated during surgery. As a result the brain shift literature has also demonstrated a need for preoperative to intraoperative data registration via computational approaches. Hata et. al. used non-rigid registration between preoperative and intraoperative MR images with a mutual information metric [30]. Biomechanical models using discretized methods (such as finite element techniques) have been explored by many groups for this problem. Hagemann et. al. performed a 2D analysis using a linear elastic model driven by surface displacements computed using active contours method [31]. Ferrant et. al. followed a similar approach and extracted the surface of the cortex and ventricles for the preoperative and intraoperative MR images and used an iterative shape matching algorithm to compute the

surface displacements [32]. Wittek et. al. obtained displacement information from intraoperative MR data and obtained volumetric displacement by applying a nonlinear model [33]. Clatz et. al. used a block matching algorithm instead of surface information to drive their computer-model based approach [34]. It should be noted that all of the above listed methods require an intraoperative MR scan, and while all are important contributions, those devices are not widely available due to high cost of operation, a cost that could represent monetary, radiation exposure (in case of CT), and/or cumbersomeness.

A more cost effective alternative to volumetric intraoperative images is to use sparse data, which does not require the installation of expensive tomographic devices in the operating room (OR). Stereoscopic cameras and laser range scanners are two devices in this category and have been used extensively to capture cortical surface data. The former involves a pair of charge-couple device (CCD) cameras attached to the stereoscopic microscope. Triangulation is used between corresponding homologous points to estimate the surface coordinates. The latter method involves a laser source and CCD camera. It works by propagation of a laser onto the brain surface and with its acquisition via CCD, followed by the triangulation of the range of the surfaces. The method further involves the systematic translation of the laser light and a complete surface description of the object of interest can be constructed. With respect to the stereo method, Skrinjar et. al. and Sun et. al. have used this technique to compute and compensate for intraoperative brain shift [35, 36]. With the laser range scanner (LRS) method, there have been several investigations involving the evaluation of rigid registration [37-39] and the measurement of non-rigid brain shift [40, 41].

While methods to measure the cortical surface are improving, having accurate updated subsurface information to delineate the remainder of tumor margin prior-to, during, and after a resection would dramatically improve the utility of image-guided surgery systems. Interestingly, for the same reasons that make biomechanical models a compelling methodology with intraoperative MR data, they are a promising avenue to pursue for an intraoperative updating strategy using sparse data. In the past decade, the growth in this literature and approach has been quite significant. Sun et. al. used a stereoscopic microscope to estimate the 3D cortical surface and registered it to the preoperative image for guidance in the OR [36]. Paul et. al. used automatic landmark extraction for registering the stereoscopically reconstructed surfaces and computing the non-rigid displacements [66]. Dumpuri et. al. used a statistical model driven by sparse laser range scan data to correct for brain shift [2].

While many approaches are being pursued, the work reflected in this paper uses the approach described by Dumpuri et. al. [2]. In this approach, an atlas of solutions that accounts for shift caused by gravity, edema, and mannitol with different head orientations and capillary permeabilities is computed. As a general characterization, the inverse solution is reconstructed by minimizing the least squared error between the solutions and the measurements made with sparse data. This method has been validated thus far using pre-operative and immediate-postoperative MR data and the predictions were found to account for 85% of subsurface shift using surface data only (similar accuracies have been found for subsurface predictions) [3].

While this work was quite compelling, it still does not represent an assessment of the technique during the intraoperative state. In this study, a modified approach to the

atlas correction is investigated within the context of true intraoperative shift correction. Results are reported that reflect the difference in the magnitude of deformation occurring intraoperatively as opposed to the pre- and post-operative measurements used in the Dumpuri et al. study. While intraoperative MR imaging capabilities are not available at our institution, valuable insight into the degradation of an intraoperative updating process can be observed when compared to the findings of Dumpuri et al.

Another important contribution of this paper is studying the sensitivity of brain shift compensation to models that include the dural septa. Briefly, the dura, the outermost meningeal layer, reflects inwards in four places in the brain forming the falx cerebri, tentorium cerebelli, falx cerebelli and diaphragma sellae. These strong structures support the brain parenchyma, preventing large deformation in the contralateral hemisphere, hindbrain and midbrain. Our hypothesis is that with sufficient understanding of the first order deformation effects in the brain, surface shift measurements in the craniotomy region are sufficient to compensate for volumetric shift. In this work, it is suggested that the dural septa are crucial components for accurately predicting subsurface shift. To lend rationale, Ferrant et. al. found that the greatest subsurface error in their model lied at the mid-sagittal plane, the location of the rigid membrane, falx cerebri [32]. In their approach to correction, a homogeneous elastic model was used with no accounting of dural septa. Similar reports using intraoperative MR have also shown that relatively little deformation is observed in the regions around the midline, tentorium and contralateral hemisphere [67]. In previous work by Miga et al. [68] the modeling of the falx cerebri was described and was utilized in [2, 3, 69]. However no systematic study has been reported that demonstrates the influence of these septa on the performance of

intraoperative shift compensation. The goal of this work is to systematically study the effect of the dural septa on subsurface brain shift and assess the need to model these structures within the context of acquired intraoperative shift data in seven cases.

Methods

Data acquisition

Preoperative MR tomograms were acquired for seven patients using a 1.5 T clinical scanner a day prior to undergoing tumor surgery. The acquired images were T1 weighted and Gadolinium enhanced with voxel size of 1mm × 1mm × 1.2mm. Demographic and other intraoperative information is compiled in Table 2.

TABLE 2: Patient information. Tumor locations L: left or R: right signify the hemisphere, followed by the lobe- F: frontal, P: parietal or T: temporal. Tumor pathologies described by the grade (ranging from I to IV) and types- olig: oligodendroglioma, astro: astrocytoma, met: metastatic tumor, GBM: glioblastoma multiforme. Orientation: IS- refers to rotation about inferior-superior axis (eg. IS 90 deg reflects patient's head parallel to the floor)

#	Age (yrs), gender	Tumor location	Tumor pathology	Lesion size (cm)	Craniotomy diameter (cm)	Head orientation in the OR
1	22,F	L,F	Gr(II) Olig.	5.2×6.2×6.0	7.7	IS 90 deg
2	52,M	L,F	Astro.	4.9×5.6×5.0	8.3	IS 90 deg
3	58,M	L,P	Met.	3.7×3.5×4.1	4.7	IS 135 deg
4	77,M	L,T	Gr(IV) GBM	3.4×3.6×2.0	5.0	IS 90 deg
5	75,F	L,T	Gr(II) GBM	5.0×5.0×5.0	6.1	IS 90 deg
6	46,M	R,T	Gr(IV) GBM	3.0×3.0×3.0	4.3	IS 90 deg
7	27,M	L,T	Gr(IV) glioma	6.9×4.0×4.0	9.0	IS 90 deg

Patient consent was obtained prior to surgery for this Vanderbilt Institutional Review Board approved procedure. After the craniotomy, an optically tracked commercial LRS device (RealScan3D USB, 3D Digital Corp, Bethel, CT) was used to obtain cortical surface scans immediately after the opening of the dura and after tumor resection.

Figure 8. Left- laser range scanner performing a scan during surgery. Right- scanner mounted on arm being tracked by camera on right

The scanning device shown in Figure 8 records the cortical surface shape and color texture of the surface which facilitates the intraoperative measurement of brain shift. This has been reported extensively in [39, 40]

Mesh Construction

Patient specific meshes were created individually from MR images of the patient. Brain and tumor surfaces were manually segmented and subsequently processed using the marching cube algorithm [57] with a Laplacian smoothing function. [58]. Once the surfaces were extracted, a tetrahedral mesh was created [59] that typically consisted of approximately 20,000 nodes and 100,000 tetrahedral elements. An image-to-grid intensity threshold method was then used to classify the brain parenchyma elements into gray and white matter [70].

Falx cerebri and the tentorium cerebelli are the two important sub-structures of the dural septa and different segmentation techniques were used for each of them. The falx was segmented manually and meshed in a manner similar to that described in Miga et. al. [68]. Briefly, using the sagittal view of the patient's image volume, a patient-

specific plane is created. This plane is then used to split the tetrahedral domain and then boundary conditions consistent with the constraint of the falx are applied (discussed in greater detail in section II. C). This procedure is shown in Figure 9.

(a) 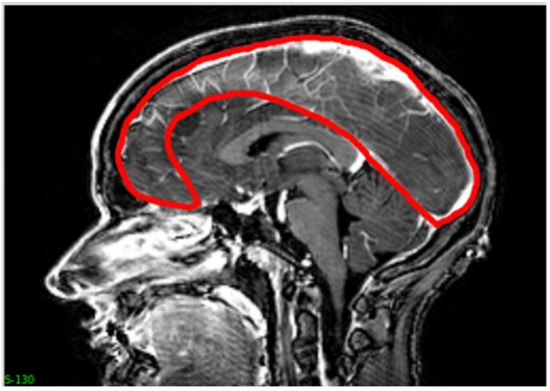 (b) 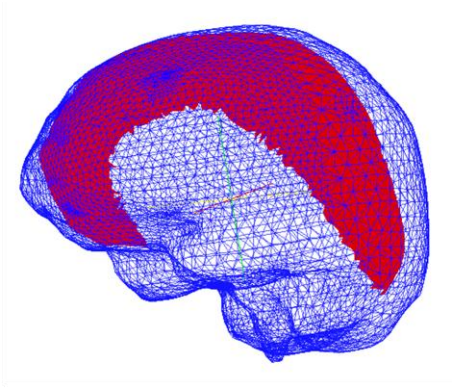

Figure 9. Falx segmentation procedure. (a) Manual periphery drawn around falx on gadolinium enhanced MRI (b) segmented falx overlaid with the mesh.

With respect to the tentorium region, the invagination encloses the straight sinus which is visualized as a high intensity region in the gadolinium enhanced images. In this region, a limited series of points were selected and a 3D thin plate spline algorithm was used to morph a plane into a tentorium surface, which was then smoothed. The tentorium cerebelli in the contralateral hemisphere was segmented similarly. Those surfaces were then used to create tentorium structures in the finite element mesh. This procedure is demonstrated in Figure 10 (a)–(e).

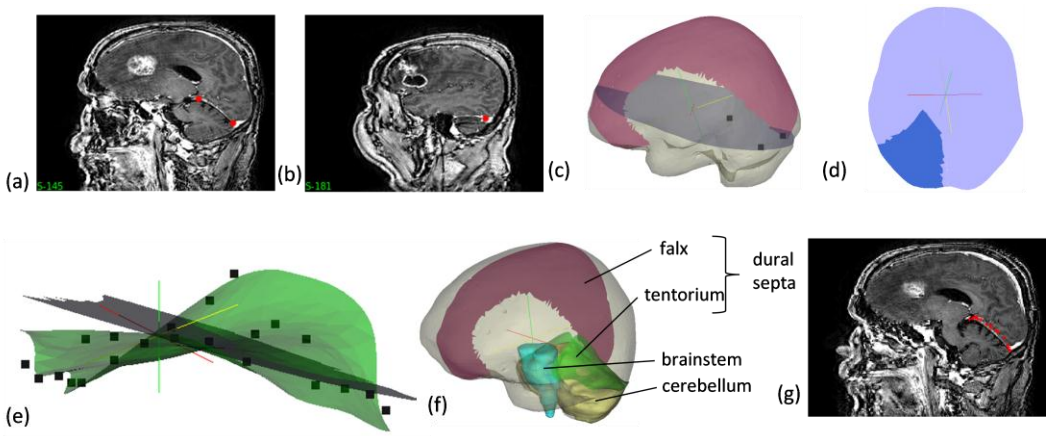

Figure 10. Procedure for tentorium segmentation. (a) and (b) show the selection of three points used for clipping a plane in the mesh, (c) shows the clipped plane (with those three points) overlaid with the mesh and the falx, (d) shows the clipped plane segmented into an approximate tentorium shaped structure and (e) shows the segmented plane with the final tentorium surface created by morphing the plane in (d) using a thin plate spline algorithm. The points on the surface are the target points used to drive the thin plate spline algorithm. (f) shows the mesh overlaid with the segmented falx and the tentorium surfaces. The segmented brainstem (in blue) and cerebellum (in yellow) are shown for reference, were not modeled separately. (g) is the sagittal MRI slices overlaid with the red points of the tentorium surface. A good overlap of the points and the hyperintense region indicate the quality of segmentation.

The quality of the segmentation was assessed visually by overlaying the tentorium points on the gadoliunium enhanced images as shown in Figure 10 (g). These overlays suggest that the overall patient specific segmenation of the tentorium is representative for modeling purposes.

Computational Model and Atlas Generation

The biphasic model proposed by Paulsen et al. was used to model the shift deformations [71]. The model was set up similar to that described in Dumpuri et. al. [2] and the details are provided here for completeness. The equations of biphasic consolidation are listed below:

$$\nabla \cdot G\nabla\vec{u} + \nabla \frac{G}{1-2\nu}\left(\nabla \cdot \vec{u}\right) - \alpha\nabla p = -\left(\rho_t - \rho_f\right)g \tag{4.1}$$

$$\alpha \frac{\partial}{\partial t}\left(\nabla \cdot \vec{u}\right) + k_c\left(p - p_c\right) = \nabla \cdot k\nabla p \tag{4.2}$$

The term $\vec{u}$ is the displacement vector, p is the interstitial pressure, G is the shear modulus, ν is the Poisson's ratio, α is the ratio of fluid volume extracted to volume change of the tissue under compression, ρ_t is the tissue density, ρ_f is the fluid density, g is the gravitational unit vector, t is the time, k_c is the capillary permeability, p_c is the intracapillary pressure, and k is the hydraulic conductivity. The material properties were similar to the ones used in Dumpuri et. al. [2] and are listed in Table 5 in the Appendix A.

The collection of deformations computed using different driving conditions for the model is termed an atlas. The atlas was constructed for two kinds of deformation: deformation caused by gravity and deformation caused by mannitol, a hyperosmolar drug administered prior to surgery to reduce intracranial pressure. The boundary conditions used for building the atlases are described in [3]. For the above two deformation types, three different displacement boundary conditions were used — fixed, stress free, and slippage. The brainstem experiences no deformation and is assigned fixed Dirichlet boundary conditions. The highest region on the head, according to the head orientation, is designated to be stress free. All other nodes on the boundary, including the internal boundaries (the dural septa), are assigned slip boundary conditions, that is, they cannot move in the normal direction, but movement in the tangential direction is permitted. The demarcation between the stress free and slippage region is done according to the head orientation, the demarcating plane is perpendicular to the direction of gravity and level is set empirically. The pressure boundary conditions were set by the presumed level to

which cerebrospinal fluid has drained during the procedure. With respect to our methods, multiple fluid drainage levels are included as part of the deformation atlas strategy described by Dumpuri et al. in [3]. The nodes exposed to atmospheric pressure are set as a Dirichlet boundary condition and the nodes submerged in fluid are subject to Neumann boundary conditions, i.e. non-draining surfaces. In order to build the atlas, for each patient, 60 different head orientations were used (three of which are represented in the columns of Figure 11). Since the entire head is draped except for the craniotomy region, it makes it challenging to ascertain the exact head orientation. An approximation of the head orientation can be obtained from the surgeon's pre-operative plan. From that base orientation, vectors can be populated around that base orientation to deal with the various changes to OR patient configuration (e.g. in our experience, the surgeon can often elect to change bed tilt and even roll during a case). Tissue resection was simulated by decoupling nodes belonging to tumor material type. For the gravity deformations, three different fluid drainage levels were used, counting for mesh with and without tumor resection, resulted in 360 solutions. For mannitol induced deformations, three different capillary permeability values were used with the 60 head orientations, also resulting in 360 different solutions in the atlas. This resulted in a combined atlas with 720 gravity and mannitol concatenated solutions. In addition, the deformations were further investigated with the construction of two atlases for shift compensation use, one that contained the dural septa and one that did not.

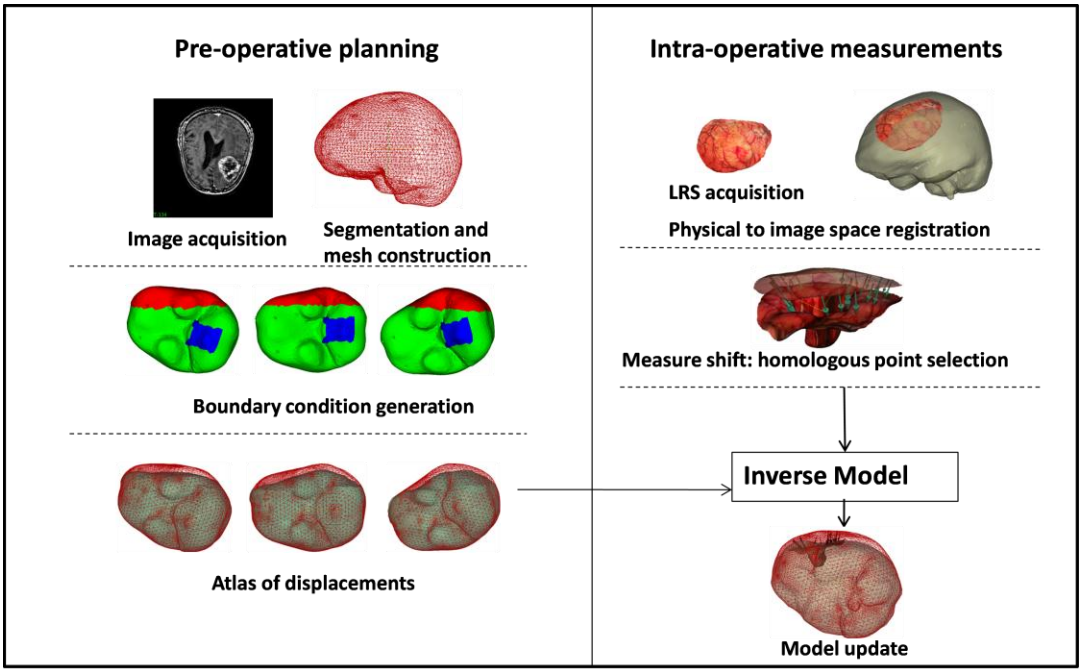

Figure 11. Schematic showing the overall procedure for model updated image guided neurosurgery. The workflow is broadly divided into pre-operative and intra-operative phases. Most time intensive steps are done in the pre-operative phase, i.e. image segmentation and mesh construction. Boundary conditions for each deformation type and generation of model solutions to form the atlas are also done pre-operatively. Some representative displacement boundary conditions are shown- with blue region being the fixed brainstem, red is the stress free region and green represents the slippage boundary conditions. The dural septa (not shown in the figure) are included in the model by assigning them the slippage boundary condition. The intraoperative phase consists of sparse data collection (laser range scans), registration of those scans to image space and obtaining measured shift through homologous points on the pre- and post-resection scans. In the last step, those measurements are used to fit the displacement atlas using an inverse model to obtain the final model updated results.

Inverse Model

Although this is a retrospective study, all the atlas construction work listed above would be part of the preoperative planning and would be performed prior to surgery. Intraoperatively, the atlas that was built prior to surgery would be used to solve the inverse model, driven by sparse data, i.e. LRS data collected during surgery. Since model solutions are performed preoperatively, the intraoperative compensation is very fast and takes into account the variability within the OR (e.g. uncertain cerebrospinal fluid (CSF) drainage levels, varying head orientations as a patient's bed is rotated, etc).

For the correction process, two LRS scans need to be acquired, one after opening of the dura and another one after shift has occurred. The scanner is tracked during the acquisition of the textured point clouds and hence the two scans can easily be registered in the same physical space. These two surfaces are registered to the preoperative MR images using constrained surface mutual information algorithm discussed in Cao et. al. [39]. The schematic of the entire process is shown in Figure 4. Homologous points are then selected on both the LRS surfaces and these sparse displacements are used to drive the inverse model as described below.

The displacement solutions computed above are compiled into an atlas. Since the true deformation over the entire domain is unknown, only sparse comparisons can be evaluated. An inverse solution is obtained by the minimization of least squared error between the predictions and the measurements. However this would result in an ill-posed problem since the number of atlas solutions far exceeds the number of sparse homologous points. This can be resolved by constraining the problem as done in [64], resulting in the following equation.

$$\min \left\| M\boldsymbol{\alpha} - \boldsymbol{u}_{\boldsymbol{sparse}} \right\|^2 \text{ s.t. } \alpha_i \geq 0 \text{ and } \sum_{i=1}^{m} \alpha_i \leq 1 \qquad (4.3)$$

The atlas matrix M consists of $3n_s$ rows and m columns. Here 'n_s' is the number of sparse points or previously computed homologous points on the LRS surfaces, where the deformation is known from tracking the pre- and post- resection LRS, with each point having a displacement solution in the Cartesian x, y, and z directions. $\boldsymbol{u}_{\boldsymbol{sparse}}$ is a $3n_s$ vector of those measured displacements.

This method is different than what was reported by Dumpuri et al. in [3] where no constraints were applied. The first constraint ensures that all the weighting coefficients

are positive. Hence if a solution in an atlas deforms in the incorrect direction, the objective function would weigh that solution lower instead of assigning a higher negative regression coefficient. The second constraint prevents the solutions from being extrapolated, which can cause inaccuracies in the predicted displacements in the far field. The implementation of the method of Lagrange multipliers in the Optimization Toolbox of MATLAB® (Mathworks Inc) was used to solve this linear optimization problem. This is in contrast to the Dumpuri et al. technique which used a Tikhonov-like regularization approach. While the analysis by Dumpuri et al. using pre- and post-MR data did not reflect far-field inaccuracies in the displacements, this was not found to be the case when using the larger and more considerable dynamic shift data from the intraoperative environment.

Results

Shift was measured across seven cases through homologously selected points on registered pre- and post-resection LRS images. The average and maximum magnitude of measured shifts for each of the patients at the homologous points are listed in Table 3. For completeness, the measurements of shift as provided by the pre- and post-MR study by Dumpuri et al. study [3] are provided for reference.

TABLE 3: The average and maximum measured intraoperative displacements. The measured shift from pre- and post-operative MR analysis from [3] is also listed for comparison. The analysis was unavailable for patients 3 and 7.

#	Number of measurement points	Intraoperative LRS: average shift ± standard deviation (maximum) in mm	Postoperative MR: average shift ± standard deviation (maximum) in mm from [20]
1	16	22.9±6.3 (28.9)	8.2±2.2 (12.2)
2	22	14.3±5.1 (29.1)	9.2±1.3 (11.6)
3	24	6.8±2.4 (10.5)	-
4	18	8.6±0.6 (9.7)	5.4±0.9 (7.0)
5	22	13.0±2.1 (15.9)	5.3±0.8 (6.8)
6	17	8.6±2.0 (13.2)	5.3±0.9 (7.1)
7	15	8.8±2.0 (12.1)	-

Percentage shift correction was measured using the formulation listed in Dumpuri et. al. [2].

$$Shift\ correction = \left(1 - \frac{Shift\ error}{Shift\ magnitude}\right) \times 100\% \tag{4.4}$$

In the above equation, shift error is the error in measured and estimated points. The average shift correction for the mesh without the inclusion of the dural septa is 68±17% and for the mesh with the septa is 75±12%.

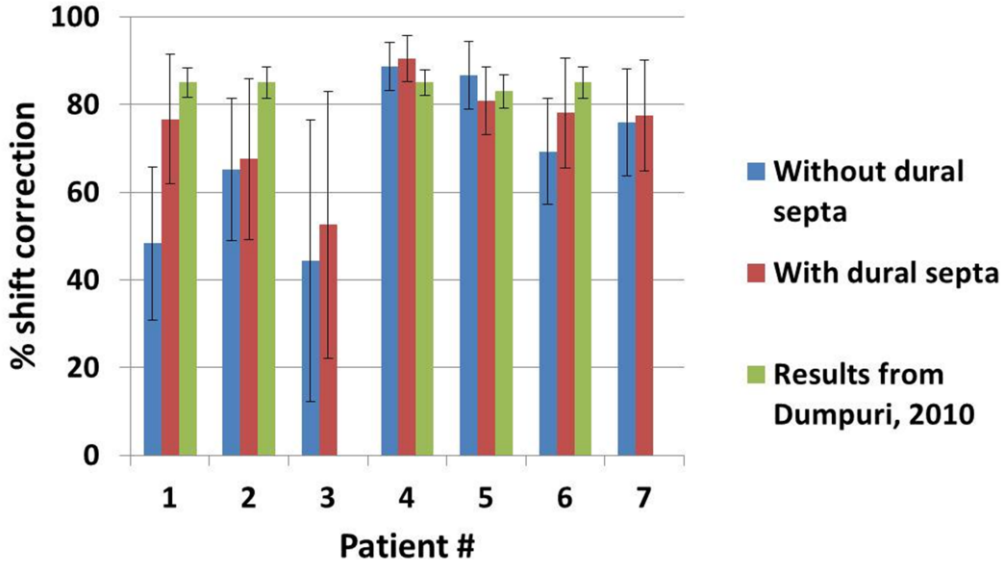

Figure 12. Shift recoveries for seven patient cases for meshes with and without dural septa. Also shown are the shift recoveries obtained for the corresponding pre- and post-operative MR data from [3]. That analysis was unavailable for patients 3 and 7.

In order to determine if there was a statistically significant difference in the shift corrections predicted by using the mesh with or without the dural septa, paired testing was performed. The expected value and variance were unknown due to the small sample size, hence Lilliefors test was used to determine whether the distribution was normal [72]. The test supported the hypothesis that the intraoperative data for both the models, with and without the dural septa, followed a normal distribution ($p>0.05$) and hence the student t-test was used for the paired comparison. The results of the student t-test indicated that there was no statistical difference ($p>0.05$) between the reconstructed atlas solutions for the mesh with or without dural septa.

For completeness, the shift recoveries obtained from the pre- and post-operative MR analysis [3] are also shown in Figure 12 for the corresponding patients. That data was available for five of the seven cases. The average shift correction across the five cases was 85±1%. It is evident that larger shift recovery was obtained with the post-operative MR data as compared to the intraoperative data. The variance amongst cases was also smaller for the post-operative MR data.

Patient 1 and Patient 3 in Figure 12 were noteworthy for the large difference in shift correction between the septa and septa-free models and the smallest shift correction overall, respectively. These two patient cases are discussed in greater detail. Whereas the average difference in percent shift correction in the remaining six patient cases for the mesh with and without the dural septa was 5±3%, the difference in shift correction for the Patient 1 was 28%. The average error in magnitude for the measurement points for the mesh without dural septa was 11.5±4.9 mm and for the mesh with the septa was 5.4±3.9 mm. The average angular error was 21.0±11.4° and 7.1±6.2°, respectively. The

measurement vectors and the predicted vectors for the two models are shown in Figure 13.

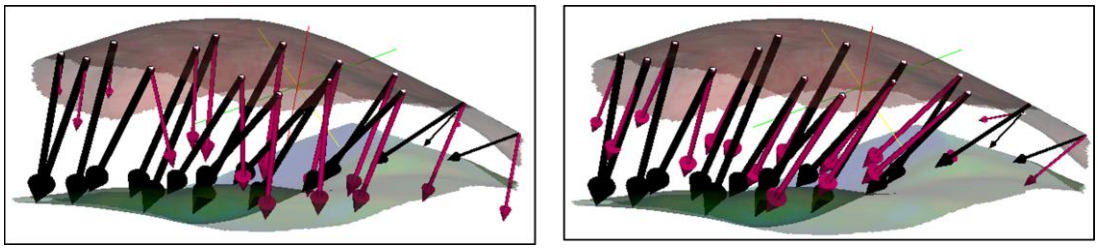

Figure 13. Measured shift vectors (black) and predicted shift vectors (magenta) for the concatenated atlas using the method of constraints for above: model without dural septa and below: model with dural septa. Vectors are overlaid with the pre-resection (top) and post-resection (bottom) LRS surfaces.

Though deformation magnitudes (as opposed to the magnitude of the error vector) were similar for both cases the angular error was much larger for the mesh without dural septa.

Patient 3 had the lowest overall shift correction. The average error in magnitude for the measurement points for the mesh without septa was 3.4±1.9 mm and for the mesh with septa was 3.1±2.2 mm. The average angular error was 31.9±24.9^{o} (maximum of 96.0^{o}), and 25.3±24.8^{o} (maximum of 85.2^{o}), respectively. Figure 14(a) shows the overlay of the undeformed mesh with the post resection LRS surface and the measured displacement vectors on the selected points.

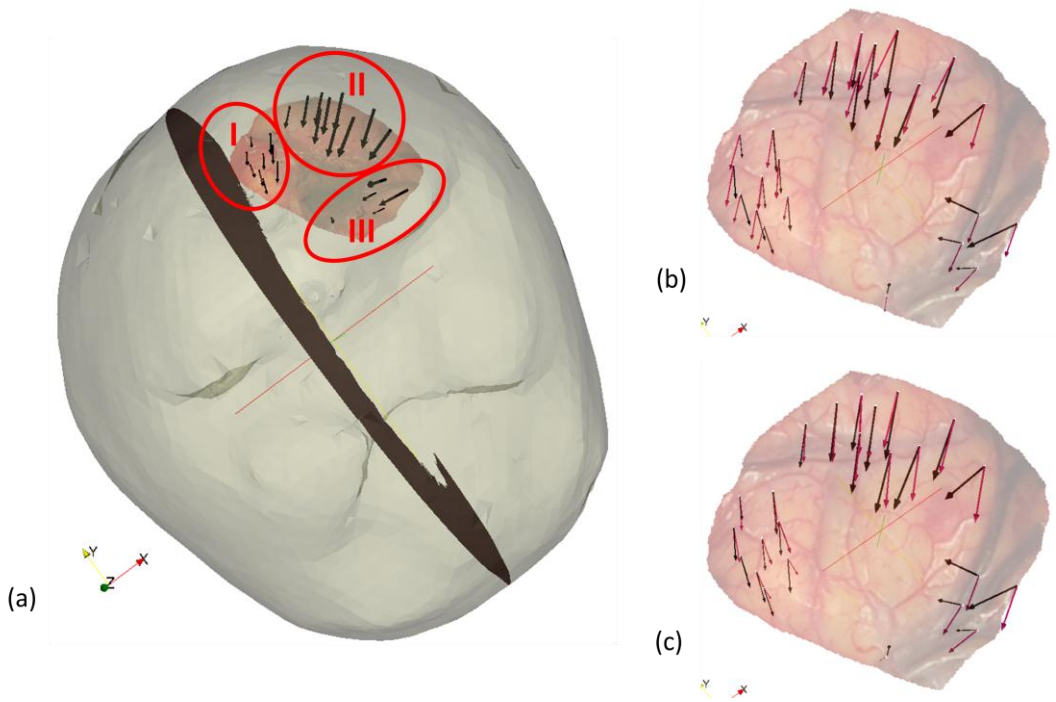

Figure 14. (a) The mesh surface overlaid with the post resection LRS and measurement vectors. The homologous points are divided into three different regions, I, II and III. Pre-resection LRS overlaid with the measurement vectors and the predicted vectors for the (b) model without dural septa and (c) model with dural septa for the concatenated atlas.

The tumor was located in the parietal lobe and the patient was in prone position in the OR, with their head tilted approximately 45° to the dorsal-ventral axis. The selected points for shift measurement could be divided into three distinct clusters (marked I, II, and III in the figure) based on their location and direction of movement. All three clusters were moving towards the center of the resection hole. In the plane that it is being viewed, region I points slide along the falx, region II points move downwards towards the bottom of the plane and region III almost move inwards into the plane. Figure 14(b) shows the predicted vectors for the concatenated atlas for the mesh without septa and Figure 14(c) shows the same for the mesh with septa. The movement towards the center of the hole was not well modeled with the current boundary conditions and is focus of future work.

The average angular and magnitude error for each of the regions for both models are summarized in Table 4.

TABLE 4: Errors in magnitude and angle for the two models using the method of constraints for the concatenated atlas. I, II and III represent the three regions for selected points shown in Figure 14(a)

	Mesh without dural septa		**Mesh with dural septa**	
	Magnitude (mm)	Angle (degrees)	Magnitude (mm)	Angle (degrees)
I	2.5±0.6	29.2±11.1	1.8±0.6	13.7±8.6
II	2.9±1.5	13.4±9.9	2.9±2.0	15.1±12.8
III	6.0±1.9	71.0±19.8	5.8±2.4	66.6±18.9

In general, in both cases, angular error is highest for region III. The applied forces (pressure gradients or gravity) to the model pull the tissue downwards while resection forces pull the tissue inwards. The latter effect is not captured well by the model. There is no statistical difference in the angular error for regions II and III ($p>0.05$). However, region I points have considerably less angular error for the mesh with the dural septa than the one without ($p<0.05$). Region I points are most proximal to the falx, and the sliding along the falx plane is captured by the mesh where the falx is accounted for in the model. A slice of the model deformed image for each model for Patients 1 and 3 are shown in Figure 15.

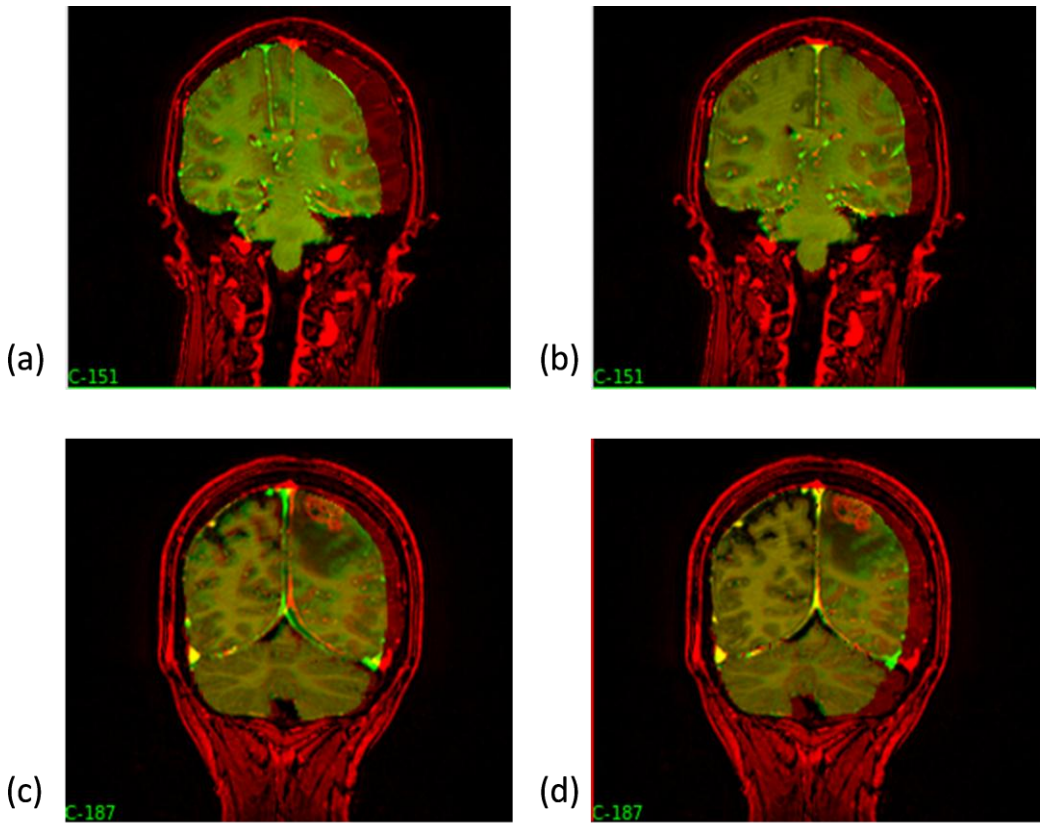

Figure 15. Preoperative image (red) overlaid with model deformed image (green) for the model without dural septa, (a) and (c), and the model with dural septa, (b) and (d). (a) and (b) are the results for Patient 1 and (c) and (d) are results for Patient 3.

Figure 15(a) and 15(b) show the mesh without and with the septa respectively for Patient 1. The hyperintense regions in the center of the image represent the sinus enclosed in the falx cerebri. For the mesh without the septa, there is considerable movement in the position of the falx, whereas the midline stays steady for the mesh with the septa. The overall subsurface shift prediction for the mesh with and without the dural septa is noticeably different for this case. Figure 15 (c) and 15 (d) shows the images updated with the inverse solution for both models respectively for Patient 3. Similar to Patient 1, movement is seen along the midline region along falx and the tentorium in the mesh without the septa whereas those regions do not move as much where the dural septa were modeled. The movement in the midline is greater for Patient 1 without dural septa than

Patient 3 without septa because the overall shift is much higher. During surgery the vicinity of the tumor would be the region of greatest interest for the surgeon and accuracy of the guidance system in that region would be most critical. To examine the difference in subsurface shift caused by the introduction of dural septa in the model, color coded vector differences in the shift predictions of the tumor boundaries for the two models are shown in Figure 16.

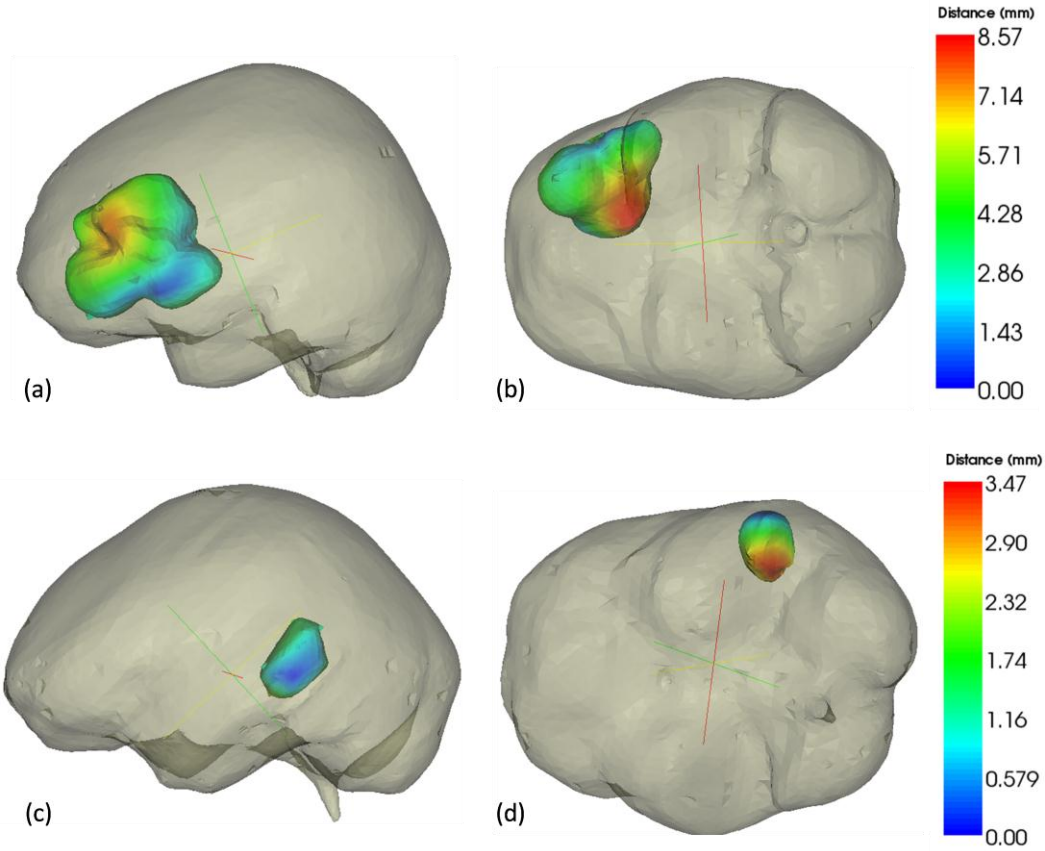

Figure 16. Color coded vector difference in predicted displacements for model with and without the dural septa. The top row figures are representation for Patient 2 and lower row is representation for Patient 4. Two different camera angles have been shown for each patient for better visual clarity.

Each row shows two different views for a different patient dataset — Patient 2 in top row and Patient 4 in bottom row. As seen in Patient 2, the subsurface differences can be as large as 9 mm. As is the case for comparison presented in Figure 8, the difference in the

magnitude of shift prediction is higher when overall measured shift was larger. Also, in each case, largest magnitude of difference in shift prediction is seen at the bottom of the tumor cavity, away from the brain surface.

Discussion

The fidelity of an intraoperative guidance system in neurosurgery is compromised due to shift in the OR caused by various factors such as gravity, hyperosmolar drugs, and edema. A considerable body of work in literature has focused on solving this problem through intraoperative imaging or updating preoperative images with mathematical models. This paper builds upon the previous work of Dumpuri et. al. [2, 3], where an atlas of solutions was used in order to compensate for the inherent uncertainty in the OR. That work was validated using postoperative MR scans and this work explores some differences between postoperative and intraoperative data. A novel model employing the two major dural membranes- falx cerebri and tentorium cerebelli was described and systematically studied in this work. No statistical difference was observed in the overall surface shift correction when comparing the results for the mesh with and without the dural septa. However when the dural septa are accounted for in the model the subsurface deformations are in greater compliance with the observations made in previous literature. This point while subtle is quite important. The results of our statistical test comparing percent surface correction in Figure 12 indicate that the fitting process with or without the septa is statistically the same. This does not say that difference in subsurface shift is negligible, in fact quite the contrary in light of Figure 16. This emphasizes that for our hypothesis to be true, in practice, accurate modeling is important. Based on the literature,

Maurer et. al. [67] observed that the deformation was very small in the midline, tentorial, and contralateral hemisphere regions and Ferrant et. al. [32] noted that the largest errors in model predictions were seen in the midline region. Our dural septa models are consistent with these findings. The lack of intraoperative MR data makes it difficult to perform a more quantitative comparison of the subsurface shift across all cases. However the analyses presented in Figures 14 (b) and 14 (c) and Table 4, as well as the qualitative results presented in Figure 16, strongly support the need to account for the septa in the model.

Some interesting differences were observed between the postoperative MR results reported by Dumpuri et. al. [3] and the intraoperative results presented in this paper. Dumpuri et. al. reported an average shift correction of 85% across 8 patient cases (ranging from 83% to 89%). In this work, the average shift correction across 7 patient cases was 75% (ranging from 53% to 90%) for the mesh with dural septa. The reason for better shift correction in postoperative MR analysis could be the nature of the data. The postoperative MR images were acquired a day or two after surgery and some shift recovery occurred during that period and thus the measured shift magnitudes presented were smaller when compared to the intraoperative measurements presented in this work. This can be seen by comparing the magnitude of the measured shift for intraoperative LRS data and postoperative MR data in Table 3 that demonstrates recovery ranges between 35-65%. The correlation between measured deformation magnitude and shift correction was to some extent observed within the intraoperative data as well. The inclusion of dural septa in the model has a larger impact on the predicted results if the observed shift was larger. For instance, in Figure 15, there was a more dramatic

movement along the mid-sagittal region in the case with the larger measured shift. In Figure 16 the difference in predicted shift was larger between the model with and without the dural septa for the case with larger measured shift as well. The intraoperative data also reflects more dynamic interactions such as tissue resection. The postoperative data might yield better results because it does not have the irregularities caused by local effects nor the considerably larger extent of shift. The cases with the best shift correction had the smallest variation within the measurement vectors i.e. they were of similar magnitude, moving uniformly in one direction. Patient 3 had a large variability and performed poorly with shift correction whereas Patient 4 had a smaller variability in measurements and performed quite well with the shift prediction. The results presented suggest that more considerable resection holes affect the angular variability of shift and provides impetus for a more accurate tissue resection model. Our current strategy to simulate tissue resection involves decoupling the tumor nodes in the mesh to reproduce the effect of cavity collapse. However qualitative results such as those presented in Table 4 and Figure 14 indicate the need for a better strategy. In our future work, we plan to explore other strategies to better account for resection forces.

Another interesting difference between the postoperative data and the intraoperative data is the contributions from various mechanisms in the atlas. The concatenated atlas in the work of Dumpuri et. al. was formed from three different atlases: (i) tumor being resected and gravity alone causing the shift, (ii) tumor being resected and mannitol alone causing the shift, and (iii) tumor being present and having a swelling effect and the rest of the brain parenchyma under the effect of mannitol. The contribution of these atlases to the overall solution was 45%, 46% and 9% respectively, with similar

distributions being observed across all patients. For the intraoperative data reconstructions presented here, the averaged distributions of the weighting coefficients between the gravity and mannitol solutions across all solutions are 16% and 84% respectively. Figure 17 is an example from 3 patients.

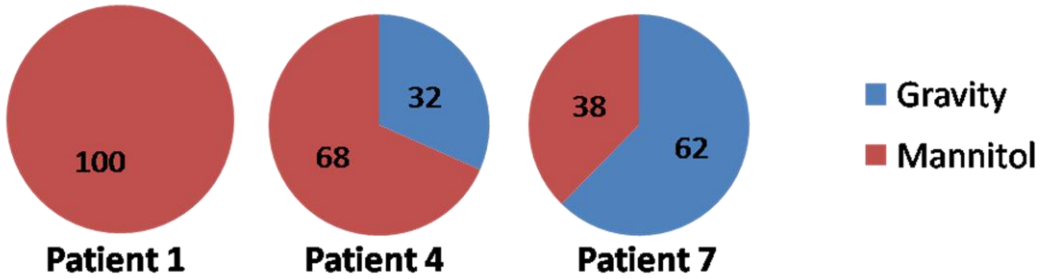

Figure 17. Distribution of weighting coefficients for the gravity and mannitol solutions for patients 1, 4, and 7 obtained by optimizing the least squared error in intraoperative data.

For four of the seven cases, the mannitol solutions exclusively contributed to the reconstructed solution. For two cases mannitol solutions were the major contributors and for the last case, gravity was the major contributor. Intraoperatively, while more variability is illustrated, the reconstructed solutions weigh the mannitol solutions more in six of the seven cases than the analysis in [3]. In addition, the magnitude of the regression coefficients was comparatively smaller in the gravity atlas. In the OR environment, various forces — gravity, mannitol, edema, tissue resection- act concurrently on the brain and it is difficult to sequester the contribution of each of these forces individually. In some respect, the results presented here agree with intuition. Given that mannitol is administered just prior to opening the dura in significant dosages to decompress the brain, shortly thereafter, tissue manipulation occurs to visualize the tumor, and generation of a resection hole and possible collapsing of surrounding tissue then follows, it is not surprising that mannitol plays a more considerable role in the regression coefficients, and

that the variability in these coefficients across patients is much more distributed. The Dumpuri et. al. study also reported a contribution from mannitol but not to the degree this study does. In this study, the magnitude of deformations intraoperatively could just not be matched by a model experiencing CSF drainage only. This could be due to the manner in which it is modeled but the results of a more pronounced reliance on mannitol-based regression coefficients for the intraopertive environment is consistent with surgical practice and would seem to speak to its influence in the reconstruction.

Conclusions

A retrospective study of correcting brain shift using sparse intraoperative LRS data to drive a finite element model based atlas was presented in this work. The method corrects for an average of 75% of the brain shift caused by various factors in the OR. While intraoperative MR imaging was not available, the results were consistent with a pre- and post-MR validation study conducted previously. When comparisons to a previous study were made, it was found that the intraoperative data contained far more dynamic interactions such as collapse due to tissue resection and considerably larger deformation. It was found that guiding shift compensation with surface data only requires a model that incorporates neuroanatomical subsurface structures such as the dural septa. Lastly, to our knowledge, the apparent need for the modeling of hyperosmotic drugs to account for intraoperative shift is a unique finding by our team. These results were found within the pre- and post-MR analysis by Dumpuri et al. and are further confirmed here for the intraoperative environment.

Acknowledgements

The authors would like to thank the resident surgeons, the operating room staff and the radiology department at Vanderbilt University for their help in data collection. Most of the visualization algorithms were developed using Visualization Toolkit (http://www.vtk.org). Some segmentation and calculations were performed using Analyze AVW Version 9.0.

Appendix A

The material properties in equations (1)-(2) are listed below.

TABLE 5
MATERIAL PROPERTIES

Symbol	Value	Units
E_{white}, E_{gray}	2100	N/m^2
E_{tumor}	100,000	N/m^2
ν	0.45	no units
ρ_t	1000	kg/m^3
ρ_t	1000	kg/m^3
g	9.81	m/s^2
α	1.0	no units
$1/S$	0.0	no units
k_{white}	1×10^{-10}	m^3s/kg
k_{gray}	5×10^{-12}	m^3s/kg
$k_{c1,\ white}$*	2.3×10^{-9}	Pa/s
$k_{c2,\ white}$*	4.6×10^{-9}	Pa/s
$k_{c3,\ white}$*	6.9×10^{-9}	Pa/s
$k_{c1,\ gray}$*	11.5×10^{-9}	Pa/s
$k_{c2,\ gray}$*	23.0×10^{-9}	Pa/s
$k_{c3,\ gray}$*	34.5×10^{-9}	Pa/s
p_c	-3633	Pa

* These values were used to simulate three different capillary permeability values resulting from the administration of mannitol and are designed to capture a physiological range.

CHAPTER V

MANUSCRIPT 2 — Sensitivity analysis and automation for intraoperative implementation of the atlas-based method for brain shift correction.

Manuscript in preparation: I. Chen, A. L. Simpson, K. Sun, B. M. Dawant, R. C. Thompson, and M. I. Miga, *Int J Comput Assist Radiol Surg*

Introduction and Significance of Study

In this work, techniques that could potentially reduce the pre-operative computational time for creating a patient specific mesh and building the deformation atlas are studied. Previous work in Chapter III described a completely manual method for segmenting the brain and tumor tissue and a semi-automatic method for the dural septa [73]. In this work, an automated segmentation technique is described for segmenting the brain and the dural septa, structures that are used to create the finite element mesh. The automatic segmentation and shift correction were compared to those using manual segmentation and the effect on shift correction is presented. The constituency of the deformation atlas was previously determined by empirical testing. Variables in building the deformation atlas include head orientation, CSF drainage levels, and capillary permeability values. While an ideal atlas would consist of an infinite number of solutions, finely sampling every possibility, for computational feasibility a balance must be struck in terms of how finely the space must be sampled. For instance, in previous work in

Chapter III, 60 head orientations were selected by sweeping a 20° cone around an estimated base orientation, with the computational time ranging from 10–18 hours. If similar results could be obtained by sampling the space more coarsely, the number of solutions and hence the computational time would be reduced. In this work, the effect of atlas size and resolution is evaluated systematically by a sensitivity analysis using simulation experiments and clinical data.

Abstract

Purpose: The use of biomechanical models to correct the misregistration due to deformation in image guided neurosurgical systems has been a growing area of investigation. In previous work, an atlas-based inverse model was developed to account for soft-tissue deformations during image-guided surgery. Central to that methodology is a considerable amount of pre-computation and planning. The goal of this work is to evaluate techniques that could potentially reduce that burden.

Methods: Distinct from previous manual techniques, an automated segmentation technique is described for the cerebrum and dural septa. The shift correction results using this automated segmentation method were compared to those using the manual methods. In addition, the extent and distribution of the surgical parameters associated with the deformation atlas were investigated by a sensitivity analysis using simulation experiments and clinical data.

Results: The shift correction results did not change significantly using the automated method (correction of 73±13%) as compared to the semi-automated method from previous work (correction of 76±13%). The results of the sensitivity analysis show that

the atlas could be constructed by coarser sampling (six fold reduction) without substantial degradation in the shift reconstruction, a decrease in preoperative computational time from 13.1±3.5 hours to 2.2±0.6 hours.

Conclusions: The automated segmentation technique and the findings of the sensitivity study have significant impact on the reduction of pre-operative computational time, improving the utility of the atlas-based method. The work in this paper suggests that the atlas-based technique can become a 'time of surgery' setup procedure rather than a pre-operative computing strategy.

Introduction

It is now recognized that intraoperative neurosurgical guidance systems can be compromised by non-rigid brain deformations caused by gravitational forces, administration of hyperosmotic drugs like mannitol, swelling, resection and retraction forces [5, 7]. This is the *brain shift* problem. The misregistration between physical and image space that is associated with this problem usually ranges from 1 to 2.5 cm [5, 7, 73]. Various techniques to correct for this misregistration span from acquisition of volumetric intraoperative images like computed tomography (CT) [12], magnetic resonance imaging (MRI) [5], ultrasound [26-28], and predictive biomechanical modeling [2, 32-34, 54]. While several medical centers have adopted the direct usage of intraoperative imaging units for guidance, there is still a need to register the wealth of preoperative data that cannot be obtained during surgery (e.g. diffusion tensor MR or functional MR). Methods to achieve this during the procedure have been forthcoming and represent data-rich frameworks [30, 32, 34]. However, concerns like exposure to ionizing

radiation for CT and prohibitively high expense for MRI have led others to pursue more cost efficient methods using sparse intraoperative imaging devices like stereoscopic operating microscopes [36], laser range scanner devices [37, 40], and ultrasound imaging [26-28]. These devices provide information at the exposed craniotomy surface, some subsurface information in the case of ultrasound, and are often coupled with computer models (either biomechanical or interpolative) to provide deformation information in the rest of the domain [2, 3, 27, 73].

The physical properties that govern the brain tissue deformation have been described using different constitutive laws – linear elastic [32, 34], non-linear viscoelastic [33], and biphasic [54]. While the complex non-linear model may describe the physical interaction of tissue more accurately, the complexity may come at the cost of computational time, which may be a hindrance in its implementation in real time. In addition, from the systems level perspective, often the error between linear and nonlinear models is small compared to the errors associated with tracking and segmentation. Nevertheless, regardless of the choice of model, with sparse intraopertive data, there is considerable uncertainty in the determination of factors that cause deformation to exact precision in the OR. These factors can be the head orientation, level of cerebrospinal fluid (CSF) drainage, and the alteration of capillary permeability resulting from administration of mannitol. To circumvent these problems, Dumpuri et. al. proposed an atlas-based approach where the forward model for deformation was solved for different permutations of driving conditions [2]. Minimization of the least squared error between the model predictions and the sparse intraoperative measurements provided the final solution. In this particular work, the biphasic model based on Biot's consolidation theory [53] was used to

describe the physical behavior of brain tissue. Discretized and solved with the Galerkin weighted residual method in finite element analysis, this model was ideally suited for the atlas-based approach because of computational simplicity while taking into account the role of interstitial pressure driving fluid movement in brain tissue.

The atlas-based method was validated with pre- and post-operative MR data. The atlas-based model provided an average of 85% surface and subsurface shift correction [3]. The method was also evaluated with intraoperative data in [73] and the shift correction was found to be an average of 75%. The reason for the degradation of correction in intraoperative data was the larger magnitude of shift correction and the more dynamic interactions like resection forces in the OR, as compared to the post-operative MR, where the time elapsed after the surgery allowed for shift recovery. There was also a suggestion in [73] that mannitol played a more considerable role in the magnitude of deformation whereas it would not have been as pronounced in the Dumpuri et al. study [3]. The work presented in [3] and [73] was a retrospective analysis and important issues of intraoperative implementation were not addressed in that work. For instance, both the works described segmenting the brain and building a patient specific mesh from the MRI scans acquired for every patient. In addition, the work in [73] suggested the need to model the dural septa, membranous structures like the falx cerebri and the tentorium cerebella, that limit the movement of brain in the contra-lateral hemisphere and the cerebellar region of the brain. The method of segmentation of the brain and the dural septa was a manual and tedious process. While the mesh creation and the atlas building computations are done pre-operatively, the time window between image acquisition and surgery can be a few hours. For the method to be feasible for

clinical implementation, automating the processes to reduce computation time may be critical. This paper will look at an automatic segmentation method for the cerebral tissue and the dural septa and compare the results to the manual segmentation.

The atlas of deformations in [3] was formed with gravity, mannitol, and swelling driving conditions and consisted of 501 solutions. The results in that paper showed a very minor role of swelling in the reconstructed solutions, and the analysis in [73] only consisted of gravity and mannitol solutions, with and without tumor resection — a total of 720 solutions. While shift reconstruction in the OR using the atlas takes under a minute, the pre-operative time required to build the atlas on a parallel cluster ranges from 10 to 18 hours, depending on the number of solutions. The size of the atlases in the above two papers was not extensively analyzed. One aspect to this paper will be to investigate the level of detail used in the atlas-based method within the context of shift prediction and determine what resolution of atlas is necessary. Building atlases with fewer solutions could have a significant impact on the computation time to construct the atlas. In this paper, results of systematic sensitivity studies towards the automation of our segmentation approaches and the effects of atlas resolution will be investigated with respect to the prediction accuracy of our approach.

Methods

A semi-automated pipeline that consists of manual image segmentation, semi-automated dural septa segmentation, mesh generation, atlas building using forward model runs of the linear elastic biphasic model, and inverse solution using optimized linear least squared error between atlas predictions and sparse measurements was presented in [73].

The first four steps are performed pre-operatively after the patient MRI images are acquired. The inverse model is solved intraoperatively after acquisition of sparse serial LRS scans before and after tumor resection. The schematic of the process is shown in Figure 18 below.

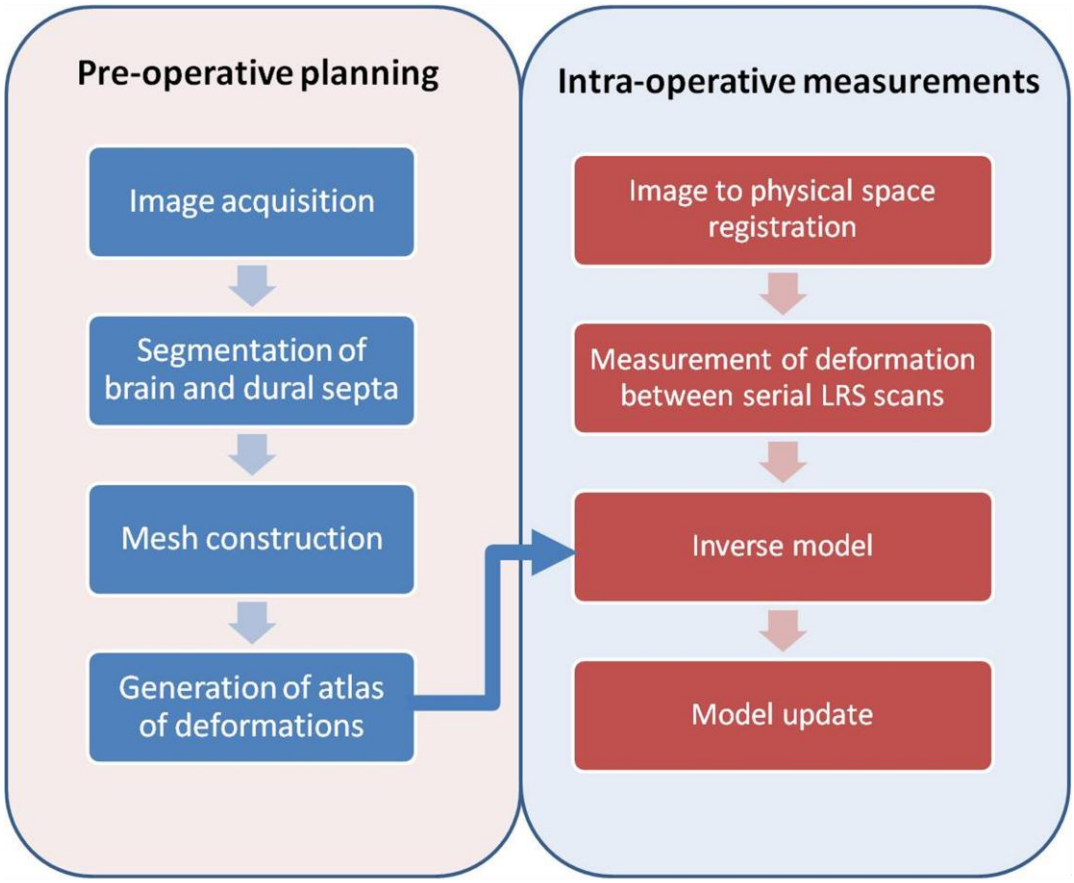

Figure 18. Schematic of the pipeline for model updated image guidance system. The pre-operative computations are typically performed the day before surgery and take on the order of several hours of computation. The intraoperative computations are performed during the surgery and provide updated information in real time.

The biphasic consolidation model [53] was used to describe the deformation behavior of the tissue. The details about the model, boundary conditions, and material properties are shown in Appendix B. The inverse model is solved intraoperatively by an optimized least squared minimization between the model predicted displacements and displacements

measured through homologous point selection in sparse intraoperative data [73]. The process of mesh construction and atlas generation is automated, but in [73], the segmentation steps were performed manually. The typical MRI image volume acquired had 180 slices in that study and the manual segmentation process was tedious and could take a few hours. In the following sections an automated segmentation process will be described and a comparison between the results of automatic and manual segmentation will be presented.

Data

The data consists of five image sets acquired pre-operatively for patients undergoing brain tumor removal surgery shown in Table 6 below.

TABLE 6: Patient information about cases used in the study. Tumor locations L: left or R: right signify the hemisphere, followed by the lobe- F: frontal, P: parietal or T: temporal.

#	Location	Age, gender	Lesion size (cm)	Average measured shift (mm)	# selected points
1	L,F	22F	5.2 x 6.2 x 6.0	23.6	16
2	L,F	52M	4.9 x 5.6 x 5.0	15.1	22
3	L,P	58M	3.7 x 3.5 x 4.1	8.5	24
4	L,T	77M	3.4 x 3.6 x 2.0	9.2	18
5	L,T	75F	5.0 x 5.0 x 5.0	13.0	22

The scans were acquired using 1.5-T clinical scanner. The voxel size for all patients was 1 mm × 1 mm × 1.2 mm and each scan consisted of 180 to 190 slices.

Automated Segmentation

The automated segmentation algorithm is based on the atlas-based segmentation approach described in [56]. The segmentation was performed using a series of three steps during which the patient images acquired above are registered to a template T1 image of

size 256 × 256 × 256 and 1 mm × 1 mm × 1 mm voxel size, for which an expertly segmented binary mask was available. The steps of the segmentation are described in the schematic below.

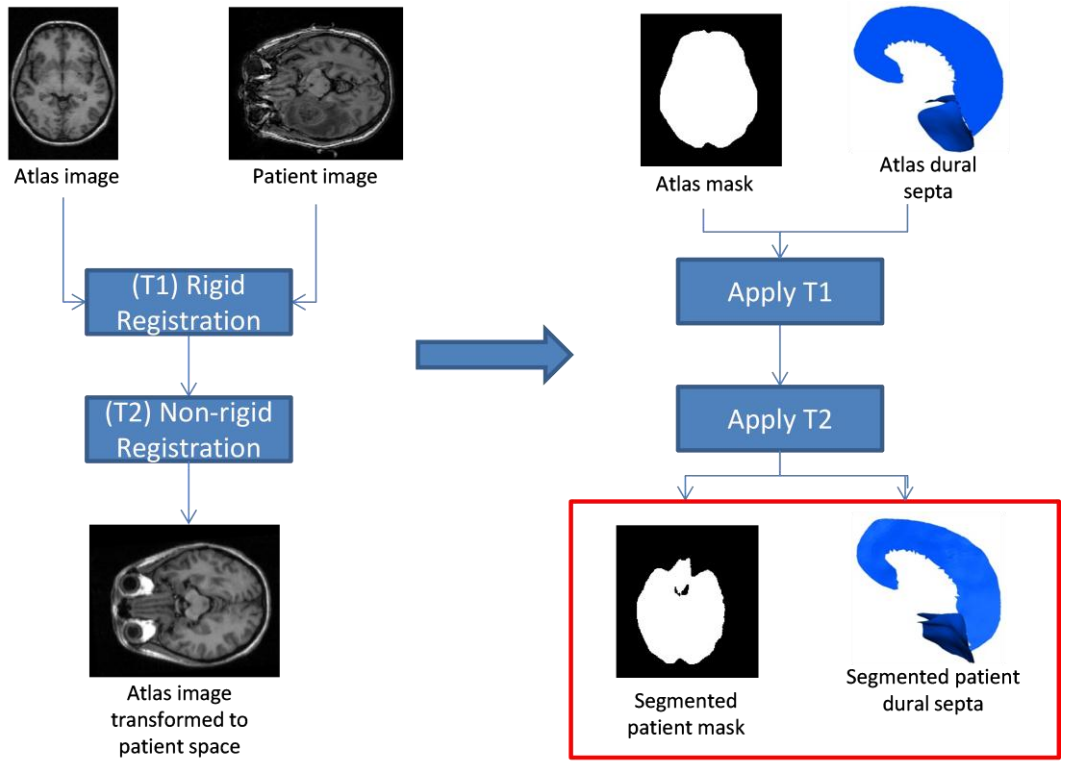

Figure 19. The schematic for segmentation of cerebral tissue and dural septa. A rigid transformation between an atlas image and patient image (T1) is computed. The transformation, T1 is applied to the atlas image and a non-rigid transformation (T2) is computed between the rigidly transformed atlas image and the patient image. The computed transformations (T1 and T2) are applied to structures derived from the atlas image (binary mask and dural septa templates) to obtain the segmentation of patient cerebral tissue and dural septa.

The first step consisted of a rigid registration (T1) between the patient image and the template atlas image based on the mutual information metric [74]. The second step consisted of a non-rigid registration (T2) between the patient image and the transformed template image from first step using the adaptive basis algorithm driven with the mutual information metric [75]. In the third step, the transformations obtained from the registrations (T1 and T2) are applied to the template mask to obtain a segmentation mask

for the patient image. A set of template dural membrane structures were also created for the template image using the semi-automated method described in [73]. The registration transformations (T1 and T2) are also applied automatically to the dural septa structures — the falx cerebri and the tentorium cerebelli. The remainder of the tetrahedral mesh construction proceeds with the automated algorithm using [59, 70] as described in [73]. In addition to the automated segmentation described above, manually created expert segmentations were also performed for the structures. The closest point distances between the dural septa created by automated segmentation were compared to the manually segmented septa. The falx and the left and right tentorium were examined separately. In addition the falx was divided into three equally spaced regions — anterior, middle, and posterior region — and the closest point distances of these three regions were separately analyzed. Lastly, the difference between brain shift compensation results using the domains generated from these two different methods was compared.

Sensitivity Analysis

The last step in the pre-operative pipeline in Figure 18 for atlas building involves constructing the boundary conditions based on the surgical plan and solving the model in a forward manner for each of those conditions, as described in greater detail in Appendix B. This process, though automated, may be the most time consuming computational step depending on the number of conditions for which the model is solved. For instance, in the work in [73], two different forces were modeled: gravitational force and force resulting from pressure gradients caused by hyperosmolar drugs like mannitol. For gravity, 60 head orientations were solved using 3 CSF drainage levels, each model solved with and

without tumor resection – resulting in 360 solutions. Mannitol conditions were solved similarly with an atlas consisting of 360 solutions, resulting in a combined atlas of 720 solutions. The time for a single forward model solve varies depending on the uniformity of element size, the number of elements in the mesh, and hardware utilized. Our software has been built for parallel computations using the open-source software resources PETSc [76] and MPI [77] and all the computations in [73] were performed with a parallel cluster of 12 quad-core 2400 MHz Dual-Core AMD Opteron(tm) Processors. The computations were distributed across four of these nodes and building time for an atlas with 720 solutions ranged from 10 to 18 hours. The following sub-sections will describe sensitivity studies using simulations and clinical data in Table 6 to evaluate the effect of atlas size on accuracy of the inverse model.

Simulation experiments

The goal of the simulation studies was to evaluate the size and composition of the deformation atlas. Since the largest contribution to the atlas size came from the number of head orientations, this will be the main parameter studied in the simulation experiments.

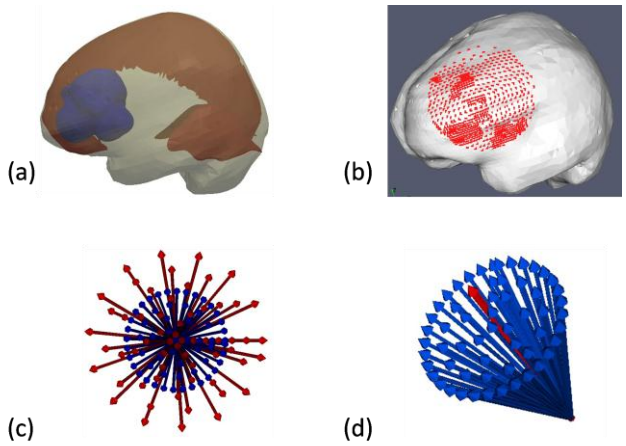

Figure 20: (a) Mesh used for the simulation experiments with the dural septa (brown) and the tumor (blue) overlaid, (b) The displacement solutions of the forward runs at the craniotomy nodes (red) used to simulate sparse data, (c) Spatial extent experiment. Blue shows the head orientations in that atlas. Red arrows show the head orientation of the ground truth solutions. (d) Spatial resolution experiment. Blue shows the head orientations in the atlas. Each orientation was eliminated from the atlas and used as the ground truth solution sequentially.

For the simulation experiments, an FEM mesh from case #2 in the clinical cases listed in Table 6 was used (Figure 20 (a)). Forward model runs with varying head orientations and other forcing conditions are used as ground truth. Sparse data was simulated by selecting the displacement solutions for the nodes in the craniotomy region, close to the tumor (Figure 20 (b)). In the first experiment, the effect of spatial extent was studied. In Figure 20 (c), the blue arrows (corresponds to the direction of the gravity vector) show the head orientation of each solution in the atlas, the extent of the cone is 20º. The red arrows show the head orientations corresponding to the ground truth (i.e. ground truth is the simulated results we would like to reconstruct from the atlas of solutions), consist of concentric cones ranging from 2.5º to 32.5º to the center, in the increments of 5º. The ground truth head orientations that are less than 20º from the center of cone are contained in the computed atlas. For solutions where the ground truth orientation was greater than 20º, the estimate of head orientation would be mis-predicted and would lie outside the cone. In the second simulation experiment, the effect of spatial resolution was tested to

study the effect of the size of the atlas on shift error (Figure 20(d)). Each of the head orientations was systematically eliminated from the atlas and used as ground truth. This was repeated for six different atlases with different atlas solution sets of varying sparsity as shown in Figure 21 with the six atlases designating the number of contained solutions as 5, 14, 21, 30, 43, and 59, respectively.

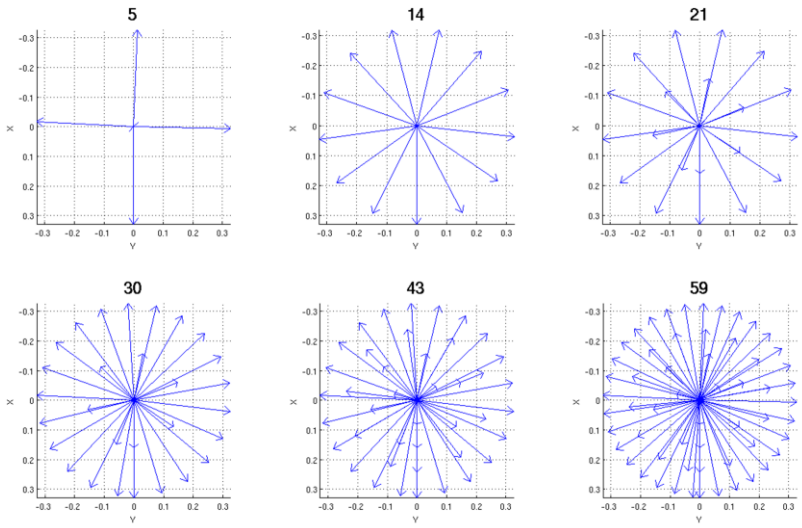

Figure 21. Head orientations. The number listed on top is the number of head orientations in each atlas. The different sized atlases were used to evaluate the effect of spatial resolution on the inverse model.

The correction results for every solution in the atlases was evaluated by running the inverse model and looking at the shift correction. In addition, the 'ground truth' selection was never contained explicitly within an atlas being used for correction.

Clinical data

The sensitivity of shift correction to number of head orientations, CSF drainage levels, and mannitol related capillary permeability values was also evaluated using the pre-operative MRI and intraoperative laser range scanner data collected for the five clinical cases listed in Table 6. To evaluate the effect of head orientations on clinical data, the different head orientations shown in Figure 22 were used to build the atlas.

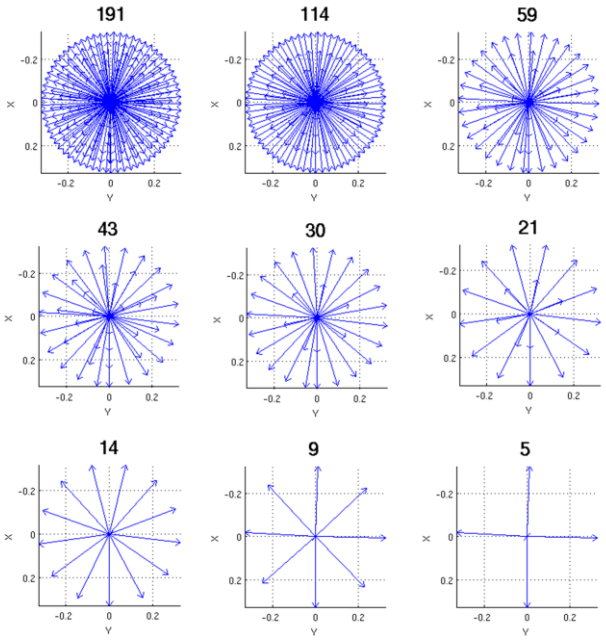

Figure 22: Head orientations. The number listed on top is the number of head orientations in each atlas. The different sized atlases were used to evaluate the effect of spatial resolution on the inverse model for the clinical data listed in Table 6.

The atlas was also built using different fluid levels for gravity and different capillary permeability values for mannitol. The inverse model was tested with different numbers of fluid levels and capillary permeability values. Three fluid levels/capillary permeability was the maximum resolution used (Figure 31, Appendix B). In addition two (highest and lowest values) and one (only the highest value) fluid levels/capillary permeability were also tested.

Results

Automated Segmentation

Five cases in Table 6 were segmented using the automated algorithm as well as the manually. The results for automated segmentation of brain were assessed qualitatively

as well as quantitatively. The occurrence of error for the segmentation of brain tissue was based on the visual evaluation of the quality of overlay between the segmentation mask and the cerebral tissue in the patient MRI. Slices that contained a visually significant misoverlap between the mask and the image were designated to contain error. The specific slices containing the segmentation errors were manually edited and the results were used for mesh construction and building the atlas. The following figure shows selected slices from a completely manual segmentation, automated segmentation and after editing the results of the automated segmentation for two cases.

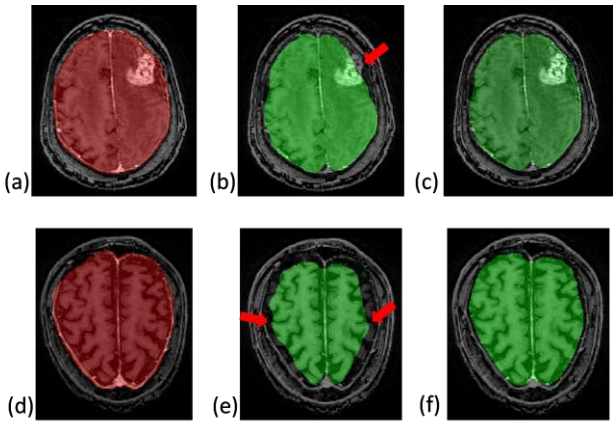

Figure 23. The top rows shows the segmentation results for patient #2 and the bottom row shows the segmentation results for patient #4. (a) and (d) show the results of manual segmentation. (b) and (e) show the results of automated segmentation with red arrows indicating the regions of misclassification of brain tissue. (c) and (f) show the slices in (b) and (e) after manually editing to correct the misclassified regions.

The regions containing error, determined by qualitative evaluation of the overlay between the mask and the image, are designated with red arrows in Figure 23 (b) and (e) for two cases. Table 7 below lists the total number of slices in each dataset and the number of slices for each case that contained segmentation error.

TABLE 7: Image size for each dataset and the number of slices in each dataset that got misclassified using the automated segmentation method.

Case #	Total slices	# slices with segmentation errors
1	180	41
2	190	47
3	180	0
4	180	31
5	180	13

Among the five datasets, for the automated segmentation of the cerebrum tissue, four of the cases had several slices containing some misclassified tissue and patient #3 was the only case that contained no segmentation error.

The results of the automated segmentation of the falx and tentorium were evaluated quantitatively as well as qualitatively. Through visual assessment of the dural septa, the automated segmentation algorithm provided acceptable results for modeling purpose. The segmentation results for the dural septa are shown in the figures below and discussed in greater detail.

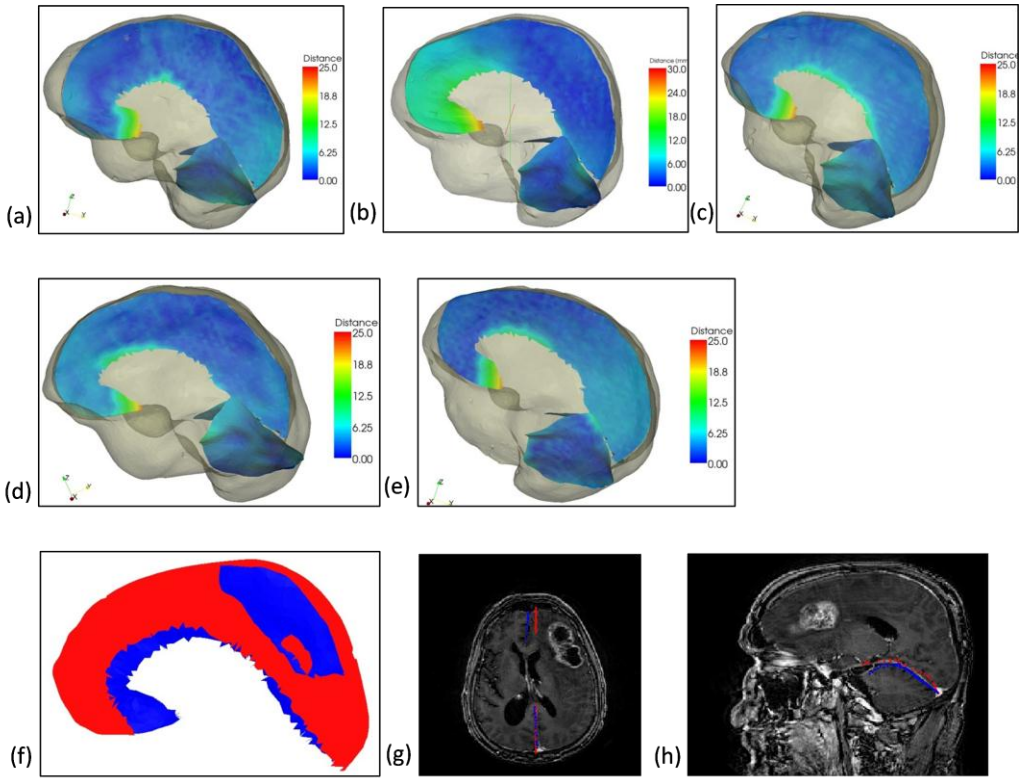

Figure 24. Shows the mesh along with the falx and tentorium segmented using the automated segmentation method. The falx and tentorium are color coded with the closest point distance between the automated and manually segmented dural septa (a) – (e) for patient 1 – 5 respectively. (f) shows the dural septa created by automated segmentation (blue) and manual segmentation (red), (g) shows the automated (blue) and manually segmented (red) falx overlaid on the MRI image and (h) shows the automated (blue) and manually segmented (red) tentorium overlaid on the MRI image for patient #2.

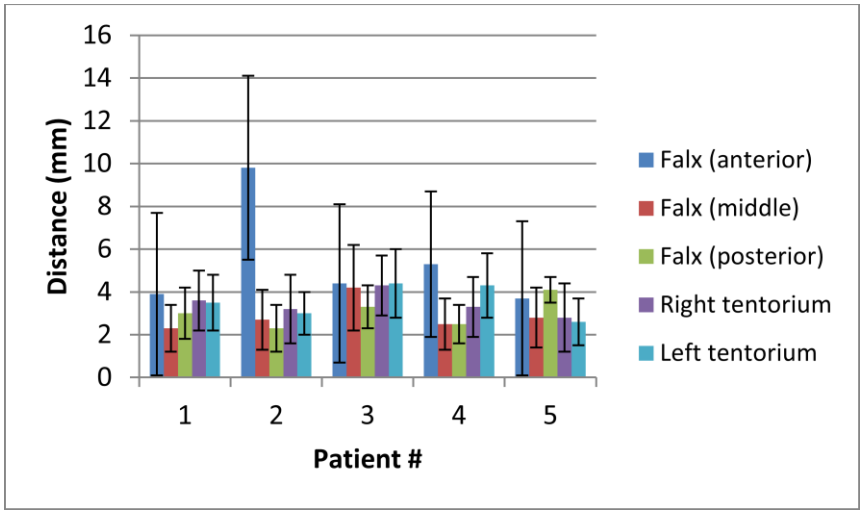

Figure 25. Shows the average closest point distances between the automatically and manually segmented dural septa for the five patient cases. The distances for anterior, middle, and posterior part of the falx, and right and left tentorium are presented separately.

Figures 24 (a) – (e) show the surface of the finite element mesh and the dural septa – the falx and tentorium, created using the automated segmentation algorithm. The dural septa are color coded with the closest point distance between the septa segmented using the automated algorithm and the manual method. Figure 25 shows the average distance between the automatically and manually segmented dural septa. The distances for the falx, right, and left tentorium are presented separately. In addition, the falx is further subdivided into three equally spaced regions—anterior, middle and posterior. The overall average distance between the automatically and manually segmented dural septa is 3.7±1.8 mm. The largest difference in terms of distances is in the anterior region of the falx. This is especially pronounced in patient #2, and to some extent in patient #1 and patient #4. The automatically (blue) and manually (red) segmented falx for patient #2 are shown in Figure 24 (f). The overlay of the falx and the tentorium on the MRI images are also shown for the same patient in Figure 24 (g) and Figure 24 (h) respectively. The blue lines are the results of the automated segmentation and the red contour is the results of manual segmentation. The overlay images also show least overlap between the two segmentation methods in the anterior region of the falx. The automated segmentation method actually performs better by visual evaluation of the overlay between the hyperintense region and falx contour. The tumor pushes the falx away from the centerline through mass effect and the manual segmentation of the falx was performed by drawing on the contour of the falx in the central sagittal plane and hence does not capture the deviation from the plane well, which is captured by the automated method.

The figure below shows the percent shift correction after running the inverse model using the manual segmentation method and the automated segmentation method.

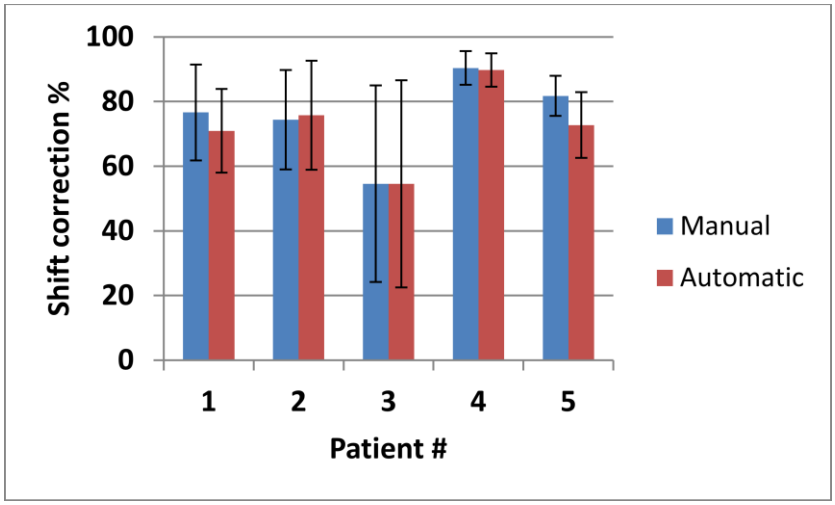

Figure 26: The percent shift correction between the measurements and the model predicted deformation for the five cases listed in Table 6 using the manual and automated segmentation methods.

The average shift correction for the five cases using the manual segmentation method is 76±13% and automated segmentation method is 73±13%. The mean correction was slightly lower for the automated segmentation method however a paired student t-test indicates that there is no statistical difference ($p>0.05$) for the shift correction results using the two methods.

Sensitivity Analysis

Simulation Experiments

The shift correction error for the simulation experiment for studying spatial extent, where the ground truth varied from 2.5º from center of the predicted cone of head orientations and up to 32.5º angle from the center is shown in the Figure 27 below. The results for error between the location of model-predicted and ground truth points was averaged for each head orientation that was at the same angle from the center of the cone.

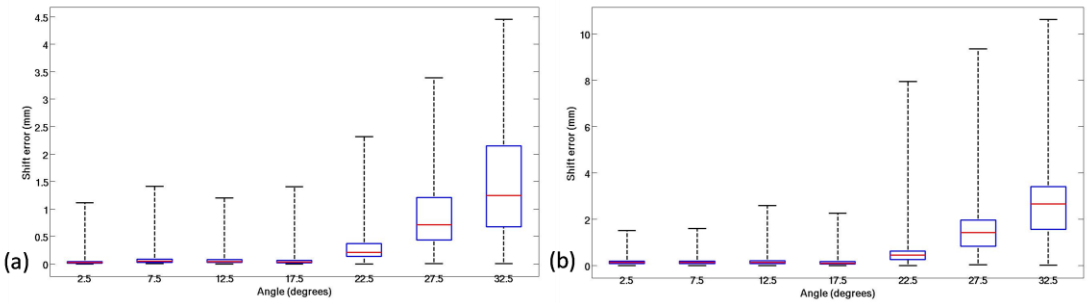

Figure 27. Box and whisker plot for error between model prediction and measurements for the simulation experiment. The x-axis represents the angle from the center of cone of atlas of head orientations and head orientation used to generate the ground truth. The red line represents the median, the box represents the twenty fifth and seventy fifth percentiles and the whiskers represent the extent of data. (a) shows the errors for ground truth without resection and (b) shows the ground truth with resection.

Figure 27 (a) shows the results using the ground truth solutions without resection and Figure 27 (b) shows the error where the ground truth results were produced by simulating resection. In both the cases, the error is minimal when the actual head orientation is contained within the cone of head orientations used to construct the deformation atlas. The error increases as the actual head orientation of the ground truth lies outside the sampling space of the head orientation angle. It is also a noteworthy point that the overall magnitude of error is larger for the case where ground truth simulates tissue resection.

The following figure shows the results for the simulation experiment to study atlas resolution. The mean error and the standard deviation for each of the different sized atlases (Figure 21) are shown in the figure below.

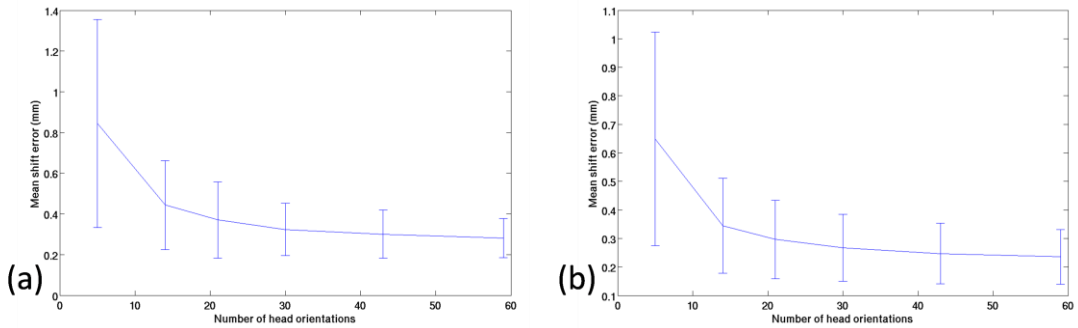

Figure 28. The mean and standard deviation of shift error for atlas of different resolution for (a) surface points and (b) subsurface points.

Figure 28 shows that though the error is modestly larger for the atlas with the coarser resolution and then quickly becomes asymptotic for both surface and subsurface nodes.

Clinical data

The following figure shows the error between model prediction and measurements for the five clinical cases listed in Table 6 using atlases built with different number of head orientations (Figure 22).

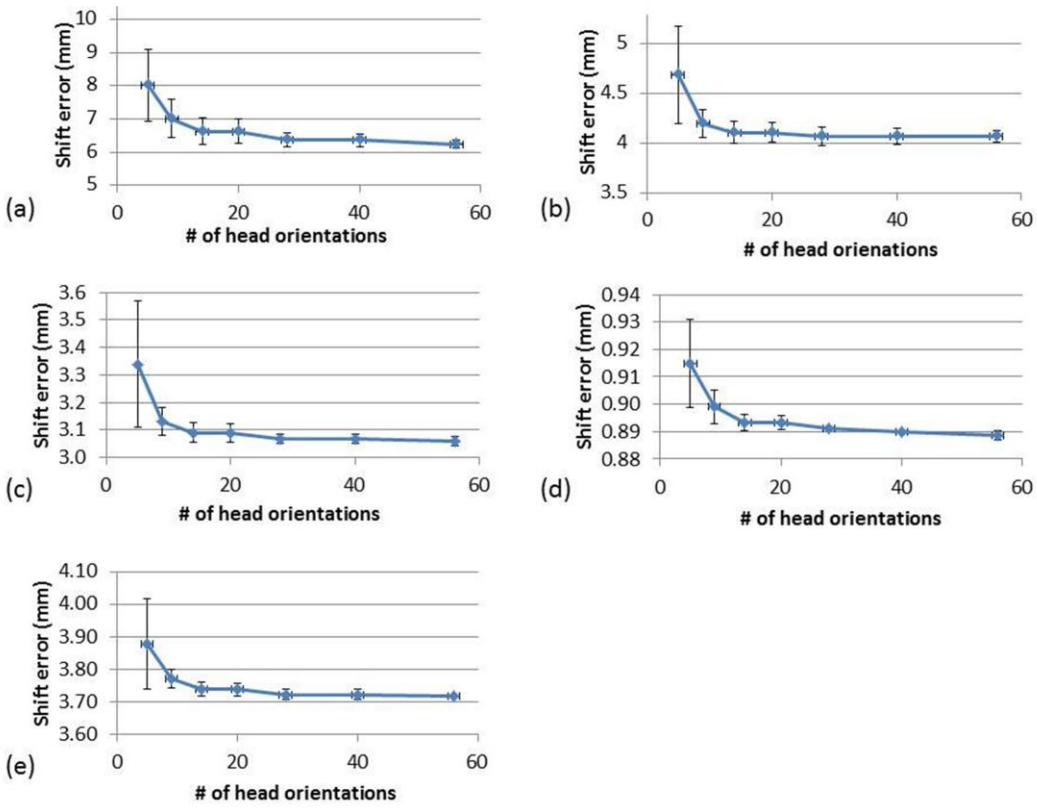

Figure 29. Shift error in mm, plotted for the five different cases, (a–e) correspond to patient #1–5. The error was calculated using atlas constructed with different number of head orientations, as shown in Figure 21.

The clinical data in Figure 29 follows a similar trend as the simulation experiment results in Figure 28, being larger at the coarser resolution and becoming asymptotic at larger resolutions with an accompanying decrease in variance. Although the above figure shows a maximum atlas size of 59 head orientations, larger sizes (shown in Figure 22) were also tested and showed no change. Testing for the effect of altering the number of fluid levels and capillary permeability values showed no change in shift correction results for the clinical cases.

Discussion

The non-rigid deformation of the brain tissue caused by gravitational forces, hyperosmotic drugs, resection and retraction forces can result in a significant error, affecting the fidelity of the image guidance system in neurosurgery. The past literature has described combining the use of sparse intraoperative devices with computational models. Our group proposed the atlas-based paradigm to overcome the uncertainty of determination of various parameters in the intraoperative environment and we validated this method with retrospective studies using postoperative and intraoperative data [3, 73]. As we move towards the implementation of this method in real-time in the OR, the computational time and efficiency become important factors. This work examines the pre-operative pipeline that consists of constructing the patient specific finite element mesh and building the deformation atlas. More specifically, an automatic segmentation method for the cerebrum and the dural septa was evaluated and the results of sensitivity analysis to determine the constitution of the deformation atlas were presented.

The automatic segmentation method for the cerebral tissue in the MR images was tested on five patient images and four of these datasets contained some error determined by visual examination. Since the segmentation method was based on the intensity based registration and the template image was a normal brain, anomalies in the images resulted in segmentation error. The results for hyperintensity on the surface due to large tumors and cerebral atrophy caused localized segmentation errors as demonstrated in Figure 23. Patient 2 had a tumor near the surface in the frontal lobe and the automated segmentation algorithm is confounded in the vicinity of that region. Patient #4 was a 77 year old male and the MRI of the brain shows age related cerebral atrophy. Consequently the automated

algorithm did not perform well near the contours. Patient #3 was the only case where no substantial segmentation error was observed because in this case the bulk of tumor was beneath the surface. The other four cases, a handful of slices (ranging from 13 to 47 for the five cases) required manual editing as opposed to a completely manual segmentation method. For a completely manual segmentation of the image with 180 slices, takes an average of 2 to 3 hours. The automatic segmentation algorithm took about 15 minutes on a 3.2GHz, Intel I7 processor. Depending on the slices needing manual editing, the total time for segmentation, including the automated algorithm and manual editing, takes 30 minutes to an hour.

The results for the automatic segmentation of the dural septa are dependent on the results from the previous segmentation of cerebrum – it uses the transformations obtained from the rigid and non-rigid registration between the template image and the dataset. The algorithm produced segmentation results for falx and tentorium that were satisfactory for modeling purposes for all five cases. As seen in Figure 26, the automated segmentation technique did not significantly change the shift correction. However it is worth noting that for patients #1 and #5 the decline in shift correction by using the automatic segmentation method was 6% and 9% respectively indicating the effect segmentation results can exert on overall shift prediction accuracy. The results of falx segmentation are visually more accurate using the automatic segmentation method because the manual method in [73] assumed it to be a planar structure, which is invalid when the mass effect from the tumor pushes the structure away from the plane. The largest benefit of the automatic segmentation for both the cerebrum and the dural septa is the reduction in time. As discussed before, the complete manual segmentation of the cerebral tissue takes 2 - 3

hours. The semi-automatic segmentation of the dural septa takes an additional 15 - 30 minutes. Even with manually correcting the segmentation errors for a few slices, the computational time ranges from 30 minutes to an hour, giving a time savings of 1.5 to 3 hours.

The number of head orientations is the variable that contributes the maximum number of solutions to the size of the atlas. Using simulation experiments, spatial extent was found to be a more important factor in the shift correction accuracy than the resolution. Considerably larger errors were found when the true orientation was outside the prediction sample space as shown in Figure 27. Sampling the space more finely does not significantly improve the shift correction as seen in both the simulation study (Figure 28) and the clinical data (Figure 29). At the minimal number of head orientations, the error is slightly higher, but the correction error is asymptotic at 20–30 solutions. When examining the weighting coefficients from the optimized results across different sized atlases, the number of non-zero coefficients ranged from 1–6. This was consistent with the variation of information within the atlas. A principal component analysis of the atlas of sparse measurement nodes revealed that 3–6 eigenvalues explained 99% of the power of the atlas, pointing towards the redundancy of information in very closely sampled solutions. This explains the observation that similar precision can be achieved with a coarser resolution of the atlas. Using different number of fluid levels and permeability values resulted in no change in shift correction results. This could be explained based on the constrained optimization method used to reconstruct the inverse model results. As shown in Appendix B.4, the optimization method minimizes the least squared error between the measurements and predictions with the non-negativity constraint and the

summation of all weighting coefficients being less than or equal to one. The fluid levels and capillary permeability values control the magnitude of shift, and if the magnitude of measurement is smaller than the predictions, then the weighting coefficients interpolate it with the appropriate scaling.

The following figure compares the computation time for building the atlas using 60 head orientations and three fluid levels/capillary permeability values as done in [73] and 30 head orientations and one fluid level/capillary permeability value.

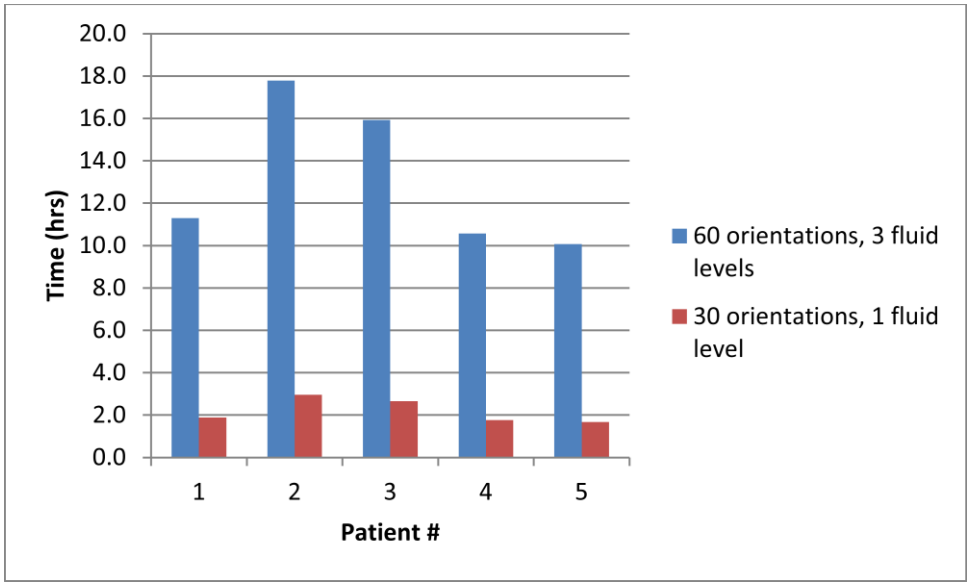

Figure 30. Computational time to build the pre-operative deformation atlas. The times are shown for 60 head orientations and 3 fluid levels as in [3]. This is compared to the computational time for a smaller atlas with 30 head orientations and 1 fluid level.

The average time with 60 orientations and three fluid levels/capillary permeability values is 13.1±3.5 hours, whereas the average computational time for building the atlas with 30 head orientations with one fluid level/capillary permeability value is 2.2±0.6 hours. The change in shift error by reconstructing the results from these two atlases is minimal but the savings in time cost is significant.

Conclusions

In the study described above, a limited number of cases were used. While the automatic segmentation method only resulted in localized errors, if the patient image is sufficiently different from the template image, it is possible for the image intensity based segmentation method to fail, which would necessitate manual segmentation of both the cerebrum and the dural septa. The automatic segmentation reduces the time of computation and cumbersome manual editing, although it does not obviate a review of the segmentation. The results of the sensitivity analysis show that the pre-operative computational time can be further reduced several-fold by decreasing the sampling resolution of the atlas without significantly degrading the shift correction. The time window from the time the pre-operative MR images are acquired to the beginning of the neurosurgery can vary from a few hours to several days. In the atlas-based inverse model paradigm, the bulk of the computational cost is shifted pre-operatively, and therefore it is important that those computations be completed within that time window. The findings in this study will have important implications in ensuring the completion of pre-operative computations within the time constraints for the implementation of the atlas-based method in real time.

Acknowledgements

This work has been supported by the National Institutes of Health (NIH)—National Institute of Neurological Disorders and Stroke under Grant R01 NS049251-01A4. The authors would like to thank the resident surgeons, the operating room staff and the

radiology department at Vanderbilt University for their help in data collection. Most of the visualization algorithms were developed using Visualization Toolkit (http://www.vtk.org). Some segmentation and calculations were performed using Analyze AVW Version 9.0.

Appendix B

B.1 Computational Model

The following coupled equations used to describe the biphasic consolidation model are listed below:

$$\nabla \cdot G\nabla\vec{u} + \nabla\frac{G}{1-2\nu}\left(\nabla\cdot\vec{u}\right) - \alpha\nabla p = -\left(\rho_t - \rho_f\right)g \qquad (5.1)$$

$$\alpha\frac{\partial}{\partial t}\left(\nabla\cdot\vec{u}\right) + \frac{1}{S}\frac{\partial p}{\partial t} + k_c\left(p - p_c\right) = \nabla\cdot k\nabla p \qquad (5.2)$$

The term $\vec{u}$ is the displacement vector, p is the interstitial pressure, G is the shear modulus, ν is the Poisson's ratio, α is the ratio of fluid volume extracted to volume change of the tissue under compression, ρ_t is the tissue density, ρ_f is the fluid density, g is the gravitational unit vector, $1/S$ is the amount of fluid that can be forced into a tissue under a constant volume, t is the time, k_c is the capillary permeability, p_c is the intracapillary pressure, and k is the hydraulic conductivity. The equation (5.1) is the mechanical equilibrium equation to describe the solid phase. Equation (5.2) is a description of the fluid phase that relates the rate of fluid flow to the pressure gradients in accordance with the Darcy's law.

B.2 Boundary Conditions

The boundary conditions were the same as used in [73], and were used to model gravity and mannitol (a hyperosmotic drug) deformation conditions. The following figure shows the boundary conditions used for running the model.

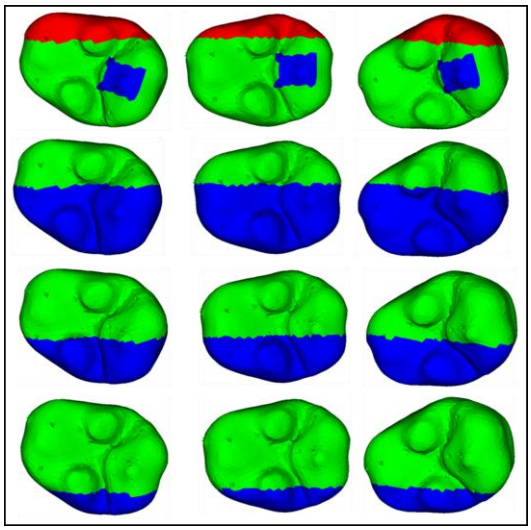

Figure 31. Boundary conditions: for displacement (first row) and pressure (second through fourth rows). The displacement boundary conditions are the same for both gravity and mannitol. The red regions are designated as stress free, the blue region is fixed, and the green region is no-slip condition. In the pressure boundary conditions, the green region is fixed atmospheric pressure and the blue region is no-flux pressure region. The second through fourth row show two different levels of CSF drainage. The three columns show the boundary conditions for different head orientations.

For the displacement boundary conditions (shown in the first row), the top red region is the stress free region, which is free to move unconstrained. The brainstem region (blue) experiences no deformation and is assigned fixed Dirichlet boundary conditions. All other nodes on the boundary (green region), including the internal boundaries such as the dural septa (not shown in the above figure), are assigned slip boundary conditions, that is, they cannot move in the normal direction, but movement in the tangential direction is permitted. For the pressure boundary conditions, the nodes exposed to atmospheric pressure are set as a Dirichlet boundary condition and the nodes submerged in fluid are

subject to Neumann boundary conditions, i.e. non-draining surfaces. The demarcation between the two regions is determined based on the level of CSF drainage, and the last three rows in Figure 31 show three different fluid drainage levels.

B.3 Material properties

The material properties used in the model [73] are listed in the table below.

TABLE 8
MATERIAL PROPERTIES

Symbol	Value	Units
E_{white}, E_{gray}	2100	N/m^2
E_{tumor}	100,000	N/m^2
ν	0.45	no units
ρ_t	1000	kg/m^3
ρ_t	1000	kg/m^3
g	9.81	m/s^2
α	1.0	no units
1/S	0.0	no units
k_{white}	1×10^{-10}	m^3s/kg
k_{gray}	5×10^{-12}	m^3s/kg
$k_{c1,\ white*}$	2.3×10^{-9}	Pa/s
$k_{c2,\ white*}$	4.6×10^{-9}	Pa/s
$k_{c3,\ white*}$	6.9×10^{-9}	Pa/s
$k_{c1,\ gray*}$	11.5×10^{-9}	Pa/s
$k_{c2,\ gray*}$	23.0×10^{-9}	Pa/s
$k_{c3,\ gray*}$	34.5×10^{-9}	Pa/s
p_c	-3633	Pa

* These values were used to simulate three different capillary permeability values resulting from the administration of mannitol and are designed to capture a physiological range.

B.4 Inverse Model

After building the atlas by varying the boundary and driving conditions, the model is solved inversely by computing the weighting coefficients α in the equation below.

$$\min \left\| M\boldsymbol{\alpha} - \boldsymbol{u}_{sparse} \right\|^2 \text{ s.t. } 0 \le \alpha_i \le 1 \text{ and } \sum_{i=1}^{m} \alpha_i \le 1 \tag{5.3}$$

M is the matrix of sparse atlas solutions which is $3n_s$ rows and m columns, n_s being the number of sparse points where the deformation is known from intraoperative tracking.

$\boldsymbol{u}_{sparse}$ is an $3n_s$ vector of those measured displacements. The first constraint ensures that all the weighting coefficients are positive. Hence if a solution in an atlas deforms in the incorrect direction, the objective function would weigh that solution lower instead of assigning a higher negative regression coefficient. The second constraint ensures that the solution is always interpolated, and not extrapolated.

CHAPTER VI

MANUSCRIPT 3 — Integrating retraction modeling into an atlas-based framework for brain shift prediction.

Manuscript in preparation: I. Chen, R. E. Ong, A. L. Simpson, K. Sun, R. C. Thompson, and M. I. Miga, *IEEE Trans Biomed Eng*

Introduction and Significance of Study

Specific intraoperative forces like resection and retraction influence the brain shift related tissue deformation. In the previous work in Chapter IV and Chapter V, these forces were not accounted for in the model. In the clinical data presented in that work, retractor was not used during surgery. Though the use of retractor is often avoided due to the risk of brain contusion or infarction, sometimes the use is necessary to explore the deep sub-surface tumor tissue. The premise of the atlas-based method is pre-computation, but the challenge with integrating retraction into that framework is that pre-computation might not feasible because the exact location of the retractor cannot predicted before the surgery. The viable solution to model retraction using the atlas-based framework would have to involve some active model solving during surgery. This work presents a method to integrate the retraction modeling with the atlas-based framework for brain shift using an intraoperative active-solve component.

Abstract

In recent work, an atlas-based statistical model for brain shift prediction which accounts for uncertainty in the intraoperative environment has been proposed. Previous work reported in literature using this technique did not account for local deformation caused by surgical retraction. It is challenging to precisely localize the retractor location prior to surgery and the retractor is often moved in the course of the procedure. This work proposes a technique that involves computing the retractor deformation in the operating room through a forward model solve and linearly superposing the solution with the pre-computed deformation atlas. As a result, the new method takes advantage of the atlas-based framework's accounting for uncertainties while also incorporating the effects of retraction with minimal intraoperative computing. This new approach was tested using simulation and phantom experiments. The results demonstrate a more accurate capturing of local retractor effects while not compromising the more distributed deformation effects.

Introduction

Brain shift induced misregistration is a well-studied problem in image-guided neurosurgery literature. This shift is a non-rigid brain tissue deformation that occurs due to gravity, hyperosmotic drugs, resection, and retraction forces [5, 7]. It has been known to cause misalignment errors between image and physical space in the range of 1 to 2.5 cm [5, 7, 73]. The techniques for shift compensation either involve intraoperative imaging or predictive computational modeling. The usage of volumetric imaging

modalities like MRI [5], CT [12] and ultrasound [26-28] for the estimation and correction of brain shift has been previously demonstrated. Cumbersomeness, necessity of non-ferromagnetic instruments, cost, exposure to radiation, and limited soft-tissue contrast are some of the concerns that have hindered the wide scale application of these modalities for shift compensation.

An alternative to these methods is to use computational modeling methods, such as finite element analysis. These predictive models are often coupled with intraoperative imaging data to provide an efficient compensation strategy. The imaging technique could be a traditional volumetric modality such as MRI, where the intraoperative image provides the driving conditions for the computational models. Clatz et. al. [34] and Wittek et. al. [33] used this strategy, combining intraoperative information from MRI images with a linear elastic model and a nonlinear model, respectively. In addition to full volumetric imaging, some work using partial volume imaging techniques with 3D ultrasound for shift correction has also been reported [26-28]. Alternatively, sparse intraoperative information can be supplied by modalities that are more cost effective, such as stereoscopic cameras [35, 36] or laser range scanner (LRS) devices [2, 37, 38, 40]. Unlike tomographic imaging devices, these modalities only provide information about the exposed brain surface during craniotomy. This sparse information cannot sufficiently constrain the forward-run of a biomechanical model without prior information or assumptions. The magnitude and direction of brain shift depends on variety of factors, such as head orientation, amount of fluid drainage, and pressure gradients caused by hyperosmotic drugs. These factors are difficult to predict or quantify to an exact precision during the surgery. To circumvent this challenge, Dumpuri et. al.

used an atlas-based framework [2, 3]. In this work, the authors chose Biot's consolidation model [53] to describe the constitutive mechanics of brain tissue. An atlas of forward-run model solutions is constructed with a variety of different driving conditions, such as head orientations and fluid drainage levels. Sparse information, computed as homologous points from either intraoperative LRS or post-operative MR, are then used to inversely solve the model through minimization of least mean squared error between the measurements and atlas predictions.

The work by Dumpuri et. al. was validated with clinical data in which no tissue retraction was performed. As a result accounting for retraction forces in their atlas was not necessary. Tissue retraction during neurosurgery is known to be associated with brain contusion or infarction but sometimes it may be necessary for adequate exposure, especially in tumor resection surgeries where the tumor is located deep beneath the surface [78, 79]. In [3], Dumpuri et. al. validated the atlas-based method with pre- and post-operative MR data and found a shift correction of 85% (ranging from 83% to 89%) in their clinical data. In contrast to Dumpuri et al.'s study, a similar analysis of the atlas-based method was investigated within the context of intraoperative data. The results of that study reduced the average shift recovery to 75% (ranging from 53% to 90%) which is likely due to the more extensive amount of shift that occurs intraoperatively [73]. The post-operative MR data acquired for the Dumpuri et al. study was acquired 24-48 hours after surgery, after the cranium was closed and some shift recovery had occurred. While retraction was not investigated in these studies, and it is not used to the same extent by surgeons; nevertheless, it does represent a standard mechanical event that is needed

during tumor resection therapy and its incorporation into compensation frameworks is needed.

In previous literature, Platenik et. al. [80] performed a study to quantify the performance of the modeling of tissue retraction first proposed by Miga et al. in [81]. Using Biot's consolidation model and Dirichlet boundary conditions of known retractor displacement (measured from a CT) along the tissue surface in contact with the retractor, the authors evaluated the performance of their predictive technique in porcine experiments. Their modeling technique recaptured 75-80% of shift caused by retraction, measured through stainless steel beads embedded in pig brain. Sun et. al. expanded this work to include retractor tracking information from stereoscopic microscopy images and demonstrated a 75% shift recapture as well [82]. These works are however, purely predictive models that do not resolve the uncertainties of the intraoperative environment.

Local displacement caused by tissue retraction occurs in conjunction with the other shift inducing factors like gravitational forces and hyperosmotic drugs. A viable solution for this problem may be by integrating the retraction forces into the pre-operative deformation atlas. One of the aspects that make the implementation of this approach challenging is that it is difficult to know the precise location of the retractor prior to surgery. The surgeon often varies the retractor location, depth and extent as he/she exposes tissue during surgery.

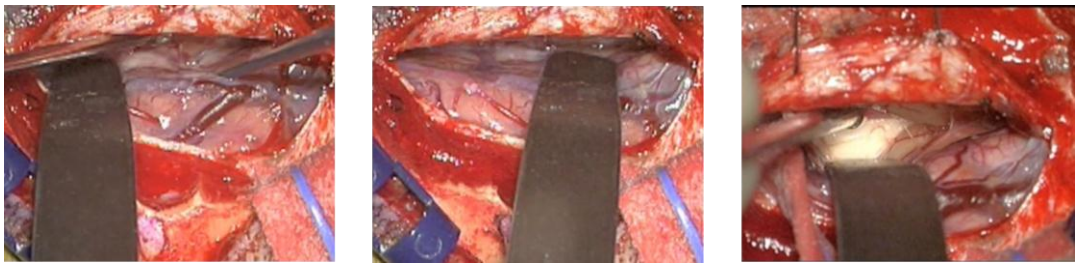

Figure 32. Retractor locations at different time points during a neurosurgery.

Figure 32 shows three different retractor locations and depths during the course of a single surgery. This provides the motivation for integrating retraction modeling as an active component into the atlas-based framework. Thus, the retraction component of deformation would not be pre-computed prior to surgery, but computed based on tracking the location of the retractor intraoperatively. In this paper, an approach is investigated that combines the pre-operative atlas with a component of forward solving capability in the intraoperative system to compensate for retraction. Simulation and phantom experiments are used to evaluate this retraction modeling approach.

Methods

Computational framework

Constitutive model. The constitutive properties of brain tissue in the past has been described by different models – linear elastic [34], non-linear [33], biphasic consolidation model [2] etc. Wittek et. al. compared three models of varying complexity – linear elastic, hyperelastic and hyperviscoelastic and found that they performed comparably for predicting brain shift deformation magnitudes [83]. As we are using a single phase tissue-like material in our phantoms, and given that elastic models are a reasonably good shift-

correction model, in this work a linear elastic model has been adopted. The primary goal of this work is to study the feasibility of integrating retraction modeling into an atlas-based system, where the choice of particular constitutive laws may be less important. Secondly, the method is evaluated with simulation and phantom experiments to understand its predictive fidelity. The linear elastic model is described by the following equation:

$$\nabla \bullet G \nabla \mathbf{u} + \nabla \frac{G}{1-2\nu}(\nabla \bullet \mathbf{u}) = -\left(\rho_t - \rho_f\right)\mathbf{g} \qquad (6.1)$$

In the above equation, G is the shear modulus (1050 N/m^2), $\mathbf{u}$ is the displacement vector, ν is the Poisson's ratio (0.45), ρ_t is tissue density (1000 kg/m^3), ρ_f the fluid density (1000 kg/m^3), and $\mathbf{g}$ is the gravitational vector.

While it has been suggested that hyperosmotic drugs like mannitol may have a substantial role in intraoperative brain tissue deformation [3], in this work only gravitational forces will be studied in conjunction with retraction related deformation. The right hand side in equation (6.1) represents an approximation to the effect of buoyancy force changes caused by drainage of fluid (such as cerebrospinal fluid in neurosurgery). Thus the amount of deformation would depend on the amount of fluid drained and the orientation.

Atlas construction and inverse model. An atlas of deformations can be constructed by varying the boundary conditions (depending on head orientation) and forces (depending on the amount of fluid drained). For a hemispherical shape used in the simulation and phantom experiments in following sections, the base is fixed with Dirichlet boundary condition and the remaining surface is given stress free Neumann boundary condition. Using the sparse intraoperative data, from a laser range scan for instance, the atlas can be

inversely solved to give a volumetric deformation field. If the atlas solutions exceed the sparsely available data, it results in an ill-posed problem. Constraints such as those utilized in [73] can be used to circumvent that problem as shown in the equation below:

$$\min \left\| M\boldsymbol{\alpha} - \boldsymbol{u}_{\boldsymbol{sparse}} \right\|^2 \text{ s.t. } \alpha_i \geq 0 \text{ and } \sum_{i=1}^{m} \alpha_i \leq 1 \qquad (6.2)$$

In the above equation, M is the atlas of deformations with $n_s \times 3$ rows and m columns, where n_s is the number of sparse intraoperative measurements and m is the number of atlas model solutions. $\boldsymbol{\alpha}$ is a vector of weighting coefficients that is the variable being optimized in this equation and $\boldsymbol{u}_{sparse}$ is the $n_s \times 3$ vector of measurements. The equation above was solved with an implementation of the active set method for quadratic programming in the Optimization Toolbox of MATLAB® (Mathworks Inc) [65].

Integration of retraction. The basic technique for modeling retraction forces will be similar to that of [80], where the mesh is split by duplicating the nodes at the tissue-retractor interface [81]. The generalized schematic of the workflow is shown in Figure 33 below.

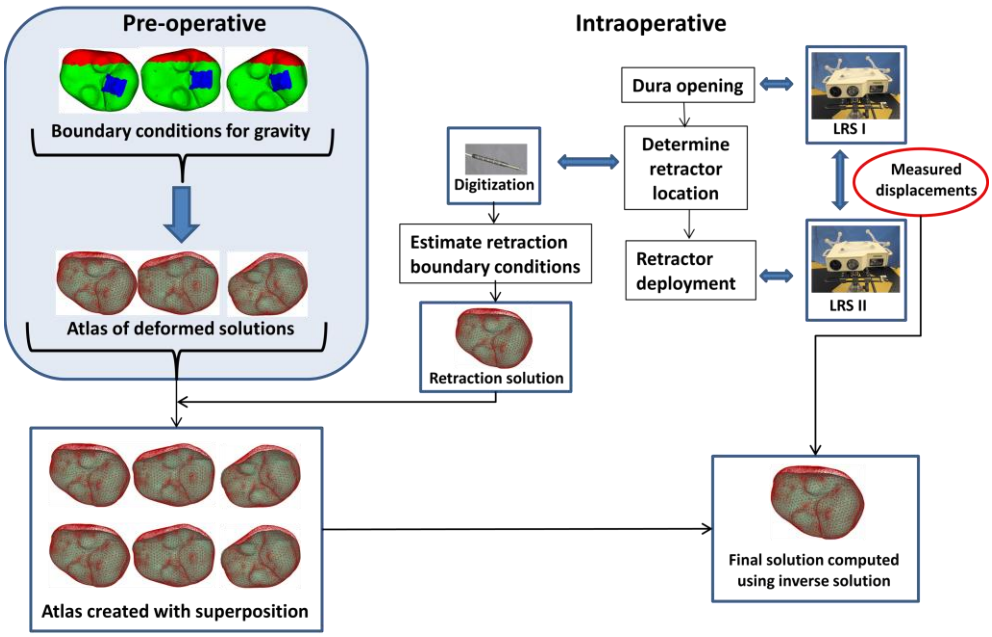

Figure 33. Schematic showing the overall workflow. Preoperatively, the deformation atlas is computed for gravity. Intraoperatively, first sparse data set is acquired after dura removal using a device such as a tracked LRS (measurement marked as LRS I in figure). After the location where the retractor will be placed is determined by the surgeon, the location can be digitized and used to estimate the retractor boundary conditions and construct a retraction model prediction. This can be linearly superposed with the gravity atlas computed pre-operatively to create an atlas that contains solutions both with and without retraction. After retractor deployment, another sparse data set can be acquired. Displacements can be computed from the two surfaces through homologous points and used to inversely solve the model.

After building the displacement atlas pre-operatively as in [73], intraoperativley, serial laser range scans would be acquired after opening the dura and after retractor deployment. The location of the retractor-tissue interface can be localized in the mesh intraoperatively by digitizing the retractor with a tracked tool tip. The side in contact with the retractor is prescribed fixed displacement along the direction normal to the retractor plane and free to move in the tangential directions. The other side has stress free boundary conditions and is free to move in all degrees of freedom. This model would be solved for localized deformations caused by retraction and then appended to the original

atlas. Though the main component of retraction deformation is in a direction normal to the retractor surface, to account for retractor slippage, the vector along which fixed displacement was prescribed, was perturbed within a 10º angle to build a retraction atlas. The inverse model was solved in the following manner.

$$\min \left\| \tilde{M}\boldsymbol{\alpha} - \boldsymbol{u}_{\boldsymbol{sparse}} \right\|^2 \text{ s.t. } \alpha_i \geq 0, \sum_{i=1}^{m} \alpha_i \leq 1, \sum_{j=m+1}^{m+n_r} \alpha_j \leq 1 \qquad (6.3)$$

In the above, $\tilde{M}$ is new atlas that has m gravity and n_r retractor solutions. The least squared error is minimized subject to the constraints that the weighting coefficients for all gravity solutions sum to less than or equal to one as well as the weighting coefficients for all retraction solutions sum to less than or equal to one. The homologous points from the serial laser range scans ($\boldsymbol{u}_{\boldsymbol{sparse}}$ in equation (6.3)) are used as measurement points to inversely solve the model by minimization of least squared error.

Experimental evaluation

The method described above was evaluated with simulation as well as phantom experiments that are described in the section below.

Simulation experiments. The performance of the model would depend on the accuracy of tracking the retractor location in the OR. The goal of the simulation experiments is to study the effect of error introduced into the system through tracking inaccuracies. A hemispherical surface with ~2.1 L volume was created using VTK (Kitware Inc.) and then made into a tetrahedral mesh with 4.5 mm element size, resulting in ~100,000 elements and ~20,000 nodes. A gold standard solution was then created by deforming the

mesh using gravity and retraction boundary conditions simultaneously with the linear elastic model, as shown in Figure 34.

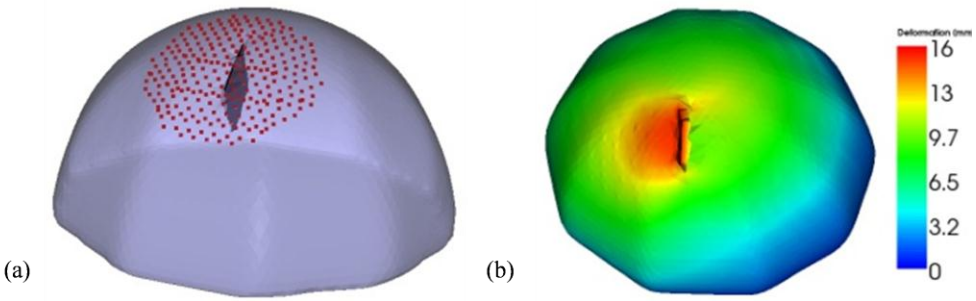

Figure 34. (a) Original undeformed mesh overlaid with the retractor plane and points on the surface used to run the inverse model. (b) Deformed solution created with simultaneous application of retraction and gravity boundary conditions color coded with deformation magnitude indicated on colorbar in mm units, used as gold standard to evaluate simulation results.

Based on intraoperative procedure information, a 1.5 cm retraction is simulated for the gold standard solution. A "pre-operative atlas" that only contains gravity deformation solutions was then created using different orientations and fluid drainage levels. 13 orientations and 1 fluid level were used to create the atlas consisting of 13 solutions, to which retraction solutions were appended.

Upon completion of the atlas, a series of simulations to understand the effects of localization and rotational errors was conducted. More specifically, the location of the retractor plane was perturbed by translating or rotating it from its true location and a forward model for retraction was solved by retracting it a distance of various retraction amounts and angles from the original. Nine different retractor plane perturbations were used – ±0.5cm, ±1cm, ±15º, ±30º and the original plane. The inverse model was driven by a set of points contained in a circular patch of radius 4 cm, centered at the retractor location on the boundary. The shift prediction error was computed at the surface points used to drive the atlas as well as subsurface points located 6 cm radially around the

retractor location. In addition, the results were compared to an inverse solution using the preoperative atlas with gravity forces only.

Phantom experiments. Polyvinyl alcohol cryogel (PVAc) material was molded into a hemispherical shape of volume ~1.2 L. Surface and sub-surface glass beads were embedded that could be tracked in a CT scanner (Figure 35 (a)). The bottom of the phantom was then fixed to a platform in a container and filled with water. The water level could be controlled with a spigot on the side (Figure 35 (b)). The top of the container was fixed a retractor assembly, with which the PVAc phantom could be retracted to desired displacements (Figure 35 (c)). In addition to the acquisition of the CT scans, the location of the glass beads on the phantom was also localized using NDI Polaris Spectra® (Figure 35 (d)) and passively tracked tool tip (Figure 35 (e)).

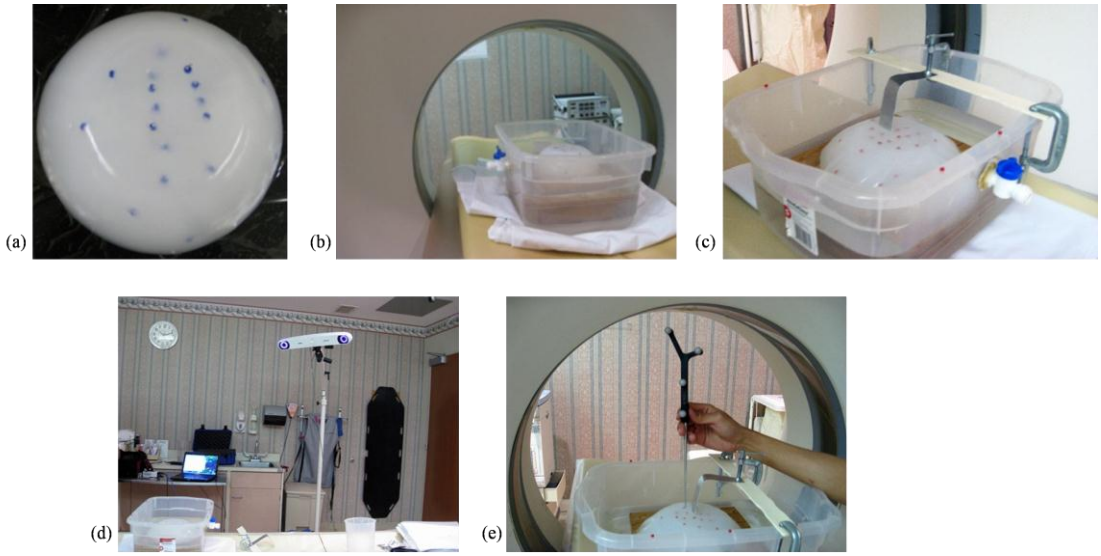

Figure 35. (a) PVAc phantom embedded with glass beads that can be tracked in a CT image. (b) Phantom fixed to the platform in the container, filled with water, being imaged in CT scanner. The water level is controlled with the spigot on the side. (c) The retraction assembly consists of a flat surface used as a retractor, which is fixed to the top of the container. (d) NDI Polaris Spectra® camera used for tracking (e) passively tracked tool used to localize the location of glass beads on the phantom surface.

Four serial CT scans were acquired: (1) phantom completely submerged in water in an undeformed state, (2) after some water has been drained, (3) after placing the retractor and (4) after performing the actual retraction.

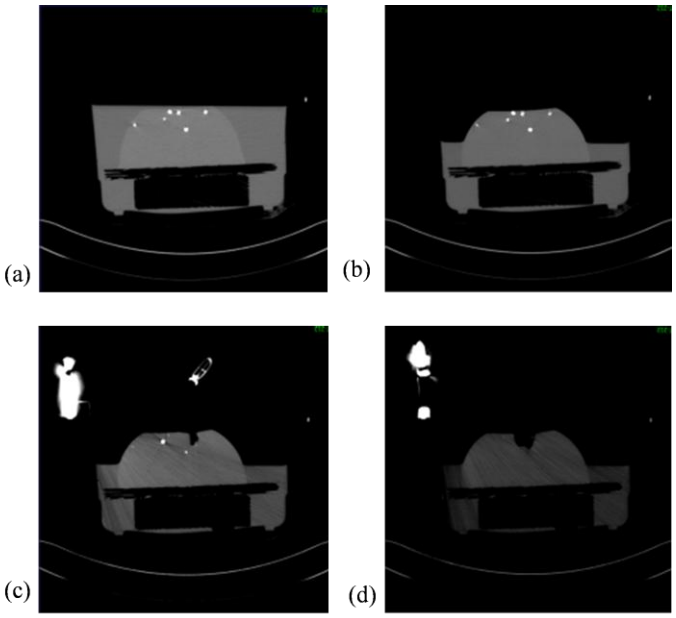

Figure 36. CT images acquired at different time points- (a) undeformed image, (b) after water drainage, (c) after retractor is placed and (d) after retractor is deployed.

The setup was not moved during the scans, so all the images were co-localized in the same space. The undeformed state image was segmented from CT images of the setup and used to construct a finite element mesh. The location of the retractor in the mesh was obtained from the third scan (Figure 36 (c)) and used to split the nodes along that plane. A deformation atlas containing gravity solutions and superposed retractor solutions was constructed and markers on the surface were used to run the inverse model. The retraction modeling technique was evaluated with five phantom datasets, with the tracking performed for three of the five cases.

Simulation experiments. The percent shift correction at the surface and subsurface points for the gravity atlas alone and the joint atlas containing gravity and superposed retraction solutions is shown in Figure 37 below.

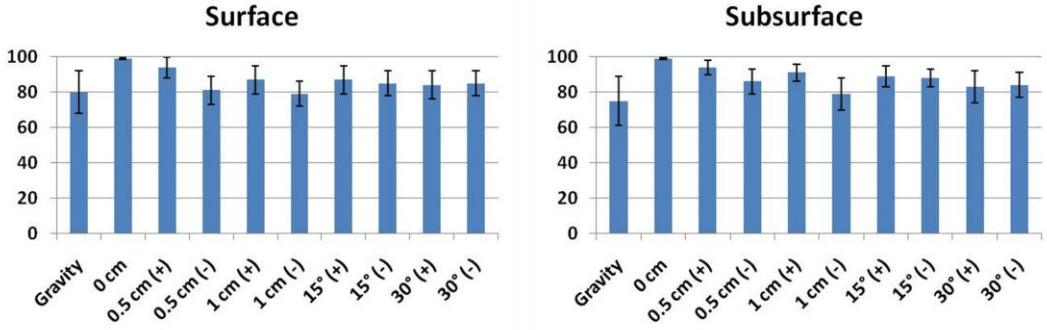

Figure 37. The left graph shows the percent shift correction at the surface points for the atlas with gravity alone and with superposed retraction solutions with various displacements and orientation. The graph on right shows the data for subsurface points. The numbers on the x-axis show the various perturbations of the retractor plane as discussed in section 2.2, with '0' being the unperturbed location.

The mean shift correction is typically higher for most cases for both the surface and sub-surface points using the superposed retraction atlas. Since the percent correction for the points don't fall into a normal distribution, as determined by the Kolmogorov-Smirnov test ($p<0.05$), the correction for each of the solutions that incorporate retraction was compared to the solution from gravity atlas alone using the Wilcoxon rank sum test. With a $p<0.05$ significance, the shift correction results for the retraction solutions are different than the ones with gravity alone, except for the case where the retractor plane was moved -0.5 cm, where the null hypothesis could not be rejected.

Phantom experiments. The atlas-based modeling technique with the gravity atlas alone and retraction superposed atlas were compared with the five phantom datasets. The

number of markers and the measured displacements for each dataset is shown in the table below.

TABLE 9. Number of markers and measured displacements for the five phantom datasets.

	Surface			Sub-surface			
#	# markers	Average measured displacement (mm)	Maximum measured displacement (mm)	# markers	Average measured displacement (mm)	Maximum measured displacement (mm)	Tracking available
1	10	12.9±4.0	17.5	6	7.4±2.6	11.3	No
2	14	8.8±2.5	13.1	12	5.9±2.0	9.5	No
3	15	18.0±1.6	21.2	10	15.0±2.9	20.2	Yes
4	12	23.1±0.6	23.7	11	16.3±3.5	20.0	Yes
5	12	23.1±2.4	27.6	11	13.2±5.6	26.9	Yes

The percent shift correction is defined as percent of difference between predicted and measured shift as compared to measured shift. For the five phantom datasets, it is reported at the surface points (which were used to constrain the least squared error solution) and subsurface points, using the gravity atlas and the superposed retraction atlas in the following figure.

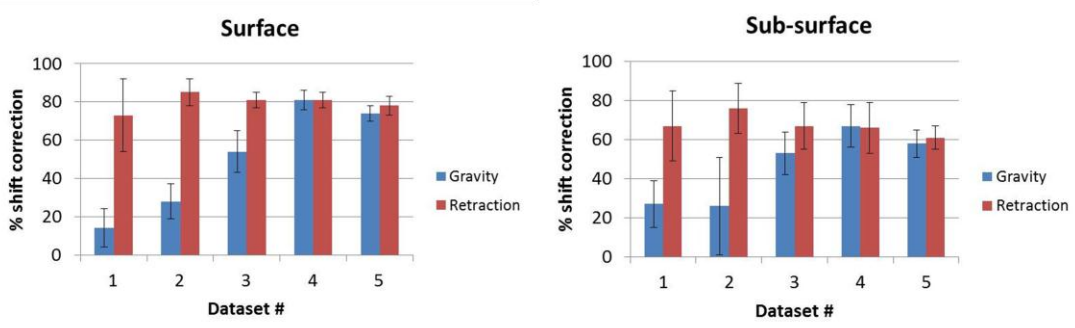

Figure 38. The % shift correction for surface and sub-surface points for the five phantom datasets in Table 9 using the gravity atlas and the superposed retraction atlas.

The percent shift correction data computed using the different atlases does not fall into a standardized normal distribution, as determined by the Kolmogorov-Smirnov test ($p<0.05$). Using the Wilcoxon rank sum test, for the surface points, the superposed retraction atlas significantly ($p<0.05$) improved the shift correction results for all datasets

except for dataset #4. For the subsurface points, there is a significant ($p<0.05$) increase in shift correction for the first three datasets, while there is no statistical change in the last two datasets.

The superposed retraction atlas contained both gravity solutions alone as well as retraction solutions. The following figure shows the proportion of the contribution of gravity and retraction solutions for the results reconstructed with the superposed retraction atlas.

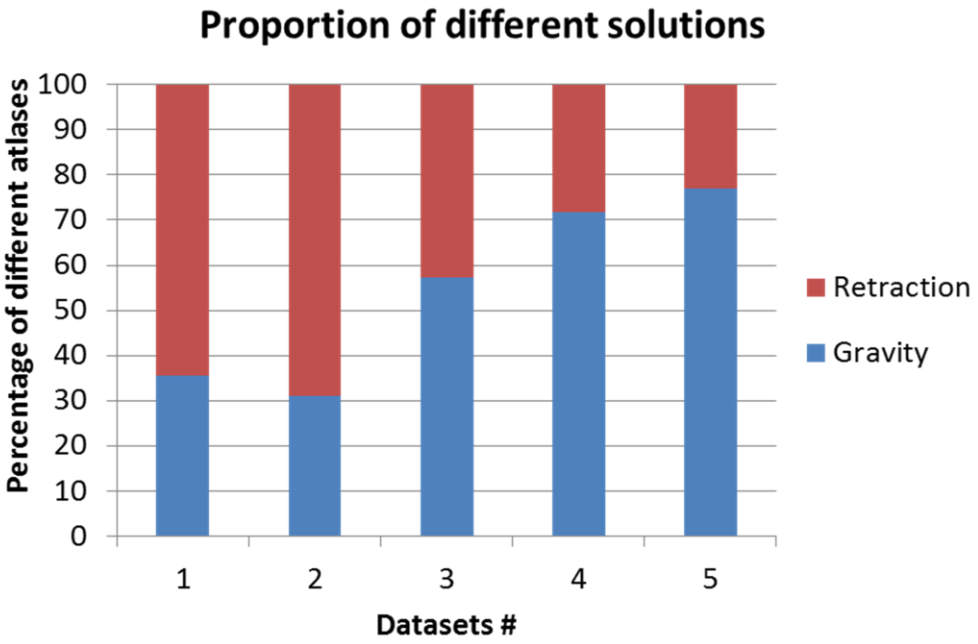

Figure 39. Percentage of contribution from different atlases to the solution reconstructed from the superposed retraction atlas.

The measured displacement magnitudes at the embedded markers after fluid drainage and after retraction for the five datasets are shown below.

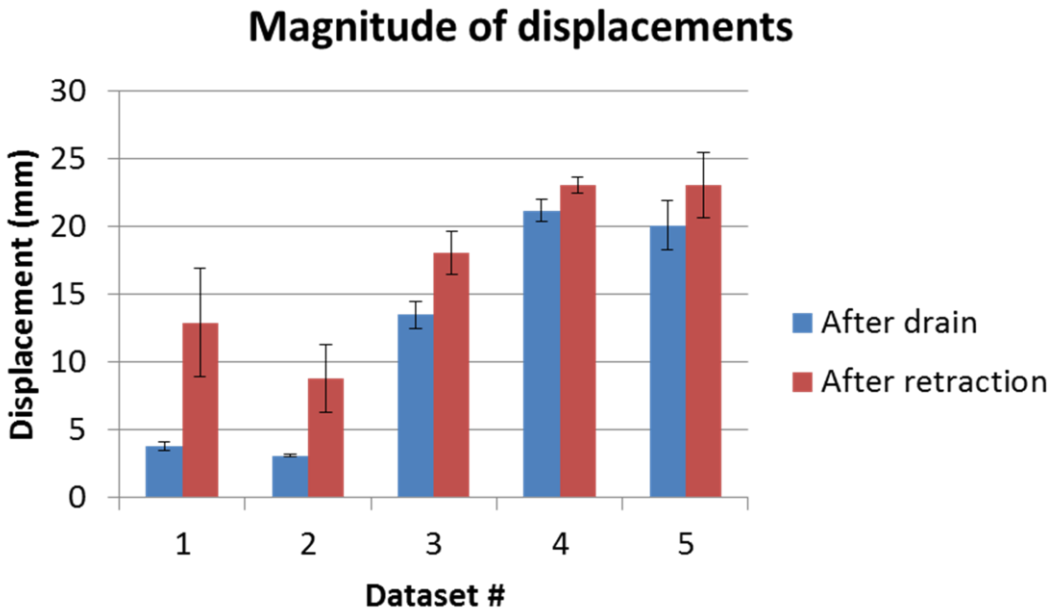

Figure 40. Measured displacements at embedded surface bead markers after fluid drainage and after retraction for the five datasets.

It is important to note that the displacement after retraction is a cumulative magnitude of both drainage and retraction applied in succession. The deformation caused by gravity is relatively small for the first two datasets, and the contribution of retraction to the overall deformation is larger. This is reflected in the percentage of retraction solutions picked from the superposed atlas for the first two datasets in Figure 39. The contribution by retraction is smaller in the last three datasets, and this trend is also reflected in the proportion of the weighting coefficients in the superposed atlas, as shown in Figure 39.

Discussion

The non-rigid deformation of brain tissue during surgery causes substantial error in the image guidance system. Usage of predictive computational models have shown promise because of cost efficiency and adaptability to wide range of data. The atlas-based

method for brain shift correction was developed to account for uncertainties in the intraoperative environment that affected the characteristic of deformation but was difficult to determine to exact precision during surgery. The papers published in the past using the atlas-based method do not account for some intraoperative forces such as resection and retraction [3, 73]. The work presented in this paper presents a method to integrate retraction modeling in the atlas-based framework. The simulation experiments demonstrated that the average percent shift correction obtained for surface and subsurface points is improved if retraction forces are accounted for in the model, even in the case of gross retractor alignment issues. This is interesting in that even if the retractor displacement is grossly incorrect, coefficient combinations are generated from the atlas technique to compensate for this gross tracking inaccuracy.

The results of the phantom experiments (Figure 38) showed a significant improvement for surface shift correction four out of five datasets. Through the use of the superposed retraction atlas, the first two datasets, the overall average shift correction improved by 57–59%, the third dataset showed an improvement by 27%, the fourth dataset showed no change, and the fifth dataset showed an improvement by 4%. The subsurface points mirrored this trend. The difference between different degrees of improvement of shift correction in different datasets can be explained by the nature of displacements. As shown in Figure 40, the magnitude of gravity displacement is smaller in the first two cases compared to the other cases. The following figure shows the gravity, retraction, and combined gravity and retraction measurements for datasets #2 and #3.

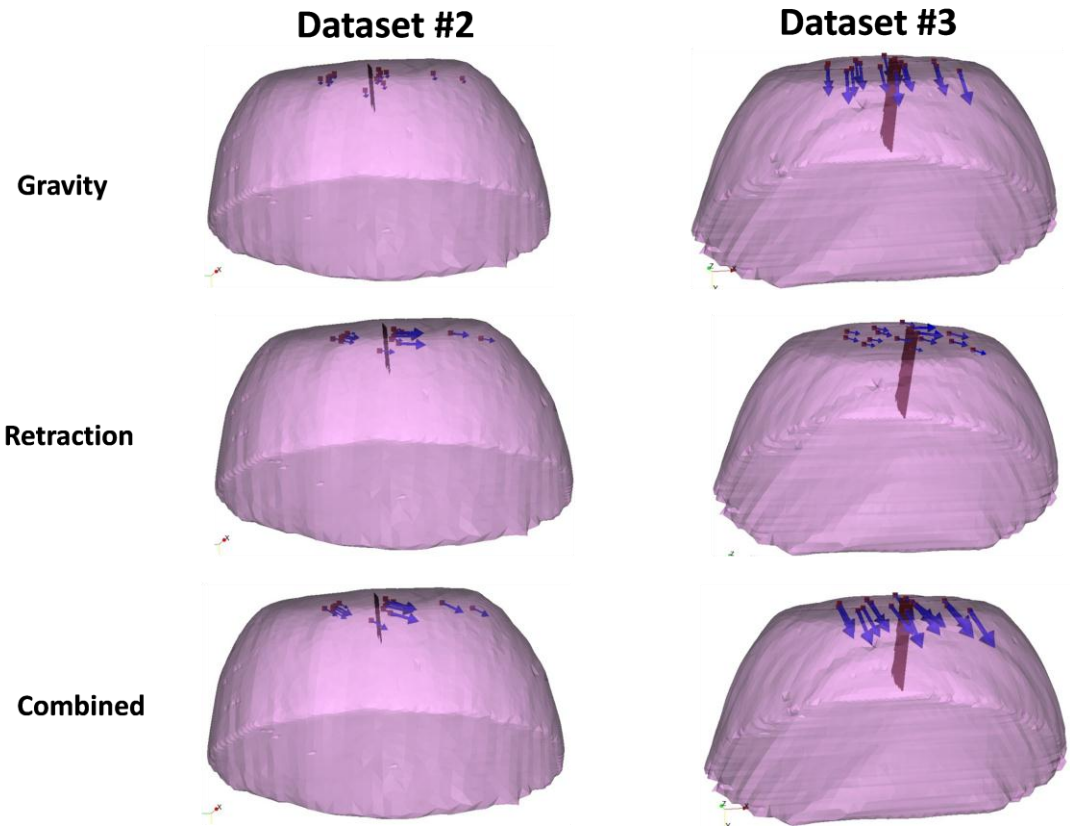

Figure 41. Measurements for deformations caused by gravity, retraction and combined forces for datasets #2 and #3. The red surface is the retractor.

The gravity deformation is almost in the vertical direction whereas the retraction deformation is nearly horizontal in Figure 41. Due to the relative magnitudes of the two forces in datasets #2 and #3, the combined deformation is weighted towards the horizontal direction for dataset #2 and the vertical direction for dataset #3. The gravity atlas is formed by tilting the phantom orientation around the vertical direction. Due to the more dominant gravitational component in dataset #3, the gravity atlas corrects for a larger extent in dataset #3 than dataset #2, which has a more dominant retraction component. This is demonstrated in the figure below.

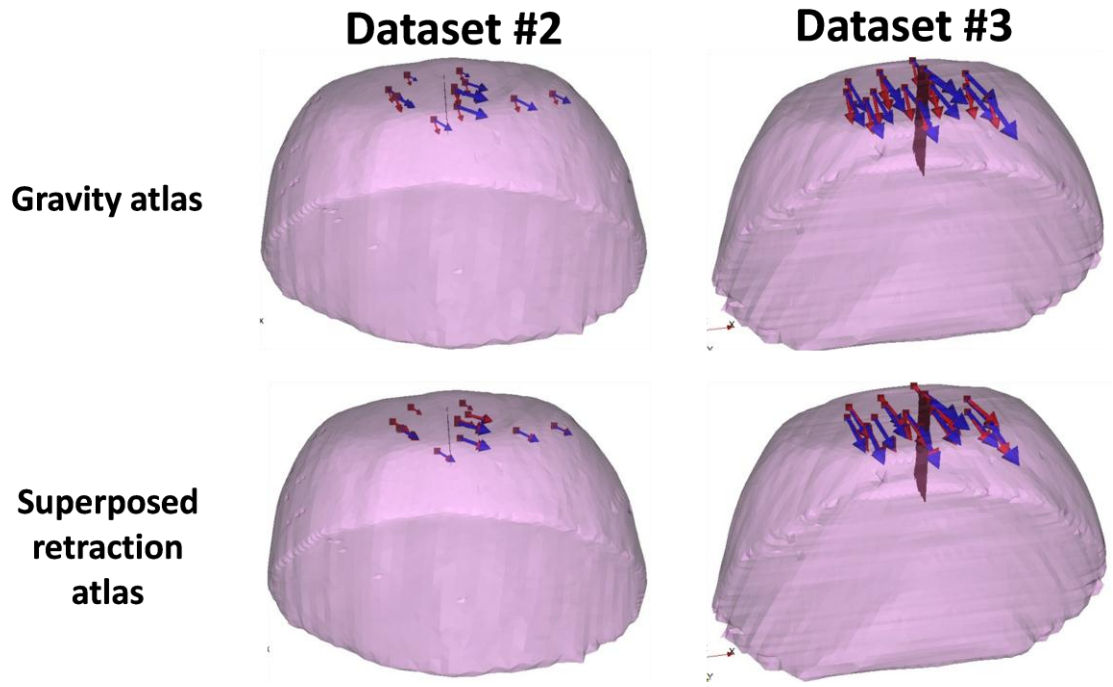

Figure 42. The measured vectors (blue) and the predicted vectors (red) using the gravity atlas and the superposed retractor atlas for datasets #2 and #3.

Figure 42 illustrates the gravity atlas performing very poorly for dataset #2 because of the dominant retractor component and performing moderately better for dataset #3 because the gravity component is more comparable in magnitude to the retractor component. The superposed retractor atlas performs comparably in both the datasets. This same reason explains why dataset #5 only experienced a 4% shift correction improvement with the superposed retractor atlas, as seen in Figure 40, the contribution of gravity deformation was much larger. The following figure shows the displacement measurement and model predictions at individual surface markers for phantom dataset #3.

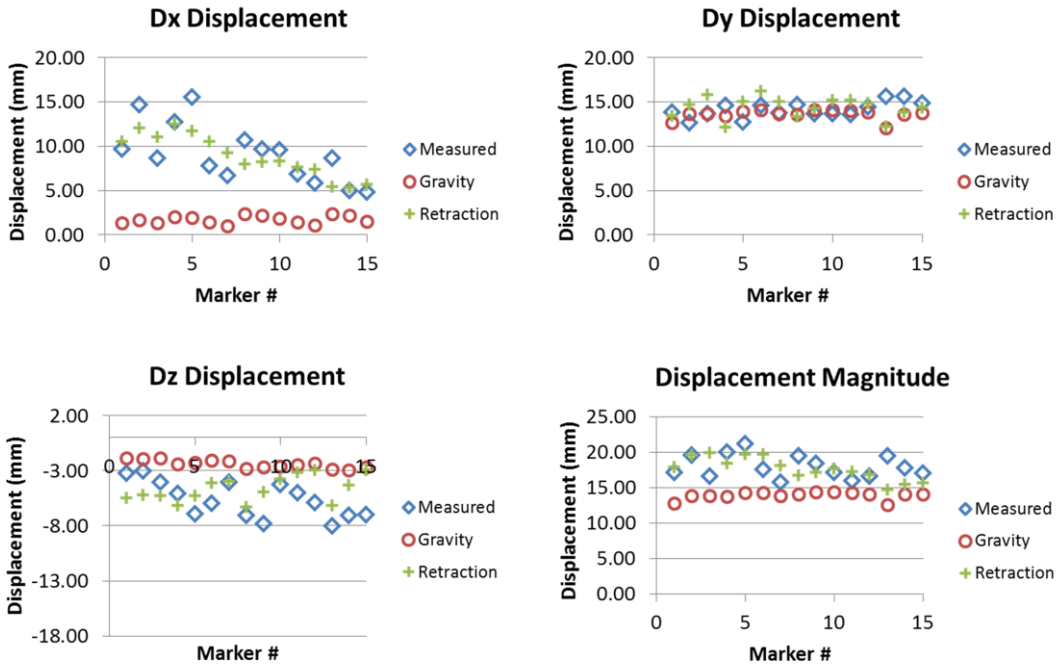

Figure 43. Comparison of the measured displacement with the prediction made using gravity atlas alone and retractor superposed gravity atlas in x (top left), y (top right), z (bottom left) directions and overall magnitude (bottom right) for phantom dataset #3.

When looking at the overall pattern of displacements, the gravity atlas produces more uniform deformations, which do not account for the local variations locally in a smaller sub-region caused by retraction forces. The local variations are better captured by the atlas that contains retractor solutions.

Lastly, the results for phantom dataset #4 showed no change from the use of superposed retractor atlas vs the gravity atlas and merit some additional examination. The following figure shows the deformation caused by retraction alone for dataset #4 and the correction for a forward model solve of retraction boundary conditions.

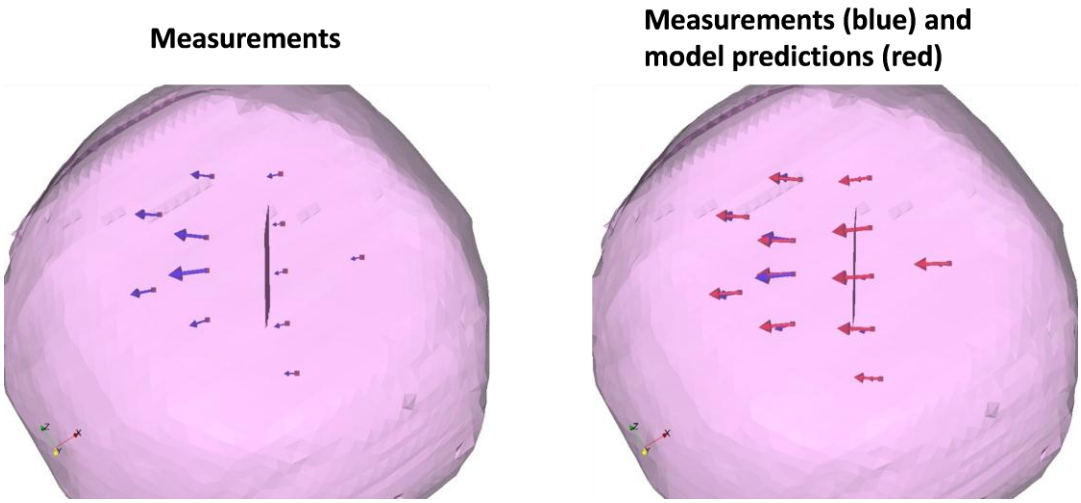

Figure 44. The deformation caused by retraction for dataset #4 and the model prediction using the forward solve of retractor boundary conditions.

The retractor moved from right to left direction, the markers on the right side of retractor experienced very small amount of deformation. This pattern was anomalous as compared to the other datasets and could be due to experimental error in the way the phantom was made or difference in the experimental setup. The retractor model prediction did not perform well in this case, and as a result, the use of the superposed retractor atlas did not cause any improvement.

There are several sources of error in the proposed method including the localization or tracking error. The location of the retractor in the phantom was determined by localizing the retractor plane and the mesh was split along the corresponding nodes in the undeformed state. However when the retractor plane is localized, the fluid drainage has already occurred. An assumption was also made that the direction of retraction was normal to this recorded surface, however the slipping or sliding of retractor would also result in some error. This was countered to some degree by building the retractor atlas through perturbation of the angle of retractor normal, as described previously. The effect of this error on the model prediction was small and this was supported by the simulation

experiment results in Figure 37. Optical tracking was also integrated into the phantom experiment and results (shown in Appendix C) were comparable to localization in the images. The PVAc phantom experimental setup was unconstrained except being fixed at the base, whereas the behavior of the brain tissue in a constrained cranial space might be different. Another potential weakness that was not addressed in this work was that in a clinical setting, the size of the exposed craniotomy may be relatively small and the retractor may conceal features for homologous point analysis. In future work, this method of modeling retraction will be explored in clinical setting using the optical tracking setup.

Conclusions

In this paper, a method to integrate retraction modeling into the atlas-based framework to compensate for brain shift in the OR was presented and evaluated with simulation and phantom studies. The atlas-based framework of brain shift computation accounts for the uncertainties in the intraoperative environment by pre-computing the deformations through different perturbations of boundary conditions and applied forces. This work presents a novel yet simple way to integrate retraction into the atlas-based brain shift computation framework. The method is completely compatible with OR workflow and minimally cumbersome. While this work does not incorporate all surgical variables, the goal of this work was to study the feasibility of the integration of retraction modeling by active solving and linear superposition. The preliminary results presented here indicate this approach to be a promising avenue to pursue.

Acknowledgements

This work has been supported by the National Institutes of Health (NIH)—National Institute of Neurological Disorders and Stroke under Grant R01 NS049251-01A4. The authors would like to thank the CT technicians in the Department of Radiology at Vanderbilt University for their help in data collection. Most of the visualization algorithms were developed using Visualization Toolkit (http://www.vtk.org). Some segmentation and calculations were performed using Analyze AVW Version 9.0.

Appendix C

The previous results presented were computed exclusively using the CT images. In the experiment, in addition to the CT data, the location of the embedded markers was also recorded using optical tracking that is typically available during surgery. The tracked data were registered to the CT images using fixed fiducials. The table below shows the fiducial registration error (FRE) and the target registration error (TRE) for the markers.

TABLE 10: FRE and TRE for the registration between image and physical space. The FRE was computed using the rigid markers fixed to the assembly and the TRE was computed using the surface markers.

Dataset #	# fiducial markers	FRE (mm)	# target markers	TRE (mm)
3	6	0.6±0.2	15	1.8±0.7
4	5	0.7±0.5	12	1.9±1.3
5	8	0.7±1.7	12	1.9±1.0

The tracking data was only available for the phantom datasets #3–5. The errors listed are a composite of both the localization error of the markers in the image and the registration error. The shift correction results obtained using the tracking data is shown in the figure below.

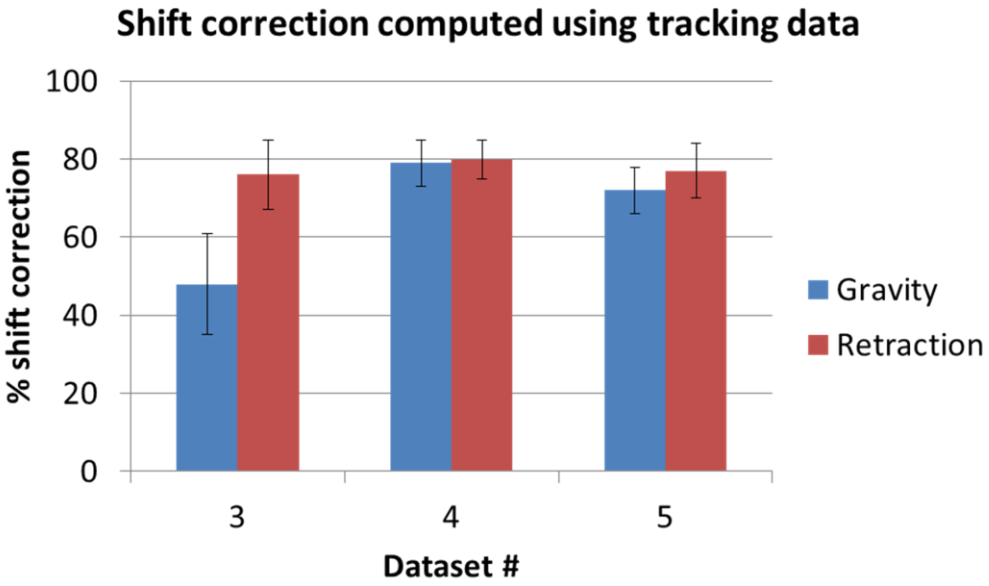

Figure 45. Shift correction results using tracking data for phantom datasets #3–5

Comparing these results to the shift correction results obtained using data from the images for phantom datasets #3–5, the values are comparable and follow a similar trend.

CHAPTER VII

MANUSCRIPT 4 — Preliminary work towards computational tumor growth model of a space occupying lesion for estimation of stresses associated with resection

Original manuscript: I. Garg, M. I. Miga, "Preliminary investigation of the inhibitory effects of mechanical stress in tumor growth" *SPIE Medical Imaging 2008: Visualization, Image-Guided Procedures, and Modeling,* vol. 6918, 2008

Introduction and Significance of Study

The results shown in Chapter IV indicated that local resection forces acting on tissue during surgery are not well accounted for in the current model. In the work presented above, resection was modeled by decoupling the tumor nodes from the mesh and effectively employing a stress free boundary condition on the resection cavity. In our experience, often the behavior of the tissue is similar to the Figure 46 which shows a pre- and post- resection LRS in a typical case. Here we see that the displacement vectors move not only in the direction of gravity, but also inward towards the center of the resection cavity.

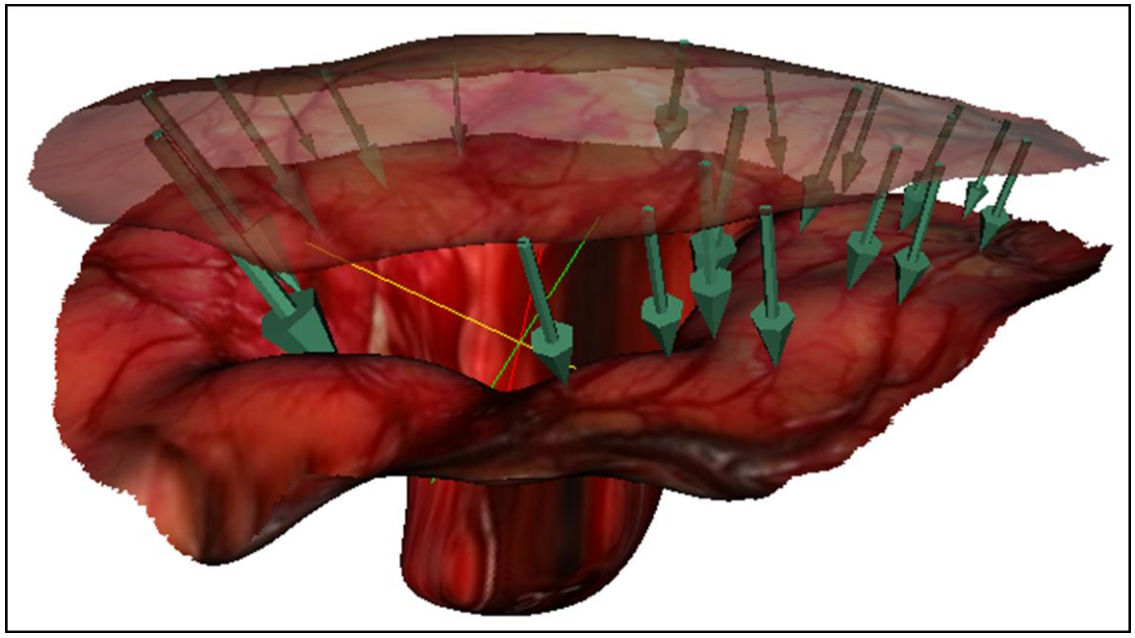

Figure 46: Pre- and post-resection LRS overlaid with the displacements between the homologous points

Some preliminary work was directed toward this in [84], in that work, the new surface created by tumor node deletion was prescribed a spatially heterogeneous decompressive stress boundary condition to attempt to partially collapse and debulk the tissue. At the sub-cortical base the stresses were normal to the surface and around the perimeter walls, non-uniform stresses were directed radially towards the center. The values of applied stress were determined through empirical testing with data. While this is an interesting strategy, perhaps a better approach could be generated if the tumor growth process could be simulated such that decompressive effects could be parameterized as part of the deformation atlas. In order to gain a better understanding of the decompressive effect, it would be important to understand the strain stored in tissue generated through the mass effect of tumor growth. Developing a tumor growth simulation model might provide more insight into this interaction. This study is a preliminary realization of a one dimensional tumor growth model in an effort to understand the compressive stresses

generated by the tumor mass effect, which perhaps in the future could be used to model tumor resection more appropriately.

Abstract

In the past years different models have been formulated to explain the growth of gliomas in the brain. The most accepted model is based on a reaction-diffusion equation that describes the growth of the tumor as two separate components- a proliferative component and an invasive component. While many improvements have been made to this basic model, the work exploring the factors that naturally inhibit growth is insufficient. It is known that stress fields affect the growth of normal tissue. Due to the rigid skull surrounding the brain, mechanical stress might be an important factor in inhibiting the growth of gliomas. A realistic model of glioma growth would have to take that inhibitory effect into account. In this work a mathematical model based on the reaction-diffusion equation was used to describe tumor growth, and the affect of mechanical stresses caused by the mass effect of tumor cells was studied. An initial tumor cell concentration with a Gaussian distribution was assumed and tumor growth was simulated for two cases- one where growth was solely governed by the reaction-diffusion equation and second where mechanical stress inhibits growth by affecting the diffusivity. All the simulations were performed using the finite difference method. The results of simulations show that the proposed mechanism of inhibition could have a significant affect on tumor growth predictions. This could have implications for varied applications in the imaging field that use growth models, such as registration and model updated surgery.

Introduction

There are an estimated 13,000 deaths and 18,000 new cases every year for all primary malignant brain and central nervous system (CNS) tumors. This translates to an age-adjusted incidence rate of about 9 per 100,000 people. Gliomas, primary tumors of the supporting tissue of the nervous system, account for 77% of all primary malignant brain tumors [1]. Histologically gliomas are classified as astrocytomas or oligodendrogliomas and pathologically they are subclassified by grades depending on the proliferative potency of the tumor. Clinically the most common presentation of glioma are seizures, headache, mental change and hemiparesis [85]. The differential diagnosis of brain neoplasm is made based on history and exam. The confirmation of diagnosis is typically obtained by some imaging modality, gadolinium enhanced magnetic resonance imaging (MRI) being the current standard. The prognosis depends on the age of the patient at diagnosis and the histologic tumor type. In a 2005 report the Central Brain Tumor Registry of the United States (CBTRUS) reported that glioblastoma (the highest grade glioma) accounted for ~62% of the 20,974 cases of glioma in a period from 1998 to 2002 [86]. In general less than 30% of patients under 45 survive for more than 2 years. For patients over 65 that survival rate dips to an even bleaker ~2% [1]. In the recent past, research efforts to combat this deadly disease have been tremendous in fields ranging from epidemiology, biomedical engineering, genetics to molecular biology. Epidemiology studies study the patterns of glioma prevalence in the society to devise better screening. The engineering aspect is focused on new chemotherapy agents and surgical advances such as intraoperative image guidance. Basic sciences aim to answer fundamental questions about the mechanism of glioma initiation and growth, which could

contribute to better screening as well as therapy. Animal models and in vitro techniques have been indispensable for all this research and have aided the testing of mechanistic hypothesis and potential of chemo-therapeutic agents.

Mathematical modeling can also be a valuable tool to understand various factors that initiate, promote, and inhibit tumor growth. Tumor growth has been historically described by an exponential model, a Gompertz model or a logistic model. The aggressive invasion of healthy tissue makes gliomas unique. Glioma growth has been mathematically described in literature by a reaction-diffusion model [87, 88]. This model describes the rate of change of tumor cell concentration as a contribution of two components: proliferation and invasion. The proliferative component is typically described by a constant growth rate, leading to exponential growth. The invasive component is described by passive Fickian diffusion. Gliomas are known to invade white matter more aggressively than grey matter and Swanson et. al. accounted for this heterogeneous behavior by assigning a higher diffusion coefficient to white matter than gray matter (factor of 2-100) [87]. Several studies extending the reaction-diffusion model have since been published. Jbabdi et. al. used diffusion tensor imaging (DTI) for increased accuracy of anisotropic diffusivity [89]. Clatz et. al., in addition to using anisotropy information from DTI, also coupled the diffusion to mechanics and studied the deformation caused by glioma growth [90].

In vitro techniques when combined with mathematical models can become even more powerful tools for analysis. Stein et. al. successfully combined these techniques and provided quantitative comparisons between theory and experiment for glioblastoma growth mechanism [91]. In a landmark experimental paper Helminger et. al.

demonstrated that multicelluar tumor spheroids cultivated in mechanically resistant matrix grow until a threshold level of stress is attained [92]. Several studies describing mathematical models for the results presented in the paper have been published since [93, 94]. These studies use a system of coupled equations describing tumor cell concentration, nutrient concentration, and mechanical stress to model the phenomenon seen in vitro. Ambrosi et. al. use a non-linear elastic model [93], and Roose et. al. used a linear poroelasticity model [94]. In each case, the stress modulates tumor concentration via a coupling relationship.

There is a dichotomy in the literature of mathematical modeling of gliomas between models formulated for in vitro multicellular tumor spheroids and in vivo animal or human tumors. The mathematical models for latter tend to be more simplistic with fewer parameters such as the reaction-diffusion model with a proliferation constant and a diffusion constant. The models for explaining in vitro growth tend to be more complex and have a lot more parameters. Those parameters might be evaluated more easily for the in vitro models, however the increase in number of unknown parameters for macroscopic tumors in human subjects decreases simulation tractability. Ultimately in vitro tumor models provide understanding of basic growth and inhibitory mechanisms which, under careful consideration of those effects, can then be applied to macroscopic scales. Whereas multicellular tumor spheroids grow to a size of several micrometers, in vivo tumors (and gliomas) have a minimum threshold radius of a few millimeters for detection in common imaging modalities. Whereas every finding in vitro tumors may not be directly applicable to tumors some of the findings deserve to be examined in that light. The inhibitory effect of stress for glioma growth might be a significant factor since it grows in

the confined space of the cranium. The goal of this paper is to attempt to bridge the gap between these two areas by formulating a simplistic mathematical model for macroscopic glioma growth that accounts for the inhibitory effect of mechanical stress. In the following sections the mathematical model will be introduced, its implementation will be discussed, and the results of simulation experiments using the model will be presented.

Methods

Mathematical Model

The evolution of tumor cell concentration, c, is modeled by a reaction-diffusion equation similar to [87] as shown below,

$$\frac{\partial c}{\partial t} = \nabla \cdot (D \nabla c) + f(c) \qquad (7.1)$$

where D is the diffusion coefficient. The first term on the right hand side is the invasive component and represents the spreading of tumor driven by the concentration gradient. The second term represents the proliferative component represented as some function of the cell concentration. In our simulations, the proliferation is modeled by a logistic growth law, i.e.

$$f(c) = \beta(1 - \alpha c)c \qquad (7.2)$$

α and β are proliferation components in logistic growth. This represents an initial exponential growth which slows down eventually as the nutrients are consumed. This is physiologically consistent as brain parenchyma has a maximum carrying capacity for tumor cells, which has been shown to be around 3.5×10^4 cells/mm^3 [95].

The mechanical equilibrium equation describing the stresses in the system is shown below,

$$\nabla \cdot \sigma + f_{ext} = 0 \qquad (7.3)$$

Here σ is the stress tensor and f_{ext} is the sum of external forces acting on the system. The material was modeled as a linear elastic system. Details about the constitutive equations can be found in the appendix.

The inhibitory effect on growth by stress was implemented by coupling the diffusion coefficient to stress by an exponential decay relationship shown here,

$$D' = De^{-k\bar{\sigma}} \qquad (7.4)$$

where D' is the spatially varying diffusion coefficient and D is invariant diffusion constant, k is a scaling constant and in the above equation $\bar{\sigma}$ represents a yield stress such as Von Mises stress in this case. It is being hypothesized that the mechanical stress inhibits glioma growth by affecting its diffusion coefficient. Gliomas are characterized by an aggressive invasion of parenchyma and a decrease in diffusivity of tumor cells would physiologically produce the observable effect of increase in cell density over time. To this effect an exponential decay relationship was used between the yield stress and diffusion coefficient and the choice was made because of simplicity.

Implementation

Three different implementations of the basic model presented above were devised. An initial concentration with a normal distribution was used and equation (7.1) was solved with Neumann boundary conditions of zero flux. In the first implementation, there was no coupling between the diffusion coefficient and stress i.e. cell concentration

depended on the reaction-diffusion equation (equation (7.1)) only. This implementation will be referred to as 'Model 1'. In the other two implementations the diffusion coefficients were coupled to stress by equation (7.4), but the way the mechanical equilibrium equations were implemented differ. In the second implementation cell concentration gradients contribute to the external forces, i.e.

$$f_{ext} = \lambda \nabla c \qquad (7.5)$$

Here λ is a scaling constant. Dirichlet condition of zero displacement was used at outer boundary because tumor cannot diffuse across the skull. Stress free conditions were used on the inner boundary. This model will be referred to as 'Model 2'. This model is similar to approach proposed in [90] to calculate stresses. In the third implementation the mechanical equilibrium was driven by displacements of the tumor front. It was assumed that the mechanical stress does not start to inhibit tumor growth until a certain threshold size is reached. Equation (7.3) is solved with Dirichlet conditions at both the inner and outer boundaries. At the inner boundary the displacement is given by the difference in the position of the tumor front at that time step and the threshold size. At the outer boundary zero displacement is used as in 'Model 2'. This implementation of the model will be referred to as 'Model 3'. It's worthwhile to note here that the mechanical domain in 'Model 3' only consists of the portion of the tumor cell domain that excludes the threshold tumor size. In the following simulations, the results of these three models will be compared to each other.

Simulation Experiments

All the implementations were simulated using the finite difference approach in MATLAB. The time dependant equation (7.1) was solved with an explicit Euler scheme. The parameter values used for the simulations are tabulated in Table 11.

TABLE 11: Parameter values used for model simulations

Parameter	Symbol	Value
Diffusion coefficient	D	0.001 cm^2/day
Logistic growth parameter	α	1 day^{-1}
Logistic growth parameter	β	0.05 day^{-1}
Young's modulus	E	2100 Pa
Poisson's ratio	υ	0.45

Some of these values were drawn from literature and others were determined by numerical experimentation. For instance the value of diffusion coefficient is quite similar to the value used in [88]. A higher proliferation rate than [88] was used in this case because the value used in that paper caused a sharp drop in cell concentration in the beginning due to high diffusion and low proliferation rate. The mechanical properties of brain tissue i.e. the Young's modulus and Poisson's ratio were found in [2].

Results

The tumor cell concentration profiles obtained with the reaction-diffusion model using the logistic growth term are shown in Figure 47.

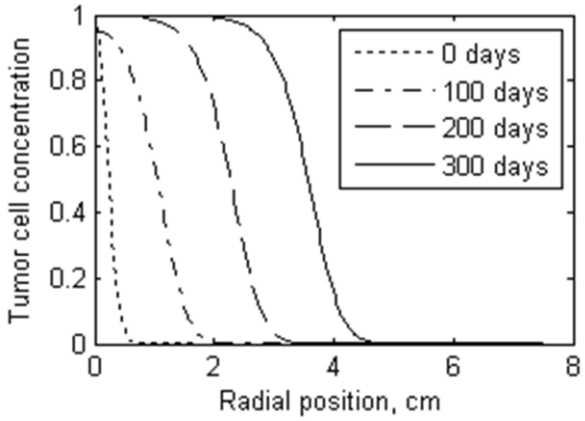

Figure 47. Traveling wave solutions for the reaction-diffusion equation (equation(7.1)) for tumor cell concentration. The concentration is normalized between a value of 0 and 1. The concentration distribution at 4 different time points is shown.

The figure shows tumor cell concentration profiles at four different time points. The cell concentrations in the figure are scaled between values of 0 and 1. The logistic growth caps the concentration at a certain maximum value. This approach, in our opinion, has a slight advantage over an implementation such as [90] where the exponential growth term is used and the cell concentration is manually constrained in the software beyond a certain maximum value. The concentration profiles follow travelling wave type solutions. It is worth pointing out that the peak concentration falls initially (100 days) while there's a greater spatial spread of the tumor. As the model progresses in time, the peak value is regained. This could be because of the choice of parameters. Initially the diffusion is dominant which spreads the tumor cells across the domain. Then as proliferation catches up, the peak concentration rises again while the tumor cells continue to invade healthy parenchyma.

The tumor cell concentration profiles obtained by the three models at different time points are shown in Figure 48.

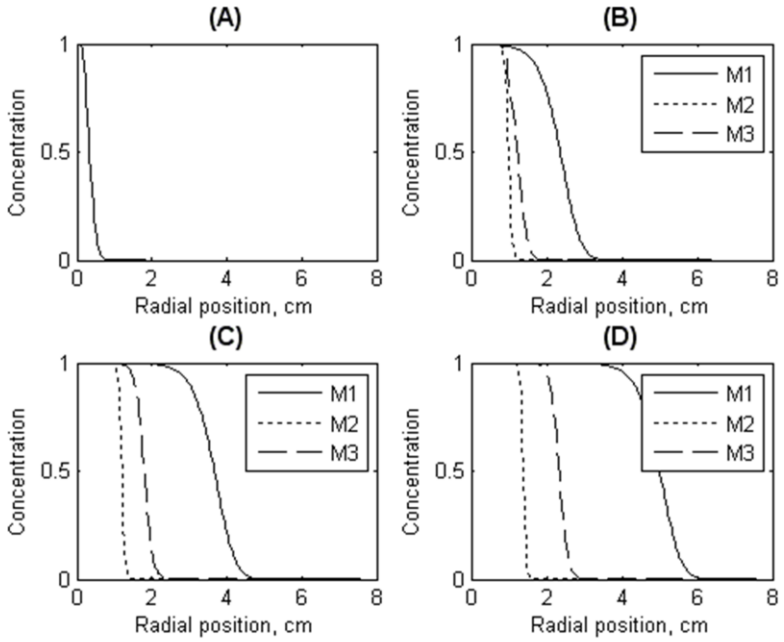

Figure 48. Comparison of the concentration profiles over time for three models. M1 refers to Model 2, M2 to Model 2 and M3 to Model 3. (a) shows the initial cell concentration and (b–d) shows the cell concentrations predicted by the models at 200, 300, and 400 days respectively.

The panel (a) shows the initial tumor cell concentration, which was common to all three models. Panels (b) through (d) show the tumor cell concentrations at 200, 300, and 400 days respectively as predicted by the three models. In each case Model 1, the simple reaction-diffusion model predicts the highest invasiveness for the tumor, followed by Model 3 and Model 2. At 200 days the concentration profiles predicted by Model 2 and Model 3 are relatively similar, but they diverge at future time points. The inhibitory effect in Model 2 is the greatest in part because in Model 3 it is assumed that the tumor grows freely without any effect of mechanical inhibition until it reaches a certain threshold size. In Model 2 stresses exert an inhibitory effect on growth from the beginning of model propagation. However, even when accounting for a quicker start, the rate of invasion is slower for Model 2. The stresses and thus the diffusion coefficients are dependent on the

choice of '*k*' in equation (7.4) and λ in equation (7.5) in Model 2. In Model 3, the diffusion coefficients are dependent only on '*k*'. '*k*' was kept consistent between the simulations for Model 2 and Model 3. As in [90], λ was an empirically determined parameter and its choice would explain the discrepancy in observed tumor profiles for Model 2 and Model 3.

The resulting radial displacements, radial stresses, and angular stresses for the three models are shown in Figure 49, Figure 50, and Figure 51 respectively.

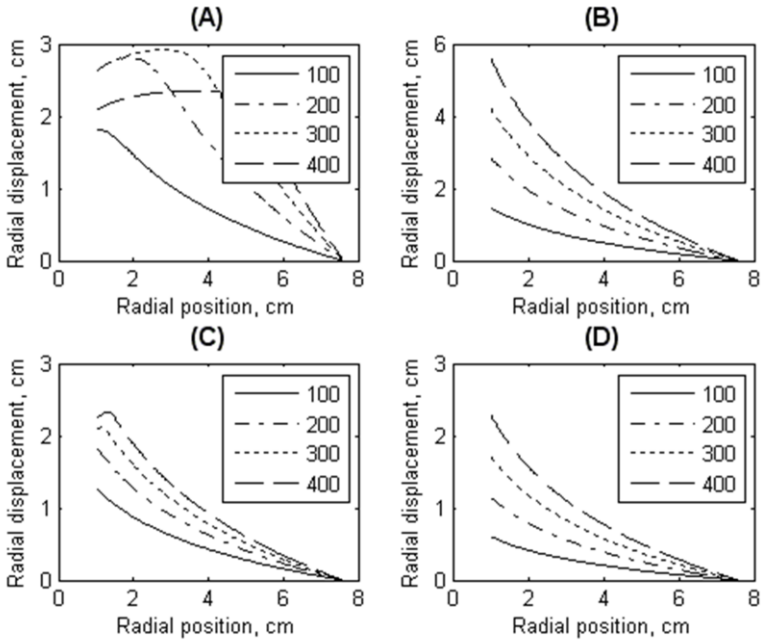

Figure 49. (a) and (b) show the brain tissue displacement in the radial direction for Model 1. In (a) the displacement was calculated by driving the mechanical equilibrium equation by the tumor cell concentration gradient and in (b) they were calculated by driving the mechanical equilibrium equation by the tumor front displacement. (c) and (d) show the results of radial displacements calculated by Model 2 and Model 3.

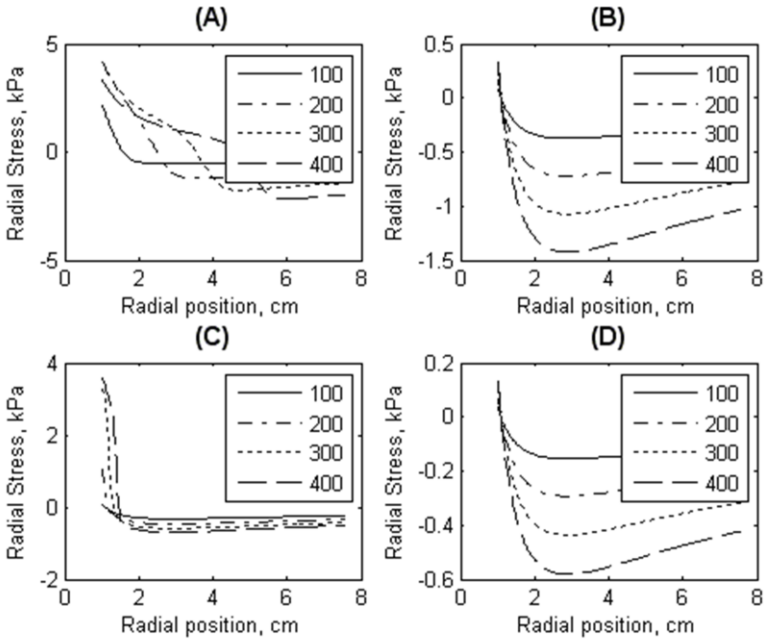

Figure 50. (a) and (b) show the radial stress in the brain tissue for Model 1. In (a) the radial stress was calculated by driving the mechanical equilibrium equation by the tumor cell concentration gradient and in (b) it was calculated by driving the mechanical equilibrium equation by the tumor front displacement. (c) and (d) show the results of radial stess calculated by Model 2 and Model 3.

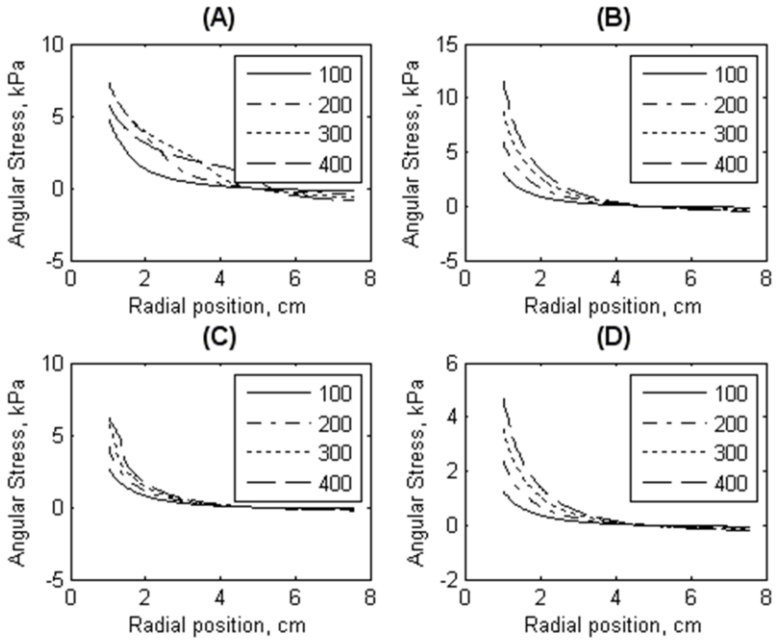

Figure 51. (a) and (b) show the angular stress in the brain tissue for Model 1. In (a) the angular stress was calculated by driving the mechanical equilibrium equation by the tumor cell concentration gradient and in (b) it was calculated by driving the mechanical equilibrium equation by the tumor front displacement. (c) and (d) show the results of angular stress calculated by Model 2 and Model 3.

In each case panels (a) and (b) show the results predicted by Model 1. Results for panel (a) were computed by driving the mechanical equilibrium equation with tumor cell concentration gradients (similar to Model 2). In panel (b) the results were computed by driving the mechanical equilibrium equation by tumor front displacements (similar to Model 3). Panels (c) and (d) show the results obtained from Model 2 and Model 3 respectively. As clarification, the difference between the first two panels and the last two panels is that for each case in (a) and (b) diffusion coefficients were not coupled to stress. The values predicted by all three models are on the same order of magnitude. Comparing the first two panels to the last two, the magnitudes of all three quantities are highest for Model 1. When comparing the displacements in Figure 49 (a) to Figure 49 (b) the displacements predicted by Model 1 are greater than Model 2 at 100, 200, and 300 days.

The dip in the displacements at 400 days for Model 1 (Figure 39 (a)) is unexpected since all other curves indicate an increase in displacement values as the model progresses in time. However, the results viewed in confluence with cell concentration gradients at the respective time points explain the dip. Initially there are larger concentration gradients in the inner portion of the domain and towards the exterior the gradient is very small. As the model progresses in time the cell concentration in the interior part of the domain level off due to logistic growth. Thus the cell concentration gradient is lowest close to the inner and outer boundary and highest in between. These gradients acting as an external force to drive mechanical equilibrium explain the observed results. The peaks in radial displacement curves in Figure 49 (a) and (b) correspond to the position of the highest cell concentration gradient at that time point. Radial displacements in Figure 49 (c) and (d) obtained from Model 1 and Model 3 respectively show consistently increasing displacements as model propagates in time, with lower displacement at each time point for Model 3. The radial stresses (Figure 50) are compressive in most of the domain which is expected since tumor growth would create a mass effect, pushing the healthy tissue closer to rigid skull boundary. Closer to the inner boundary the stresses are tensile. The tensile component is much stronger in Model 2 than Model 3. The value of compressive component of stress is quite similar in magnitude for all models. The angular stresses (Figure 51) in all cases are tensile. This trend is also expected since healthy brain parenchyma is modeled as a nearly incompressible material (Poisson's ratio of 0.45). Thus if the tissue is being compressed radially, it would experience stretching in the angular direction.

Discussion

The goal of this work was to assess the applicability of knowledge gained from in vitro tumor growth models to human glioma growth. In the past in vitro studies have shown that mechanical stress can have an inhibitory effect on tumor growth. Due to the growth of gliomas in the confined cranium space, that effect may be significant enough to be incorporated into macroscopic growth models. The results in [92] indicated that mechanical stress did not affect proliferation rates but decreased the rate of apoptosis and that led to a compaction of cells, which was supported by an observable increase in cell density in case of stress inhibited tumors. It was hypothesized that the mechanical stress inhibits glioma growth by affecting its invasiveness, which in the reaction-diffusion growth model is represented by a Fickian diffusion. More experimental work would be needed to formulate an appropriate relation that would be physiologically consistent. It is known that gliomas invade white matter more aggressively than grey matter and anisotropic diffusion coefficients have been used previously in literature to account for those differences. The work presented in this paper used a spatially variant diffusivity that was only affected by mechanical stress caused by tumor growth. However heterogeneous diffusion coefficients for gray and white matter would be relatively straightforward to integrate into this model framework. The brain parenchyma was assumed to have a linear elastic response to stress but different material properties can be modeled by changing the constitutive relationships. This model also assumes no intervening therapy but that can be modeled by modifying the reaction diffusion equation as in [88]. In Model 3 a minimum threshold size of 1 cm was assumed before it starts exerting an inhibitory affect. A more appropriate value would have to be experimentally

determined. While some parameter values were used from literature where they were available, all published models are unique and have their own set of assumptions. At times it was difficult to directly make use of those values and appropriate measures had to be determined by numerical experimentation. Since this was a preliminary investigation all the results presented in this paper are computational simulations and the next natural step would be use of the model to validate in vivo measures such as displacements caused by tumors in the brain parenchyma.

The computational simulations presented in this work show that stress could potentially have a significant effect on tumor growth. Two different implementations of a model where stress exerts an inhibitory effect on tumor growth were presented in this paper. In the Results sections part of the domain was clipped in presenting the results of Model 2 in Figures 49–51. This was done to ease the direct comparison of results from the two models because the stress acts on two slightly different domains. The displacements and radial stresses for the entire domain for Model 2 at one time point are shown in Figure 52.

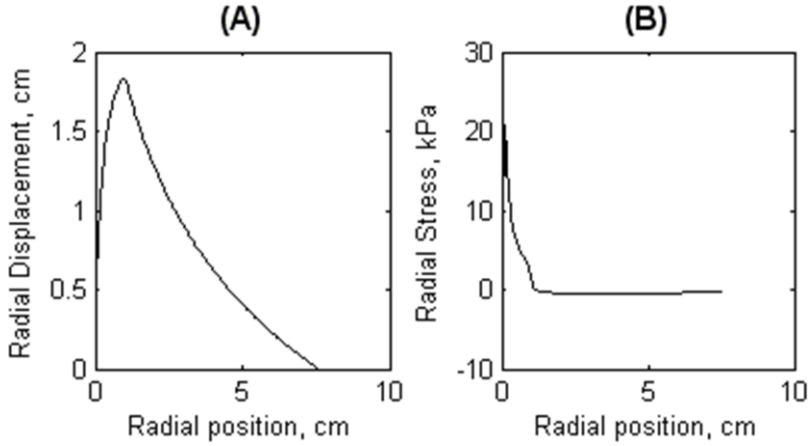

Figure 52. The (a) radial displacement and (b) radial stress for a time point in Model 2. As seen in panel (b), there is a strong tensile component of radial stress.

Part of the domain is in tension and while it is difficult to see due to scaling, the remainder is under compressive stresses (see panel (b)). The tensile effects are not consistent with physiological tumor growth. In that respect Model 3 might be a better choice. In the implementation of Model 3, the stress does not start to act or affect the growth until it reaches a certain threshold value. This is consistent with the finding in [92] that tumor spheroids grow in the mechanically resistant matrix until a growth-inhibitory threshold level of stress was attained. Also it is easier to directly use tumor front displacements to drive the mechanical model than empirically determining an indirect coupling factor for stress and concentration gradient, i.e. λ in equation (7.5). The change in tumor radius as predicted by the three models is shown in Figure 53. Model 2 and Model 3 predict a slower tumor growth than Model 1. These curves qualitatively resemble the initial part of results shown in [9] with a few notable differences. Since this model is applicable to tumor on the order of 1 cm, and spheroids grow to the order of micrometers the scale for tumor size and growth time is very different. The plateau effects of growth at longer times are not seen in the results in Figure 53.

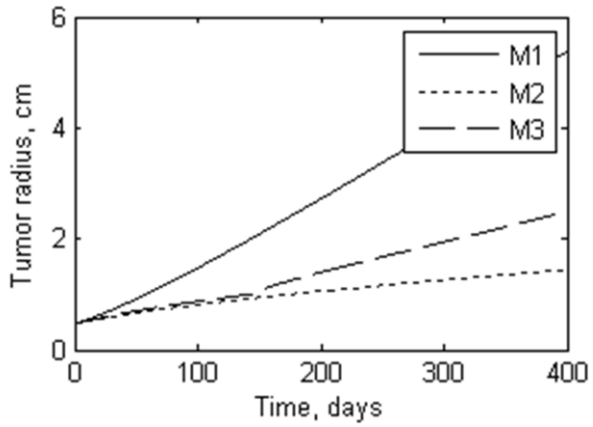

Figure 53. Change in tumor size as predicted by the three models over time.

That could be because of the aforementioned differences in medium of growth, temporal and spatial scales of tumor growth, or different tumor cell lines. The increase in tumor radius in 6 months as predicted by Models 1, 2 and 3 are 2 cm, 6 mm and 8mm respectively. As a comparison to a macroscopic glioma growth model an average tumor boundary displacement of 3 mm was reported in the same time period in [90]. The discrepancy could result from the choice of parameters. While all three models predict higher tumor boundary displacement than what is reported in [90], values predicted by Models 2 and 3 are much closer to the reported displacement.

Conclusions

There might be some benefit to integrating the insights gained from in vitro tumor growth models into macroscopic models for glioma growth. While the mathematical models for in vitro models afford the advantage of controlling and knowing more parameters and thus can be constructed with a greater degree of complexity for fine tuning such is not the case for macroscopic growth models. However it was demonstrated in this work that it might be worthwhile exploring some of the findings on that microscopic scale and applying them to macroscopic scale. The purpose of this study was a preliminary investigation into observing the inhibitory effects of stress and inferring general trends about the tumor growth. The simplicity provided by a single spatial dimension aids in a better understanding before a more complicated model can be pursued. Accurate macroscopic models of brain tumor growth could be used in many applications. For example, statistical atlases of brain function can be used in surgical

guidance to prevent the surgical invasion of important functional areas of the brain (e.g. motor cortex). Often, these atlases are based on "normal" brains. Understanding the movement of these statistical distributions of functional areas in response to disease growth may be very important for improving a patient's quality of life post-surgical outcome. In addition, recent findings have indicated that significant swelling of the brain can occur from the very initiation of tumor resective therapy. To improve guidance systems, it may be advantageous to correlate the degree of swelling with an accurate biomechanical model of disease growth. In so doing, important information for preoperative planning could be derived as well as the potential for guidance correction during the earliest stages of surgery.

Acknowledgements

This project was funded by NIH-National Institute for Neurological Disorders and Stroke Grant # R01 NS049251-01.

Appendix D

The appendix lists the details of the implementation of some aspects of the model. The model was implemented in polar coordinates. Equation (7.1) expanded out in polar coordinates is shown below.

$$\frac{\partial c}{\partial t} = \left(\frac{\partial^2 c}{\partial r^2} + \frac{1}{r}\frac{\partial c}{\partial r} + \frac{1}{r^2}\frac{\partial^2 c}{\partial \theta^2} \right) + f(c) \qquad (7.6)$$

The equation (7.3) written for polar coordinates when f_{ext} is zero is shown below in matrix form.

$$\nabla \cdot \begin{bmatrix} \sigma_{rr} & \sigma_{r\theta} \\ \sigma_{\theta r} & \sigma_{\theta\theta} \end{bmatrix} = 0 \tag{7.7}$$

For an axially symmetric problem, this equation reduces to the following [96].

$$\frac{\partial \sigma_{rr}}{\partial r} + \frac{1}{r}\left(\sigma_{rr} - \sigma_{\theta\theta}\right) = 0 \tag{7.8}$$

The constitutive equations for the linear, elastic, homogenous, and isotropic material for plane strain in polar coordinates are shown below.

$$\begin{aligned} \varepsilon_{rr} &= \frac{1}{E}\left[\sigma_{rr} - \upsilon\sigma_{\theta\theta}\right] \\ \varepsilon_{\theta\theta} &= \frac{1}{E}\left[\upsilon\sigma_{rr} - \sigma_{\theta\theta}\right] \\ \varepsilon_{r\theta} &= \frac{1}{2G}\sigma_{r\theta} = \frac{1}{2G}\sigma_{\theta r} = \varepsilon_{\theta r} \end{aligned} \tag{7.9}$$

In the equations above E is the Young's modulus of elasticity and υ is the Poisson's ratio. Since the terms $\sigma_{r\theta}$ and $\sigma_{\theta r}$ don't appear in equation (7.8), the remaining terms can be used to solve the equations for stresses in terms of strain.

$$\begin{aligned} \sigma_{rr} &= \frac{E}{(1-\upsilon^2)}\left(\varepsilon_{rr} + \upsilon\varepsilon_{\theta\theta}\right) \\ \sigma_{\theta\theta} &= \frac{E}{(1-\upsilon^2)}\left(\upsilon\varepsilon_{rr} + \varepsilon_{\theta\theta}\right) \end{aligned} \tag{7.10}$$

The definitions of strain terms are shown below.

$$\begin{aligned} \varepsilon_{rr} &= \frac{\partial u_r}{\partial r} \\ \varepsilon_{\theta\theta} &= \frac{u_r}{r} + \frac{1}{r}\frac{\partial u_\theta}{\partial \theta} \end{aligned} \tag{7.11}$$

Thus strains were expressed in the form of displacements and the displacements were solved for in equation (7.8). The displacements obtained were then used to obtain the angular and radial stresses as expressed in equation (7.10).

CHAPTER VIII

SUMMARY AND FUTURE DIRECTIONS

This dissertation presented studies that evaluated the atlas-based method of brain shift correction for better adaptation to intraoperative neurosurgical conditions. Brain shift, the non-rigid deformation of the brain tissue due to intraoperative factors like gravitational forces, hyperosmotics drugs like mannitol, resection and retraction can cause an error ranging from 1–2.5 cm in the image guidance system [5, 7]. Work done in previous literature to address this problem has included volumetric and sparse intraoperative imaging and mathematical modeling, the two often working synergistically. The obstacle with intraoperative uncertainty in finding the precise parameters to run the mathematical models have been overcome with the atlas-based inverse modeling approach, where using some prior knowledge, various perturbations of the modeling parameters are used to build an atlas of deformation and then inversely solved using sparse intraoperative measurements [2, 3]. This prior work was developed using pre- and post-operative MR data analysis, which validated the basic framework, however still left several avenues for adaptation to intraoperative conditions. Chapter IV presented a novel study where the pre- and post-operative data was compared to the pre- and intraoperative shift analysis and some critical differences were found in the nature of data, providing insights for avenues of development. This chapter also studied the importance of modeling the dural septa, subsurface structures that could potentially alter both surface and sub-surface shift correction results. Chapter V evaluated the atlas-based

model from a system implementation perspective. Minimizing user interaction, automation of the pipeline, and decrease in overall computational time would be not only be desirable, but also important to make the method feasible for fitting the time window between the acquisition of pre-operative imaging data and the beginning of surgery. To advance these aims, the chapter presented methods to automate the segmentation of the brain and the dural septa for the purposes of construction of the finite element mesh. Sensitivity analysis was also presented in this chapter that showed that similar accuracy of results could be obtained by sampling the deformation atlas more coarsely, dramatically decreasing the computational time. Prior work in the atlas-based literature accounted for factors such as gravity, mannitol and swelling, however did not account for intraoperative forces of resection and retraction. One of the problems with integrating retraction with the atlas-based approach is that exact location of retraction is not known prior to surgery. Chapter VI presented a method that combined the pre-computed atlas with a component of intraoperative active model solving to account for retraction induced deformation. This work was only tested with simulation and phantom experiments, future work would include clinical testing. Accounting for tissue resection in the atlas-based method is a challenging problem because the decompressive forces that cause tissue shrinkage are difficult to compute empirically. The compressive stresses are a function of the mass effect exerted by the tumor growth and Chapter VII presented preliminary work at an effort to understand the mechanical stress associated with tumor growth to a better extent. This work presented a tumor growth model in 1D. Future work would extend this model to 3D, include ways to test the model and devise a way to integrate the predicted stresses from the growth model into the atlas-based framework for resection modeling.

There are many other avenues for the pursuit of improvement of methodology. For instance currently, manually selected homologous points on pre- and post-resection LRS are used to drive the inverse model. The selection of homologous points is a challenging task. The LRS can only image the brain visible in the craniotomy region. Surgical resection and other deforming forces in the OR not only produce a sag in the direction normal to the surface but also cause tissue to slide out of the craniotomy region and new tissue to slide into the region. The presence of the resection hole causes the removal of vessels from the visible region of the scan. Pooling of blood and reflection of light off the surface further compounds the difficulty of establishing correspondence between the points on the pre- and post-resection LRS. For future work, it would be important to perform some sensitivity studies to establish the minimal number of corresponding points needed for the inverse model reconstruction. Also, if instead of a handful of manually selected homologous points between the pre- and post-resection LRS, the point correspondence was known for the entire craniotomy region then a greater degree of known correspondence would yield better results when used to drive the inverse model. Recent work in literature has extended techniques that now provide better correspondence between serial laser range scans and the Appendix E presents some challenges and a potential approach of how this new knowledge can be applied for solving the inverse model. This work is in no way a perfect solution and is indeed limited in scope to addressing the many challenges that confront the problems in neurosurgical image guidance. Placing this work in the context of other recent developments from our research group [97-99], the results presented in this work provides important conclusions

to advance the goal of implementation of an efficient and cost-effective brain shift correction strategy for the neurosurgical image guidance.

Appendix E

Currently, manually selected homologous points on pre and post resection LRS are used to drive the inverse model. For the clinical data presented in the previous section, the number of selected points has ranged from 15 to 24. If instead of a handful of manually selected homologous points between the pre- and post-resection LRS, the point correspondence was known for the entire craniotomy region then a greater degree of known correspondence would yield better results when used to drive the inverse model. The work of Ding et. al. has focused on establishing correspondence between the entire pre- and post-resection LRS field by using interpolation techniques [41, 100, 101]. The LRS device acquires the 3D point clouds and the 2D digital images, the correspondence between which is known due to device calibration. The work in [100] introduced the feature based technique to register pre- and post- resection point clouds by registering the 2D images. This process is shown in the following figure.

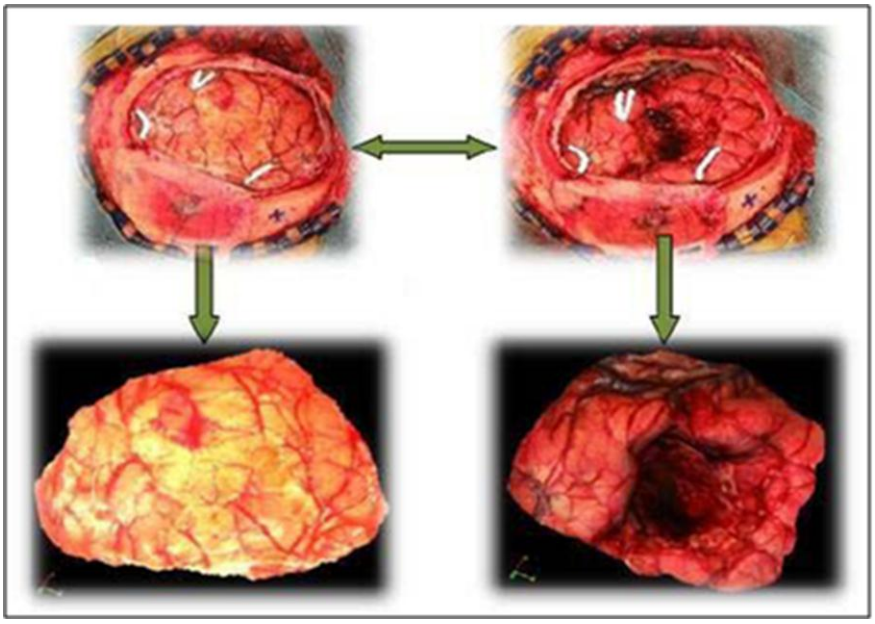

Figure 54. Registration procedure between the pre- and post- resection LRS textured point clouds outlined in [100]. The images on top are the 2D images with manually segmented vessel contours. After correspondence between the 2D images is established, it is applied to the 3D point clouds using the known correspondence between them.

The vessels used for performing the registration were manually segmented. Because the success of model updated image guided surgery is contingent on the feasibility of the method to work within the time constraints of the OR, efforts were made to automate the establishment of vessel correspondence between the images. The methodology described in [41] uses a semi-automated method for finding correspondence between vessels on the two LRS scans. In this work, instead of designating the entire length of the vessels manually, only the starting and the ending points of the vessels are manually specified and length of the vessel is automatically found using a minimal cost function on images enhanced using a vesselness filter [102]. An example of the vessel map computed between two images is shown in Figure 55 below.

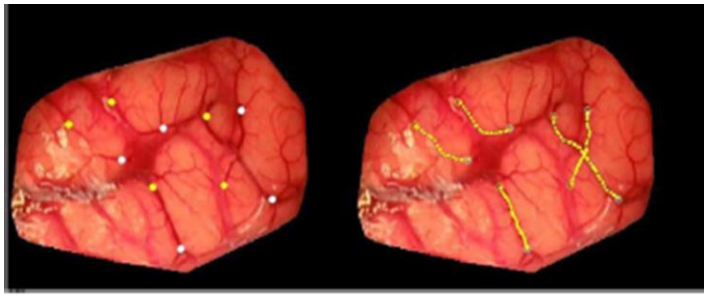

Figure 55. Semi-automatic method of establishing vessel correspondence between pre- and post- resection images as described in [41]. The image on left shows the pre-resection LRS with the starting and ending points marked in yellow and white respectively and the image of right shows the vessel maps obtained.

Registration results with sub-milimetric target registration error were reported with this semi-automated method of correspondence. Further attempts at automating this technique are described in [101, 103], where the goal is to reduce the manual designation of points only to one set of images. Hence, only the points in the pre-resection LRS are manually designated and the corresponding points in the post-resection LRS are found by using an automated method of projection. The tumor resection drastically alters the topography of the surfaces, which presents a considerable challenge for this method of establishing point correspondence. If serial images could be acquired through the resection process, the gradation of deformation between the intermediate images would ease the problems of the registration process. However continuous acquisition of laser range scans would pose a serious intrusion into the surgical procedure. Hence the work in [101, 103] uses serial images acquired from the video stream of the surgical microscope and proposes registering the beginning and the end of the sequence to the pre- and post- resection LRS images respectively.

A vessel based registration followed by a spline interpolation yields much higher correspondence than manually selected homologous points that are currently used to

drive the data. The inverse model is solved with a least squares minimization approach as was discussed in section C.2.1. The least mean square minimization problem is shown below.

$$\min \left\| \left(M\boldsymbol{\alpha} - \boldsymbol{u}_{sparse} \right) \right\|^2 \qquad (8.1)$$

In equation (8.1) above, M is an $3N_s \times m$ atlas of solutions, where m is the number of atlas solutions and N_s is the number of sparse points where displacement is known, $3N_s$ represents the displacements in the three coordinates, $\boldsymbol{\alpha}$ is the vector of weighting coefficients and $\underline{\boldsymbol{u}}_{sparse}$ is the vector of sparse measurements. The components expanded out can be written as follows

$$\min \left\| \begin{bmatrix} dx_{11} & dx_{12} & \dots & dx_{1m} \\ dy_{11} & dy_{12} & \dots & dy_{1m} \\ dz_{11} & dz_{12} & \dots & dz_{1m} \\ \dots & \dots & \dots & \dots \\ dz_{N_s 1} & dz_{N_s 2} & \dots & dz_{N_s m} \end{bmatrix} \begin{bmatrix} \alpha_1 \\ \alpha_2 \\ \dots \\ \alpha_m \end{bmatrix} - \begin{bmatrix} u_{x1} \\ u_{y1} \\ u_{z1} \\ \dots \\ u_{zN_s} \end{bmatrix} \right\|^2 \qquad (8.2)$$

In the above equation, dx_{ij}, dy_{ij}, and dz_{ij} are the displacements in x, y, and z direction at the 'i^{th}' sparse node of the mesh in the 'j^{th}' solution in the atlas, α_j is the weighting coefficient for the 'j^{th}' solution in the atlas and u_{xi}, u_{yi}, and u_{zi} are the measured displacements in the x, y, and z directions at the 'i^{th}' sparse node in the mesh. We hypothesize that the expansion of the M matrix and the $\underline{\boldsymbol{u}}_{sparse}$ vector would condition the inverse problem better. To test this hypothesis, the denser displacement field obtained by interpolation techniques would be integrated into equation (8.2). First a point-to-point mapping must be established between the LRS surface and the brain mesh. The LRS surfaces have much higher point density than the corresponding craniotomy region on the surface of the brain mesh. The LRS surface points can be down sampled and a closest

point matching can establish correspondence between LRS surface points and mesh surface nodes since they are both in image space through a surface mutual information registration.

The success of an interpolation technique depends on a relatively even distribution of the known quantities to be interpolated across the domain. If the homologous points are localized in one region of the image, the interpolation results on the regions with extremely sparse data could potentially have greater errors. This problem is represented conceptually in the figure below.

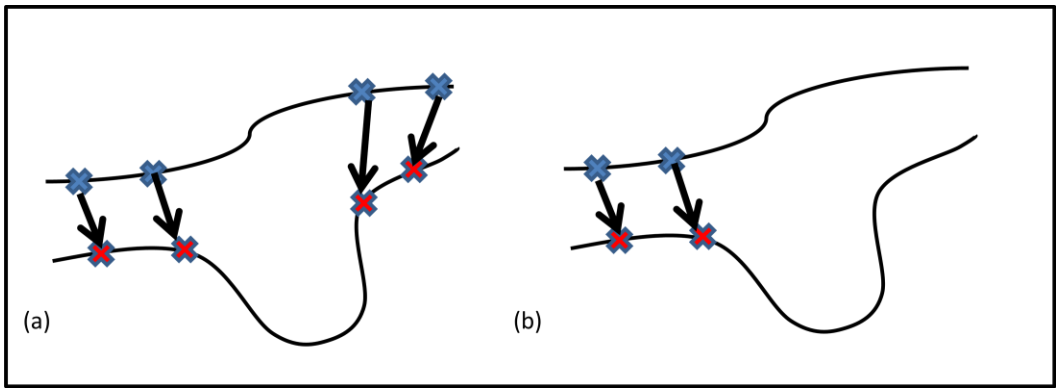

Figure 56. Conceptual representation of the problem of interpolation. The line on top represents the pre-resection LRS and the line on the bottom represents the post-resection LRS. (a) Shows a relatively ideal distribution of corresponding points, (b) shows a potential distribution where no corresponding points are found in the right hand side part of the surfaces. The interpolation errors would be much higher in the right hand side of the image because of the lack of data in that region.

Figure 56 (a) shows an ideal distribution of homologous points around the resection cavity. During the acquisition of the serial microscope video images, instruments occasionally block the view of the vessels. Though the method has shown considerable robustness to small periodic obstructions, a bigger problem is posed by the discontinuous use of the microscope through the procedure, resulting in more drastic changes in the discontinuous frames, which would confound the automated point finding method. Figure

56 (b) shows a potential biased point correspondence found due to the above described problems, where the homologous points are localized on one side of the surfaces. The resultant error of fitting a spline would be much higher on the right hand side because of the lack of point correspondence in that region. Since the interpolated displacements would outnumber the points with known correspondence, the points would have to be weighted appropriately to avoid biasing the results. This could be done by rewriting the least squares minimization problem as follows.

$$\min \left(M\boldsymbol{\alpha} - \boldsymbol{u}_{sparse} \right)^T W \left(M\boldsymbol{\alpha} - \boldsymbol{u}_{sparse} \right) \qquad (8.3)$$

In the above equation W is a weighting matrix, where the homologous measurement points could have a higher weight and the interpolated displacements could be assigned a lower weight. The weighting coefficients, $\boldsymbol{\alpha}$, could be solved by directly computing or obtaining a solution through constrained optimization of the following equation.

$$\boldsymbol{\alpha} = \left(M^T W M \right)^{-1} M^T W \boldsymbol{u}_{sparse} \qquad (8.4)$$

A potential choice for the weighting matrix is the inverse of the covariance of the vector being estimated [104], which in this case would be the residual error.

$$W = [Cov(r)]^{-1} \qquad (8.5),$$

$$\text{where} \quad r = M\boldsymbol{\alpha} - \boldsymbol{u}_{sparse} \qquad (8.6)$$

Thus in order to establish a weighting matrix, a prior estimate of the covariance of the residuals must be made. The error due to interpolation will be larger if the point lies farther from the corresponding features. An empirical relation between target registration error and distance from known feature can be established by data fitting. The error established from that relationship can then be used for estimating the covariance matrix

in equation (8.5). In the work of Ding et. al. [41], registration results were obtained through semi-automatic vessel segmentation algorithm. Since the vessels were selected semi-automatically, there is a good distribution of vessels through the surface. In order to simulate a scenario where fewer vessel features are available, a smaller subset of the corresponding vessel contours can be used for the registration and interpolation. The remaining corresponding vessels can be used as novel targets. The empirical registration between target registration error and distance from known features can then be established by data fitting, which can then be use used to construct an appropriate weighting matrix. The shift correction error resulting from this approach would be compared to an algorithm with simple least square minimization of all distances as well as to the simple homologous point approach.

REFERENCES

[1] J. A. Schwartzbaum, J. L. Fisher, K. D. Aldape, and M. Wrensch, "Epidemiology and molecular pathology of glioma," *Nat Clin Pract Neurol,* vol. 2, no. 9, pp. 494-503, Sep, 2006.

[2] P. Dumpuri, R. C. Thompson, B. M. Dawant, A. Cao, and M. I. Miga, "An atlas-based method to compensate for brain shift: Preliminary results," *Medical Image Analysis,* vol. 11, no. 2, pp. 128-145, 2006.

[3] P. Dumpuri, R. C. Thompson, A. Cao, S. Ding, I. Garg, B. M. Dawant, and M. I. Miga, "A fast efficient method to compensate for brain shift for tumor resection therapies measured between preoperative and postoperative tomograms.," *IEEE Transactions on Biomedical Engineering,* vol. 57, no. 6, pp. 1285-1296, 2010.

[4] P. J. Kelly, B. A. Kall, S. Goerss, and F. Earnest, "Computer-assisted stereotaxic laser resection of intra-axial brain neoplasms," *Journal of Neurosurgery,* vol. 64, no. 3, pp. 427-439, 1986.

[5] C. Nimsky, O. Ganslandt, S. Cerny, P. Hastreiter, G. Greiner, and R. Fahlbusch, "Quantification of, visualization of, and compensation for brain shift using intraoperative magnetic resonance imaging," *Neurosurgery,* vol. 47, no. 5, pp. 1070-1079, Nov, 2000.

[6] D. L. G. Hill, C. R. Maurer, R. J. Maciunas, J. A. Barwise, J. M. Fitzpatrick, and M. Y. Wang, "Measurement of intraoperative brain surface deformation under a craniotomy," *Neurosurgery,* vol. 43, no. 3, pp. 514-526, Sep, 1998.

[7] D. W. Roberts, A. Hartov, F. E. Kennedy, M. I. Miga, and K. D. Paulsen, "Intraoperative brain shift and deformation: A quantitative analysis of cortical displacement in 28 cases," *Neurosurgery,* vol. 43, no. 4, pp. 749-758, Oct, 1998.

[8] P. Hastreiter, C. Rezk-Salama, G. Soza, M. Bauer, G. Greiner, R. Fahlbusch, O. Ganslandt, and C. Nimsky, "Strategies for brain shift evaluation," *Medical Image Analysis,* vol. 8, pp. 447-464, 2004.

[9] P. J. Kelly, "Intraoperative brain shift and deformation: A quantitative analysis of cortical displacement in 28 cases - Comment," *Neurosurgery,* vol. 43, no. 4, pp. 759-759, Oct, 1998.

[10] L. D. Lunsford, R. Parrish, and L. Albright, "Intraoperative imaging with a therapeutic computed tomographic scanner," *Neurosurgery,* vol. 15, no. 4, pp. 559-61, Oct, 1984.

[11] H. Okudera, S. Kobayashi, K. Kyoshima, H. Gibo, T. Takemae, and K. Sugita, "Development of the operating computerized tomographic scanner system for neurosurgery," *Acta Neurochir (Wien),* vol. 111, no. 1-2, pp. 61-3, 1991.

[12] W. E. Butler, C. M. Piaggio, C. Constantinou, L. Nikalson, R. G. Gonzales, G. R. Cosgrove, and N. T. Zervas, "A mobile computed tomographic scanner with intraoperative and intensive care unit applications.," *Neurosurgery,* vol. 88, no. 4, pp. 1304-1310, 1998.

[13] P. M. Black, T. M. Moriarty, E. I. Alexander, P. Stieg, E. J. Woodard, P. L. Gleason, C. H. Martin, R. Kikinis, R. B. Schwartz, and F. A. Jolesz, "Development and Implementation of Intraoperative Magnetic Resonance Imaging and Its Neurosurgical Applications," *Neurosurgery,* vol. 41, no. 4, pp. 831-845, 1997.

[14] C. R. Wirtz, M. Knauth, A. Staubert, M. M. Bonsanto, K. Sartor, S. Kunze, and V. M. Tronnier, "Clinical evaluation and follow-up results for intraoperative magnetic resonance imaging in neurosurgery," *Neurosurgery,* vol. 46, no. 5, pp. 1112-1120, 2000.

[15] V. Tronnier, A. Staubert, R. Wirtz, M. Knauth, M. Bonsanto, and S. Kunze, "MRI-guided brain biopsies using a 0.2 Tesla open magnet," *Minimally Invasive Neurosurgery,* vol. 42, no. 3, pp. 118-22., 1999.

[16] V. M. Tronnier, A. Staubert, S. Hahnel, and A. Sarem-Aslani, "Magnetic resonance imaging with implanted neurostimulators: an in vitro and in vivo study," *Neurosurgery,* vol. 44, no. 1, pp. 118-25; discussion 125-6., 1999.

[17] V. M. Tronnier, C. R. Wirtz, M. Knauth, G. Lenz, O. Pastyr, M. M. Bonsanto, F. K. Albert, R. Kuth, A. Staubert, W. Schlegel, K. Sartor, and S. Kunze, "Intraoperative diagnostic and interventional magnetic resonance imaging in neurosurgery," *Neurosurgery,* vol. 40, no. 5, pp. 891-900; discussion 900-2, May, 1997.

[18] G. R. Sutherland, T. Kaibara, D. Louw, D. I. Hoult, B. Tomanek, and J. Saunders, "A mobile high-field magnetic resonance system for neurosurgery," *J Neurosurg,* vol. 91, no. 5, pp. 804-13., 1999.

[19] G. R. Sutherland, T. Kaibara, C. Wallace, B. Tomanek, and M. Richter, "Intraoperative assessment of aneurysm clipping using magnetic resonance angiography and diffusion-weighted imaging: Technical case report," *Neurosurgery,* vol. 50, no. 4, pp. 893-897, 2002.

[20] F. A. Jolesz, A. Nabavi, and R. Kikinis, "Integration of interventional MRI with computer-assisted surgery," *J Magn Reson Imaging,* vol. 13, no. 1, pp. 69-77, Jan, 2001.

[21] T. Kaibara, S. T. Myles, M. A. Lee, and G. R. Sutherland, "Optimizing epilepsy surgery with intraoperative MR imaging," *Epilepsia,* vol. 43, no. 4, pp. 425-9, Apr, 2002.

[22] M. Hadani, R. Spiegelman, Z. Feldman, H. Berkenstadt, and Z. Ram, "Novel, compact, intraoperative magnetic resonance imaging-guided system for conventional neurosurgical operating rooms," *Neurosurgery,* vol. 48, no. 4, pp. 799-807; discussion 807-9, Apr, 2001.

[23] J. W. Trobaugh, D. J. Trobaugh, and W. D. Richard, "Three-dimensional imaging with stereotactic ultrasonography," *Comput Med Imaging Graph,* vol. 18, no. 5, pp. 315-23, Sep-Oct, 1994.

[24] R. M. Comeau, A. Fenster, and T. M. Peters, "Intraoperative US in interactive image-guided neurosurgery," *Radiographics,* vol. 18, no. 4, pp. 1019-27, Jul-Aug, 1998.

[25] D. B. Downey, A. Fenster, and J. C. Williams, "Clinical utility of three-dimensional US," *Radiographics,* vol. 20, no. 2, pp. 559-71, Mar-Apr, 2000.

[26] D. Gobbi, R. Comeau, and T. Peters, "Ultrasound Probe Tracking for Real-Time Ultrasound/MRI Overlay and Visualization of Brain Shift," *Medical Image Computing and Computer Assisted Intervention: Lecture Notes in Computer Science,* vol. 1679, pp. 920-927, 1999.

[27] D. Gobbi, R. Comeau, and T. Peters, "Ultrasound/MRI Overlay with Image Warping for Neurosurgery," *Medical Image Computing and Computer Assisted Intervention: Lecture Notes in Computer Science,* vol. 1935, pp. 29-53, 2000.

[28] M. M. J. Letteboer, P. W. A. Willems, M. A. Viergever, and W. J. Niessen, "Brain shift estimation in image-guided neurosurgery using 3-D ultrasound," *IEEE Transactions on Biomedical Engineering,* vol. 52, no. 2, pp. 268-276, Feb, 2005.

[29] N. Archip, O. Clatz, S. Whalen, D. Kacher, A. Fedorov, A. Kot, N. Chrisocholdes, F. Jolesz, A. Golby, P. M. Black, and S. K. Warfield, "Non-rigid alignment of pre-operative MRI, fMRI, and DT-MRI with intra-operative MRI for enhanced visualization and navigation in image-guided neurosurgery," *Neuroimage,* vol. 35, no. 2, pp. 609-624, Apr, 2007.

[30] N. Hata, T. Dohi, S. K. Warfield, W. M. Wells III, R. Kikinis, and F. A. Jolesz, "Multimodality Deformable Registration of Pre- and Intraoperative Images for MRI-guided Brain Surgery," *Proceedings of the First International Conference on Medical Image Computing and Computer-Assisted Intervention,* vol. 1496, no. 1998, pp. 1067-1074, 1998.

[31] A. Hagemann, K. Rohr, H. S. Stiehl, U. Spetzger, and J. M. Gilsbach, "Biomechanical modeling of the human head for physically based, nonrigid image registration," *IEEE Transactions on Medical Imaging,* vol. 18, no. 10, pp. 875-884, Oct, 1999.

[32] M. Ferrant, A. Nabavi, B. t. Macq, F. A. Jolesz, R. Kikinis, and S. K. Warfield, "Registration of 3-D Intraoperative MR Images of the Brain Using a Finite-Element Biomechanical Model," *IEEE Transactions on Medical Imaging,* vol. 20, no. 12, pp. 1384, 2001.

[33] A. Wittek, K. Miller, R. Kikinis, and S. K. Warfield, "Patient-specific model of brain deformation: Application to medical image registration," *Journal Of Biomechanics,* vol. 40, no. 4, pp. 919-929, 2007.

[34] O. Clatz, H. Delingette, I.-F. Talos, A. J. Golby, R. Kikinis, F. Jolesz, N. Ayache, and S. Warfield, "Robust non-rigid registration to capture brain shift from intraoperative MRI," *IEEE Transactions on Medical Imaging,* vol. 24, no. 11, pp. 1417-1427, 2006.

[35] O. Skrinjar, A. Nabavi, and J. Duncan, "Model-driven brain shift compensation," *Medical Image Analysis,* vol. 6, no. 4, pp. 361-373, December, 2002.

[36] H. Sun, D. W. Roberts, H. and Farid, Z. Wu, A. Hartov, and K. D. Paulsen, "Cortical Surface Tracking Using a Stereoscopic Operating Microscope," *Neurosurgery,* vol. 56, no. 1, pp. 86-97, 2005.

[37] M. A. Audette, K. Siddiqi, F. P. Ferrie, and T. M. Peters, "An integrated range-sensing, segmentation and registration framework for the characterization of intra-surgical brain deformations in image-guided surgery," *Computer Vision and Image Understanding,* vol. 89, no. 2-3, pp. 226-251, Feb-Mar, 2003.

[38] T. K. Sinha, M. I. Miga, D. M. Cash, and R. J. Weil, "Intraoperative cortical surface characterization using laser range scanning: Preliminary results," *Neurosurgery,* vol. 59, no. 4, pp. 368-376, 2006.

[39] A. Cao, R. C. Thompson, P. Dumpuri, B. M. Dawant, R. L. Galloway, S. Ding, and M. I. Miga, "Laser range scanning for image-guided neurosurgery:

Investigation of image-to-physical space registrations," *Medical Physics,* vol. 35, no. 4, pp. 1593-1605, 2008.

[40] T. K. Sinha, B. M. Dawant, V. Duay, D. M. Cash, R. J. Weil, and M. I. Miga, "A method to track cortical surface deformations using a laser range scanner," *IEEE Transactions on Medical Imaging,* vol. 24, no. 6, pp. 767-781, 2005.

[41] S. Ding, M. I. Miga, J. H. Noble, A. Cao, P. Dumpuri, R. C. Thompson, and B. M. Dawant, "Semiautomatic Registration of Pre- and Postbrain Tumor Resection Laser Range Data: Method and Validation," *Biomedical Engineering, IEEE Transactions on,* vol. 56, no. 3, pp. 770-780, 2009.

[42] S. K. Warfield, F. Talos, A. Tei, A. Bharatha, A. Nabavi, M. Ferrant, P. M. Black, F. A. Jolesz, and R. Kikinis, "Real-time registration of volumetric brain MRI by biomechanical simulation of deformation during image guided neurosurgery," *Computing and Visualization in Science,* vol. 5, no. 1, pp. 3-11, 2002.

[43] M. Bucki, C. Lobos, and Y. Payan, "Framework for a low-cost intra-operative image-guided neuronavigator including brain shift compensation," *Engineering in Medicine and Biology Society, 29th Annual International Conference of the IEEE,* vol. EBMS 2007, pp. 872-875, 2007.

[44] J. Hu, X. Jin, J. B. Lee, L. Zhang, V. Chaudhary, M. Guthikonda, K. H. Yang, and A. I. King, "Intraoperative brain shift prediction using a 3D inhomogenous patient-specific finite element model.," *J Neurosurg,* vol. 106, pp. 164-169, 2007.

[45] G. R. Joldes, A. Wittek, and K. Miller, "Suite of finite element algorithms for accurate computation of soft tissue deformation for surgical simulation," *Med Image Anal,* vol. 13, no. 6, pp. 912-9, Dec, 2009.

[46] K. Miller, "Constitutive model of brain tissue suitable for finite element analysis of surgical procedures," *Journal Of Biomechanics,* vol. 32, no. 5, pp. 531-537, 1999.

[47] A. Wittek, R. Kikinis, S. K. Warfield, and K. Miller, "Brain shift computation using a fully nonlinear biomechanical model," *Med Image Comput Comput Assist Interv Int Conf Med Image Comput Comput Assist Interv,* vol. 8, no. 2, pp. 583-90, 2005.

[48] J. Ma, A. Wittek, G. R. Joldes, T. Washio, K. Chinzei, and K. Miller, "Evaluation of accuracy of non-linear finite element computations for surgical simulation: study using brain phantom," *Computer Methods in Biomechanics and Biomedical Engineering,* vol. 13, no. 6, pp. 783-794, 2010.

[49] S. K. Kyriacou, A. Mohamed, K. Miller, and S. Neff, "Brain mechanics for neurosurgery: modeling issues," *Biomech Model Mechanobiol,* vol. 1, pp. 151-164, 2002.

[50] K. K. Mendis, R. L. Stalnaker, and S. H. Advani, "A constitutive relationship for large deformation finite element modeling of brain tissue," *Journal of Biomechanical Engineering,* vol. 117, pp. 279-285, 1995.

[51] K. D. Paulsen, M. I. Miga, F. E. Kennedy, P. J. Hoopes, A. Hartov, and D. W. Roberts, "A computational model for tracking subsurface tissue deformation during stereotactic neurosurgery.," *IEEE Transactions on Biomedical Engineering,* vol. 49, no. 8, pp. 823-835, 1999.

[52] K. E. Lunn, K. D. Paulsen, D. W. Roberts, F. E. Kennedy, A. Hartov, and L. A. Platenick, "Non-rigid brain registration: synthesizing full volume deformation

fields from model basis solutions constrained by partial volume intraoperative data," *Computer Vision and Image Understanding,* vol. 89, pp. 299-317, 2003.

[53] M. A. Biot, "General Theory of Three-Dimensional Consolidation," *Journal of Applied Physics,* vol. 12, no. 2, pp. 155-164, 1941.

[54] M. I. Miga, K. D. Paulsen, J. M. Lemery, S. D. Eisner, A. Hartov, F. E. Kennedy, and D. W. Roberts, "Model-updated image guidance: Initial clinical experiences with gravity-induced brain deformation," *IEEE Transactions on Medical Imaging,* vol. 18, no. 10, pp. 866-874, 1999.

[55] A. Goshtasby, "Registration of images with geometric distortions," *IEEE Transactions on Geoscience and Remote Sensing,* vol. 26, no. 1, pp. 60-64, 1988.

[56] P.-F. D'Haese, V. Duay, T. E. Merchant, B. Macq, and B. M. Dawant, "Atlas-Based Segmentation of the Brain for 3-Dimensional Treatment Planning in Children with Infratentorial Ependymoma," *Proc. MICCAI,* pp. 627-634, 2003.

[57] W. E. Lorensen, and H. E. Cline, "Marching cubes: A high resolution 3D surface construction algorithm," *SIGGRAPH Comput. Graph.,* vol. 21, no. 4, pp. 163-169, 1987.

[58] W. J. Schroeder, K. M. Martin, and W. E. Lorensen, *Visualization toolkit: an object-oriented approach to 3D Graphics,* 3rd ed., pp. 331-334, Albany, NY: Kitware, Inc., 2003.

[59] J. M. Sullivan, G. Charron, and K. D. Paulsen, "A three-dimensional mesh generator for arbitrary multiple material domains," *Finite Elements in Analysis and Design,* vol. 25, no. 3-4, pp. 219-241, 1997.

[60] J. D. Humphrey, and S. L. Delange, *An Introduction to Biomechanics,* pp. 563, New York, NY: Springer, 2004.

[61] P. J. Besl, and N. D. McKay, "A method of registration of 3-D shapes," *IEEE Trans Pattern Anal. Mach. Intell.,* vol. 14, pp. 239-256, 1992.

[62] L. W. Clements, P. Dumpuri, W. C. Chapman, R. L. Galloway Jr., and M. I. Miga, "Atlas-based method for model updating in image-guided liver surgery.," *Medical Imaging 2007: Visualization and Image-Guided Procedures: Proc of SPIE,* 2007.

[63] N. Joachimowicz, C. Pichot, and J. P. Hugonin, "Inverse scattering: an iterative numerical method for electromagnetic imaging," *Antennas and Propagation, IEEE Transactions on,* vol. 39, no. 12, pp. 1742-1753, 1991.

[64] P. Dumpuri, R. C. Chen, and M. I. Miga, "Model updated image guidance: A statistical approach," *Lecture Notes in Computer Science: Medical Image Computing and Computer-Assisted Intervention – MICCAI 2003,* vol. 2879, no. 1, pp. 375-382, 2003.

[65] P. E. Gill, W. Murray, and M. H. Wright, *Practical Optimization,* London, UK: Academic Press, 1981.

[66] P. Paul, X. Morandi, and P. Jannin, "A surface registration method for quantification of intraoperative brain deformations in image-guided neurosurgery," *IEEE Trans Inf Technol Biomed,* vol. 13, no. 6, pp. 976-83, Nov, 2009.

[67] C. R. Maurer, D. L. G. Hill, A. J. Martin, H. Liu, M. McCue, D. Rueckert, D. Lloret, W. A. Hall, R. E. Maxwell, D. J. Hawkes, and C. L. Truwit, "Investigation of intraoperative brain deformation using a 1.5T interventional MR system:

preliminary results.," *IEEE Transactions on Medical Imaging*, vol. 17, no. 5, pp. 817-825, 1998.

[68] M. I. Miga, K. D. Paulsen, F. E. Kennedy, A. Hartov, and D. W. Roberts, "Model-updated image-guided neurosurgery using the finite elemtn method: incorporation of the falx cerebri.," *Medical Image Computing and Computer Assisted Intervention: Lecture Notes in Computer Science*, vol. 1679, pp. 900-909, 1999.

[69] I. Garg, S. Ding, A. M. Coffey, P. Dumpuri, R. C. Thompson, B. M. Dawant, and M. I. Miga, "Enhancement of subsurface brain shift model accuracy: a preliminary study," *SPIE Medical Imaging 2010: Visualization, Image-Guided Procedures, and Modeling*, vol. 7625, pp. 76250J-76250J, 2010.

[70] M. I. Miga, K. D. Paulsen, F. E. Kennedy, P. J. Hoopes, A. Hartov, and D. W. Roberts, "In Vivo Analysis of Heterogeneous Brain Deformation Computations for Model-Updated Image Guidance," *Comput Methods Biomech Biomed Engin*, vol. 3, no. 2, pp. 129-146, 2000.

[71] K. D. Paulsen, M. I. Miga, F. E. Kennedy, P. J. Hoopens, A. Hartov, and D. W. Roberts, "A computational model for tracking subsurface tissue deformation during stereotactic neurosurgery," *Biomedical Engineering, IEEE Transactions on*, vol. 46, no. 2, pp. 213-225, 1999.

[72] D. J. Sheskin, *Handbook of parametric and nonparametric statistical procedures*, Second edition ed., pp. 142-143, Boca Raton, FL: Chapman & Hall/CRC, 2000.

[73] I. Chen, A. M. Coffey, S. Ding, P. Dumpuri, B. M. Dawant, R. C. Thompson, and M. I. Miga, "Intraoperative brain shift compensation: accounting for dural septa," *IEEE Trans Biomed Eng*, vol. 58, no. 3, pp. 499-508, Mar, 2011.

[74] F. Maes, A. Collignon, D. Vandermeulen, G. Marchal, and P. Suetens, "Multimodality image registration by maximization of mutual information," *Medical Imaging, IEEE Transactions on*, vol. 16, no. 2, pp. 187-198, 1997.

[75] G. K. Rohde, A. Aldroubi, and B. M. Dawant, "The adaptive bases algorithm for intensity-based nonrigid image registration," *Medical Imaging, IEEE Transactions on*, vol. 22, no. 11, pp. 1470-1479, 2003.

[76] S. Balay, W. D. Gropp, L. C. McInnes, and B. F. Smith, *Modern Software Tools in Scientific Computing*, pp. 163-202, Ann Arbor, MI: Birkhauser Press, 1997.

[77] H. El-Rewini, and M. Abd-El-Barr, *Message Passing Interface (MPI), in Advanced Computer Architecture and Parallel Processing*, Hoboken, NJ: John Wiley & Sons, Inc., 2005.

[78] A. J. Russell, and J. R. Bringas, "A review of brain retraction and recommendations for minimizing intraoperative brain injury.," *Neurosurgery*, vol. 33, no. 6, pp. 1052-1064, December 1993, 1993.

[79] W. Xu, P. Mellergard, U. Ungerstedt, and C. H. Nordstrom, "Local changes in cerebral energy metabolism due to brain retraction during routine neurosurgical procedures," *Acta Neurochir (Wien)*, vol. 144, no. 7, pp. 679-83, Jul, 2002.

[80] L. A. Platenik, M. I. Miga, D. W. Roberts, K. E. Lunn, F. E. Kennedy, A. Hartov, and K. D. Paulsen, "In vivo quantification of retraction deformation modeling for updated image-guidance during neurosurgery," *IEEE Transactions on Biomedical Engineering*, vol. 49, no. 8, pp. 823-835, 2002.

[81] M. I. Miga, D. W. Roberts, F. E. Kennedy, L. A. Platenik, A. Hartov, K. E. Lunn, and K. D. Paulsen, "Modeling of retraction and resection for intraoperative updating of images," *Neurosurgery,* vol. 49, no. 1, pp. 75-84; discussion 84-5, Jul, 2001.

[82] H. Sun, F. E. Kennedy, E. J. Karlson, A. Hartov, D. W. Roberts, and K. D. Paulsen, "Modeling of Brain Tissue Retraction Using Intraoperative Data " *Medical Image Computing and Computer-Assisted Intervention – MICCAI 2004,* vol. 3217, pp. 225-233, 2004.

[83] A. Wittek, T. Hawkins, and K. Miller, "On the unimportance of constitutive models in computing brain deformation for image-guided surgery," *Biomech Model Mechanobiol,* vol. 8, no. 1, pp. 77-84, Feb, 2009.

[84] M. Miga, A. Staubert, K. Paulsen, F. Kennedy, V. Tronnier, D. Roberts, A. Hartov, L. Platenik, and K. Lunn, "Model-Updated Image-Guided Neurosurgery: Preliminary Analysis Using Intraoperative MR

Medical Image Computing and Computer-Assisted Intervention – MICCAI 2000," Lecture Notes in Computer Science S. Delp, A. DiGoia and B. Jaramaz, eds., pp. 11-14: Springer Berlin / Heidelberg, 2000.

[85] R. Greenwood, M. P. Barnes, T. T. McMillan, and C. D. Ward, *Neurological Rehabilitation*, pp. 535-537: Psychology Press, 1997.

[86] CBTRUS. "Statistical Report: Primary Brain Tumors in the United States, 1998-2002," http://www.cbtrus.org.

[87] K. R. Swanson, E. C. Alvord, Jr., and J. D. Murray, "Virtual brain tumours (gliomas) enhance the reality of medical imaging and highlight inadequacies of current therapy," *British Journal of Cancer,* vol. 86, no. 1, pp. 14-18, 2002.

[88] K. R. Swanson, C. Bridge, J. D. Murray, and E. C. Alvord, Jr., "Virtual and real brain tumors: using mathematical modeling to quantify glioma growth and invasion," *Journal of Neurological Science,* vol. 216, no. 1, pp. 1-10, 2003.

[89] S. Jbabdi, E. Mandonnet, H. Duffau, L. Capelle, K. R. Swanson, M. Pelegrini-Issac, R. Guillevin, and H. Benali, "Simulation of anisotropic growth of low-grade gliomas using diffusion tensor imaging," *Magn Reson Med,* vol. 54, no. 3, pp. 616-24, Sep, 2005.

[90] O. Clatz, M. Sermesant, P. Y. Bondiau, H. Delingette, S. K. Warfield, G. Malandain, and N. Ayache, "Realistic simulation of the 3-D growth of brain tumors in MR images coupling diffusion with biomechanical deformation," *IEEE Trans Med Imaging,* vol. 24, no. 10, pp. 1334-46, Oct, 2005.

[91] A. M. Stein, T. Demuth, D. Mobley, M. Berens, and L. M. Sander, "A mathematical model of glioblastoma tumor spheroid invasion in a three-dimensional in vitro experiment," *Biophysical Journal,* vol. 92, no. 10, pp. 356-365, 2006.

[92] G. Helmlinger, P. A. Netti, H. C. Lichtenbeld, R. J. Melder, and R. K. Jain, "Solid stress inhibits the growth of multicellular tumor spheroids," *Nature Biotechnology,* vol. 15, no. 8, pp. 778-783, Aug, 1997.

[93] D. Ambrosi, and F. Mollica, "The role of stress in the growth of a multicell spheroid," *Journal of Mathematical Biology,* vol. 48, no. 5, pp. 477-499, 2004.

[94] T. Roose, P. A. Netti, L. L. Munn, Y. Boucher, and R. K. Jain, "Solid stress generated by spheroid growth estimated using a linear poroelasticity model," *Microvascular Research,* vol. 66, pp. 204-212, 2003.

[95] G. Cruywagen, D. Woodward, P. Tracqui, G. Bartoo, J. D. Murray, and E. C. Alvord, Jr., "The modeling of diffusive tumours," *Journal of Biological Systems,* vol. 3, no. 4, pp. 937-945, 1995.

[96] A. P. Boresi, and K. P. Chong, *Elasticity in Engineering Mechanics,* 2nd ed., New York: John Wiley & Sons, 2000.

[97] T. S. Pheiffer, B. Lennon, A. L. Simpson, and M. I. Miga, "Development of a novel laser range scanner," *SPIE 2011 Medical Imaging: Visualization, Image-Guided Procedures, and Modeling Conference,* vol. 7964, 2011.

[98] A. L. Simpson, J. Burgner, I. Chen, T. S. Pheiffer, K. Sun, R. C. Thompson, R. J. Webster, and M. I. Miga, "Intraoperative brain resection cavity characterization with conoscopic holography," *SPIE 2012 Medical Imaging: Image-Guided Procedures, Robotic Interventions, and Modeling Conference,* vol. (in press), 2012.

[99] A. L. Simpson, B. Ma, R. E. Ellis, A. J. Stewart, and M. I. Miga, "Uncertainty propagation and analysis of image-guided surgery," *SPIE 2011 Medical Imaging: Visualization, Image-Guided Procedures, and Modeling Conference,* vol. 7964, 2011.

[100] S. Ding, M. I. Miga, R. C. Thompson, P. Dumpuri, A. Cao, and B. M. Dawant, "Estimation of intra-operative brain shift using a tracked laser range scanner," *Proceedings of the 29th Annual International Conference of the IEEE Engineering in Medicine and Biology Society*, pp. 848-851, 2007.

[101] S. Ding, M. I. Miga, R. C. Thompson, and B. M. Dawant, "Robust vessel registration and tracking of microscope video images in tumor resection neurosurgery," *Proceedings of the Sixth IEEE international conference on Symposium on Biomedical Imaging: From Nano to Macro*, 2009.

[102] A. F. Frangi, W. J. Niessen, K. L. Vincken, and M. A. Viergever, "Multiscale vessel enhancement filtering," *Medical Image Computing and Computer-Assisted Intervention - Miccai'98,* vol. 1496, pp. 130-137, 1998.

[103] S. Ding, M. I. Miga, T. S. Pheiffer, A. L. Simpson, R. C. Thompson, and B. M. Dawant, "Tracking of vessels in intra-operative microscope video sequences for cortical displacement estimation," *IEEE Trans Biomed Eng,* vol. 58, no. 7, pp. 1985-1993, 2011.

[104] D. R. Lynch, *Numerical partial differential equations for environmetal scientists and engineers: a first practical course*, pp. 281-282, New York, NY: Springer Science+Business Media, Inc., 2005.